Adaptive Fringe Pattern Projection Techniques for Image Saturation Avoidance in 3D Surface Measurement

by

Christopher Waddington

A thesis
presented to the University of Waterloo
in fulfillment of the
thesis requirement for the degree of
Master of Applied Science
in
Systems Design Engineering

Waterloo, Ontario, Canada, 2010

I hereby declare that I am the sole author of this thesis. This is a true copy of the thesis, including any required final revisions, as accepted by my examiners.

I understand that my thesis may be made electronically available to the public.

Abstract

Fringe-pattern projection (FPP) techniques are commonly used for surface-shape measurement in a wide range of applications including object and scene modeling, part inspection, and reverse engineering. Periodic intensity fringe patterns with a specific amplitude are projected by the projector onto an object and a camera captures images of the fringe patterns, which appear distorted by the object surface from the perspective of the camera. The images are then used to compute the height or depth of the object at each pixel.

One of the problems with FPP is that camera sensor saturation may occur if there is a large change in ambient lighting or a large range in surface reflectivity when measuring object surfaces. Camera sensor saturation occurs when the reflected intensity exceeds the maximum quantization level of the camera. A low SNR occurs when there is a low intensity modulation of the fringe pattern compared to the amount of noise in the image. Camera sensor saturation and low SNR can result in significant measurement error. Careful selection of the camera aperture or exposure time can reduce the error due to camera sensor saturation or low SNR. However, this is difficult to perform automatically, which may be necessary when measuring objects in uncontrolled environments where the lighting may change and objects have different surface reflectivity.

This research presents three methods to avoid camera sensor saturation when measuring surfaces subject to changes in ambient lighting and objects with a large range in reflectivity. All these methods use the same novel approach of lowering the maximum input gray level (MIGL) to the projector for saturation avoidance. This approach avoids saturation by lowering the reflected intensity so that formerly saturated intensities can be captured by the camera.

The first method of saturation avoidance seeks a trade-off between robustness to intensity saturation and low SNR. Measurements of a flat white plate at different MIGL resulted in a trade-off MIGL that yielded the highest accuracy for a single adjustment of MIGL that is uniform within and across the projected images.

The second method used several sets of images, taken at constant steps of MIGL, and combined the images pixel-by-pixel into a single set of composite images, by selecting the highest unsaturated intensities at each pixel. White plate measurements using this method had comparable accuracy to the first method but required more images to form the composite image. Measurement of a checkerboard showed a higher accuracy than the first method since the second method maintains a higher SNR when the object has a large range of reflectivity.

The last method also used composite images where the step size was determined dynamically, based on the estimated percentage of pixels that would become unsat-

urated at the next step. In measurements of a flat white plate and a checkerboard the dynamic step size was found to add flexibility to the measurement system compared to the constant steps using the second method. Using dynamic steps, the measurement system was able to measure objects with either a low or high range of reflectivity with high accuracy and without manually adjusting the step size. This permits fully automated measurement of unknown objects with variable reflectivity in unstructured environments with changing lighting conditions.

The methods can be used for measurement in uncontrolled environments, for specular surfaces, and those with a large range of reflectivity or luminance. This would allow a wider range of measurement applications using FPP techniques.

Acknowledgements

I would like to express my sincerest appreciation to Professor Jonathan Kofman for his support and guidance scholastically over the course of my masters research. I would also like to acknowledge the support of the University of Waterloo, the Ontario Graduate Scholarship in Science and Technology (OGSST) and Natural Sciences and Engineering Research Council (NSERC) of Canada for their financial support of this research.

Contents

List of Tables

List of Figures

Nomenclature

α combined effects of the aperture and exposure time referred to as camera sensitivity, 28

$\bar{\phi}_c$ average of the phase of pixels along the zero phase centerline, 18

$\breve{I}_i(x, y)$ ith phase-shift of the composite image for the LPA and DPA method, 64

$\Delta\phi(x, y)$ difference in object phase map and reference phase map, 16

$\Delta\phi_j(x, y)$ Phase difference between object and reference at jth position from reference plane, 19

δ_i ith phase shift, 12

γ projector nonlinearity, 20

$\hat{\gamma}$ estimate of projector nonlinearity, 20

$\hat{\varepsilon}$ estimated error when determining the unknown saturated intensity, 85

$\hat{I}_i(x, y)$ unknown saturated intensity estimate, 84

Ω solid angle, 7

$\phi(x, y)$ phase map for sinusoidal fringe pattern, 12

$\phi_a(x, y)$ absolute phase map, 18

$\phi_j(x, y)$ phase map at the jth position from the reference plane, 19

$\phi_n(x, y)$ phase at the nth row of the zero phase centerline, 18

$\phi_{obj}(x, y)$ object phase map, 16

$\phi_{ref}(x, y)$ reference phase map, 16

$\psi(x, y)$ data modulation, 28

σ standard deviation, 54

θ angle between the surface normal and the specified direction, 7

A area of the the illuminated surface, 7

$a(x, y)$ background intensity of the fringe pattern, 12

$a_1(x, y)$ incident ambient light reflected into the camera, 27

$a_2(x, y)$ ambient light that enters the camera directly from the environment, 28

B camera bit-level, 27

$b(x, y)$ amplitude of modulation of the fringe pattern, 12

$D(x, y)$ intensity distribution added to the original captured image for simulation, 53

F luminous flux, 7

$h(x, y)$ height map of object in millimeters, 16

$h_j(x, y)$ height map at the jth position from the reference plane, 19

$I''(x, y)$ average intensity, 28

$I'(x, y)$ intensity modulation, 28

$I_i^{(k)}(x, y)$ ith phase-shifted image captured at k MIGL, 64

$I_i^{**}(x, y)$ ith phase shift of the unknown saturated intensity map, 84

$I_i^{*}(x, y)$ modified image for simulation of the ith phase shift from the original captured image, 53

$I_{high}(x, y)$ highest captured intensity of the N phase-shifts at pixel x, y, 14

$I_i(x, y)$ ith phase shifted fringe image, 12

$I_{low}(x, y)$ lowest captured intensity of the N phase-shifts at pixel x, y, 14

$I_{max}(x, y)$ maximum input gray level of the fringe pattern to the projector, 14

$I_{med}(x, y)$ median captured intensity of the N phase-shifts at pixel x, y, 14

$I_{min}(x, y)$ minimum input gray level of the fringe pattern to the projector, 14

$I_m(x, y)$ difference between the maximum and minimum input intensities to the projector, 14

$K(x, y)$ least squares phase-to-height calibration map, 16

L_v luminance of an object, 7

M number of translation positions from the reference plane, 19

N number of phase shifts, 12

N_c number of pixels along the zero phase centerline, 18

$r(x, y)$ object surface reflectivity map, 27

$r_0(x, y)$ intensity ratio for the triangular fringe pattern, 14

S step size when using the LPA method, 64

T fringe pitch/period, 14

u normalized input pixel intensity, 20

w normalized output intensity from the projector, 20

Chapter 1

Introduction

Three-dimensional (3D) computer models have proven to be valuable tools in industry for product design, quality control, and research and development. An early method of 3D digitization is through the use of a coordinate measuring machine (CMM). This machine uses a touch triggered probe that is placed at several points along the surface of an object to obtain a coordinate point cloud. Surface fitting or interpolation through the data points is performed to obtain the 3D model of the object. Using touch sensors to digitize an object has proven to be very accurate; however, it is also very time consuming, the measurement data is sparse, and contacting the surface may deform or damage the part. Optical techniques for 3D digitization were later developed as a non-contacting solution to surface geometry measurement. This thesis focuses on improving one type of non-contacting optical 3D measurement technique. The need for such improvement is explained in the following sections, beginning with the general need for 3D optical surface measurement systems.

1.1 Need for optical 3D surface measurement

Systems capable of 3D surface measurement are used for many applications and in a wide variety of industries. Some of the more common applications are part inspection, reverse engineering, and object or scene modeling. More recently, there have been advancements in technologies related to computer vision that use 3D surface measurement systems including: stereoscopic displays, face and object recognition, augmented reality displays, and autonomous navigation. This section discusses these applications and how they use 3D digitization to solve problems.

1.1.1 Part inspection

Part inspection involves measuring the 3D features of an actual part for quality assurance during a manufacturing process. The captured 3D model of the object is compared with a CAD model to determine if the part is within the design tolerances and specifications. Part inspection is used on a wide range of objects including car parts [1] and solder joints [2, 3]. Due to the non-contacting nature of optical 3D measurement, automatic online inspection on an assembly line has been used to ensure part quality such as measuring dents and paint thickness for defects [4].

1.1.2 Object and scene modeling

A captured 3D model can be manipulated and rendered in a computer generated scene for testing or interfacing to a new CAD part. For example, a 3D model may be used to create a custom fit of a prosthetic limb for an amputee [5]. Optical 3D measurement systems have also been used in the medical industry for diagnosing deformities ranging from orthopedics, breast cancer, and plastic surgery [6]. Halioua and Liu [6] developed such a system for diagnosing spinal and postural deformity.

1.1.3 Reverse engineering

Digitization of an object to create a 3D model is often used for redesigning or reverse engineering a part that already exists. Typical parts range from tool and die making for manufacturing to biomedical device design such as orthoses and prostheses [7]. Sansoni and Docchio [7] used optical techniques to digitize the car body of a Ferrari. Carbone et al. [8] demonstrated on a door handle and a turbine blade that optical techniques can be used in tandem with a CMM for higher accuracy measurements in a few hours, compared to purely optical techniques that are calculated in a few minutes.

1.1.4 Stereoscopic displays

More recently, optical techniques and knowledge of visual perception has been used to create more accurate stereoscopic displays. This new technology uses a depth map, the depth at each pixel, along with the color image. Separate left and right images based on the depth map are directed into the observer's appropriate eye using polarized spectacles to give the appearance of a 3D scene [9]. Stoykova et al. [10] survey the various methods used to obtain the depth map for stereoscopic displays including methods using the original 2D film and structured light techniques.

1.1.5 Face and object recognition

Captured 3D data of an object have been used successfully for features in object [11, 12] or biometric face recognition [13, 14]. Industries that use this technology include: security [14], augmented reality [12], and robot artificial intelligence. Augmented reality is the overlaying of graphics onto a video stream, where the graphics can be manipulated and oriented from the perspective of an observer. Recognition, combined with visual tracking is used to anchor the graphic object in the scene as it moves [12]. Potential applications of this technology include: robotic manipulation [12], assisted navigation or assistance with other complex tasks such as surgery [15]. However, there are still challenges with depth of field, acquisition time, and gathering the 3D data robustly. Often there are "holes" or "spikes" due to the sensor being unable to acquire the data [13], and this adversely affects recognition.

1.1.6 Autonomous navigation

The use of 3D sensors is an integral part of simultaneous localization and mapping (SLAM) [16, 17] which is used to build a map of an unknown environment from recognition of landmarks while also keeping track of the sensor's current location within the map. This is a very active field in robotics for the purpose of autonomous navigation of robots, and obstacle detection for vehicle guidance [4]. Salvi et al. [18] present a review of the advantages and constraints for using optical measurement techniques utilizing structured light for the purpose of autonomous navigation. Among the limitations of utilizing structured light for autonomous navigation are: measurement of specular or metallic surfaces, reflection of a pattern onto another surface, and measuring surfaces with geometric surface discontinuities [18].

1.2 Overview of optical measurement techniques

Optical measurement techniques can be approximately classified into two groups: active and passive. Both active and passive techniques may use triangulation between the object, a camera, and at least one other camera or light source at a different and known pose. The difference between active and passive methods is that passive methods capture light that already exists in the scene during a measurement, while active methods add light to the scene as part of the measurement system [19]. The added light may be in the form of a laser [20] or direct light source with a known position relative to the camera and pattern. By projecting a known light source, active methods can have higher accuracy and faster processing than their passive

alternative. Adding light is especially effective for measuring surfaces that would otherwise be featureless due to lack of variation in structure, texture, shading, or color. However, adding light to the scene can introduce some limitations on what can be measured, for instance, specular surfaces, which have high reflectivity.

Some of the common passive and active methods that use triangulation for 3D digitization of object surfaces are described along with their limitations in Section 1.2.1 and 1.2.2, respectively. A more detailed review of general 3D shape measurement techniques can be found in [4] and in [21]; the latter focuses more on structured light techniques.

1.2.1 Passive techniques

Binocular or stereo vision is the most common passive method for obtaining 3D surface geometry information of an object or scene [21, 22]. The method makes use of triangulation between two or more cameras and the overlapping observable area in the scene as viewed by the camera(s). Prior to measurement, the cameras are calibrated by observing a known object that has point features at precisely known positions from one another [23]. The essential and most difficult step of calibration and measurement is matching corresponding pixels between images captured at the same time in the overlapping observable area of the cameras. This problem is often referred to as the correspondence problem [24]. To simplify the correspondence problem during calibration, the calibration object is composed of high contrast point features compared to the background. A popular calibration object is a black and white checkerboard with the point features being the intersections of the squares. This object is used by Bouget's camera calibration toolbox for MATLAB ($>$ v.5.0) [23] and in the open source computer vision library (OpenCV) ($>$ v.1.0) [25]. The calibration is used to determine the intrinsic parameters of the cameras and extrinsic parameters between the cameras. The intrinsic parameters include the focal length, principal point, and camera distortion parameters. The intrinsic parameters are used to relate pixel coordinates to coordinates in the world. The extrinsic parameters include the rotations and translations to map one camera to the other camera(s). This is used in triangulating the depth. Computing the correspondence points between images for a measurement is much more difficult and computationally expensive during measurement since corresponding pixels do not often have high contrast, which would help in obtaining an accurate measurements. Since the correspondence problem can be very computationally expensive and must be solved, obtaining a dense 3D surface measurement in real-time is not feasible without high performance computers [24, 26].

Rather than using stereo cameras and matching corresponding image pixels, one of the cameras can be replaced with a light source. In this case, the triangulation

is fundamentally the same but the correspondences can be observed in the captured images, since the light that is projected onto the surface at any point is detectable in the image. Passive approaches that use triangulation between the naturally occurring light and a camera are often referred to as "shape from" methods. These methods are based on a lighting model [27, 28] and the goal is to solve for the surface normal from the shading [29, 30, 31], shadows [32], or specular reflection [27]. While the correspondences do not have to be made between images, the difficulty lies in determining the position of the light source with respect to the camera. This requires multiple views [33, 32] or a calibration object [34] with known surface and lighting properties. Many assumptions are made to simplify the problem of "shape from" methods such as the light source being infinitely far away so that light rays are parallel, the light emanates from a single point, and the surface is Lambertian (apparent brightness of the surface to an observer is the same regardless of the observer's angle of view) [35]. These "shape from" methods can result in dense 3D surface measurement data but they are typically limited to measurement of simple objects with a uniform surface reflectivity where the shading, shadows, and specular reflections can easily be determined.

1.2.2 Active techniques

The active alternative to passive "shape from" methods are structured lighting techniques. These techniques often use a laser or a periodic intensity light pattern rather than a diffuse light source. This makes it easier to distinguish measurement points and reduces the effect of noise from the camera and the projector during measurement. It also makes the principle of triangulation clearly visible in the captured image used for measurement, since the light profiles are distorted according to the topography of the object as observed by the camera.

One advantage of using laser lines is that a bandpass filter can be used to eliminate environmental lighting effects. This helps when segmenting a laser profile in the captured image. The problem with using lasers for structured lighting techniques is that multiple captured images of the laser profile shifted across the object are required to acquire enough data to compute the surface coordinates of the entire object. Once the data is retrieved, the 3D coordinates between profiles can be computed through interpolation by surface fitting. This can cause important details to be ignored if the profiles are too far apart. Alternatively, profiles can be acquired with very high resolution, when scanning the laser across the surface. However, this makes the surface coordinate data acquisition very time consuming. The processing associated with capturing multiple frames can be reduced by projecting multiple laser lines onto an object, however, the spatial accuracy of the measurement is still limited [20] and interpolation between profiles may still be needed.

By using a light projector to project a continuous intensity light pattern that completely fills a camera image, the 3D coordinates can be found for each pixel. This is referred to as a full-field technique. There are a number of light patterns that have been used for full-field surface measurement including binary light [36, 37], moiré [4], De Bruijn [37], multi-color [37, 38], and fringe patterns. A fringe pattern is a periodic pattern that varies in intensity across the image. Trapezoidal [39, 40], triangular [41, 42], and most commonly, sinusoidal intensity profile patterns are used for fringe-pattern projection (FPP). Patterns are shown in Figure 1.1. A recent review of the various structured light techniques can be found in [43] and more specifically on FPP techniques in [44].

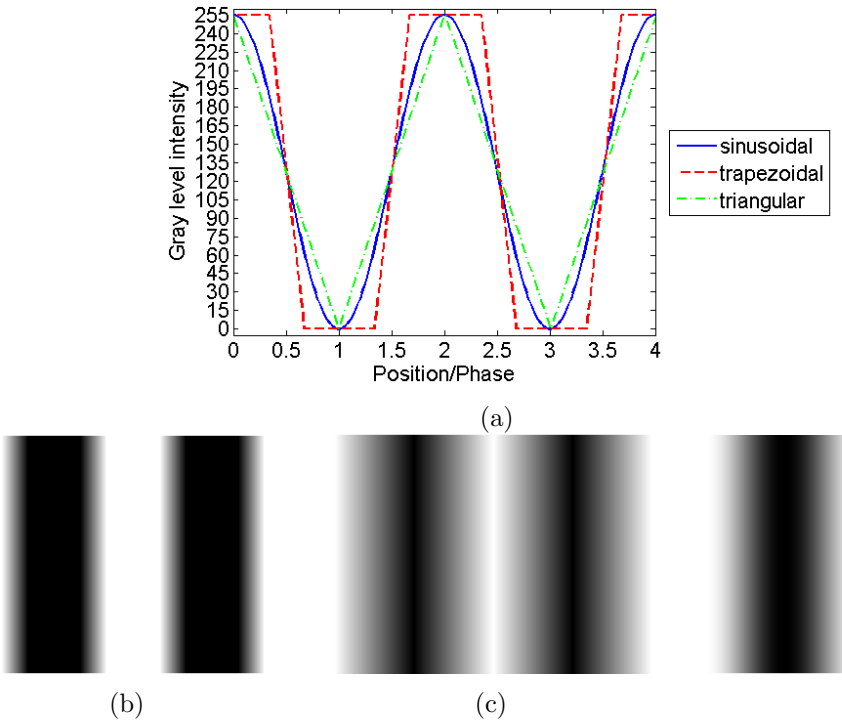

Figure 1.1: Fringe patterns shown in (a) with the same pattern period (pitch) and with (b) trapezoidal, (c) triangular and (d) sinusoidal waveforms.

In addition to being a full-field, non-contact, optical technique, FPP can achieve high accuracy (usually < 0.50 mm and as low as several microns root mean squared error (RMSE) depending on the setup) and is capable of real-time measurement [45]. Among the various FPP techniques, Fourier transform profilometry (FTP) [46, 47] has the advantage of allowing 3D surface measurement using a single projected pattern at the cost of accuracy [48]. Phase-shifting fringe-pattern projection (PSFPP)

techniques [4] achieve higher accuracy, especially for complex shapes [48], and are less sensitive to local surface reflectivity variations, and ambient light. However, the phase-shifting algorithm typically requires three to four patterns to be sequentially projected, and thus is not as fast as FTP. With high-speed digital projection of fringe patterns, phase-shifting techniques can still achieve real-time measurement [44, 49] using off-the-shelf components [50]. High frame rates were achieved by Zhang and Huang [45] by removing the color filter from the projector [51] and synchronizing a high speed camera with the projector. They were able to achieve measurements at 60 fps with a resolution of 640×480 pixels.

1.3 Problem definition

While PSFPP remains one of the most effective non-contact optical techniques for obtaining a dense full-field surface geometry measurement, it does have its limitations. One particular limitation occurs when performing measurements with a large range of luminance. Illuminance refers to the incident luminous flux (lumens) directed onto an object's surface, per unit area in units of lux (lx) [35]. Luminance is the light reflected from the object's surface in a particular direction as follows [35]:

$$L_v = \frac{\partial^2 F}{\partial A \partial \Omega \cos\theta} \tag{1.1}$$

where F is the luminous flux, θ is the angle between the surface normal and the specified direction, A is the area of the illuminated surface and Ω is the solid angle. Luminance depends on the intensity of the incident light to the surface (ambient light), the reflectivity of the object's surface (ratio of incident light reflected from surface) and the pose of the observer or camera with respect to the object. The camera can control the amount of luminance that is captured by adjusting the aperture and/or the exposure time. However, if there is a large range or high level of luminance from the object surface then the correct intensity may not be captured by the camera for certain settings of the aperture and/or exposure time. This is referred to as camera sensor saturation.

Camera sensor saturation causes loss of information when the light intensity directed to the camera exceeds the maximum intensity quantization level (maximum gray level) that the camera can acquire. When this occurs, the pixel intensity is captured as the maximum gray level of the camera. This has the effect of capturing an incorrect pattern in some portion of the captured image. This effect can be observed in Figure 1.2 which shows a sinusoidal fringe pattern with different levels of added ambient light ranging from 100 lx to 900 lx in 100 lx increments. As the luminance

increases, the peak intensities begin to saturate at the maximum gray level of 255. This is evident by the flat portion at the peaks of the pattern above 300 lx. Intensity saturation results in measurement error since the correct camera captured intensity, which is needed to compute the height, is not known.

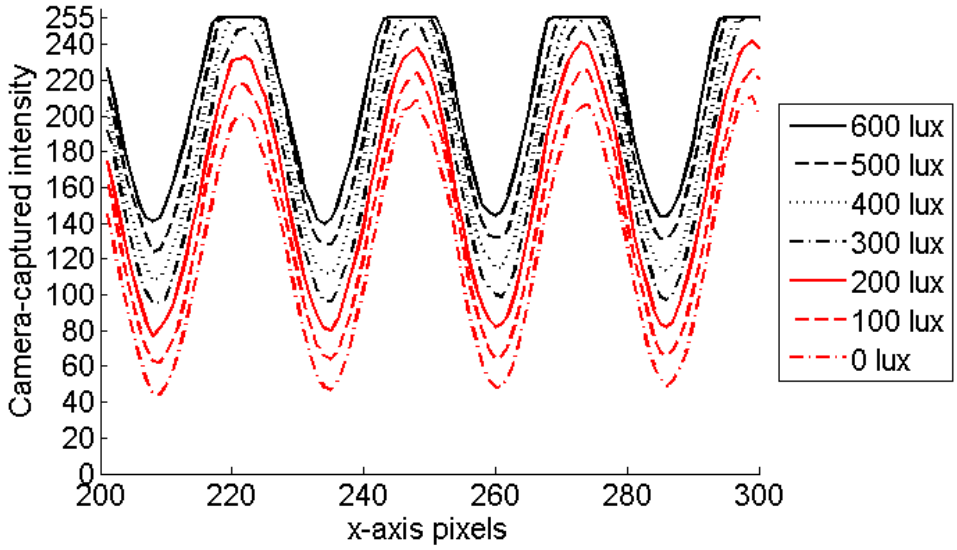

Figure 1.2: Several sinusoidal fringe patterns captured with incremental additions of 100 lx of ambient light added to the scene. Note the effect of saturation of the pattern as the added light causes the luminance to increase.

One problem that compounds the problem of saturation is that a low level of luminance for a specific setting of the aperture and/or exposure time will result in a low signal-to-noise ratio (SNR). The SNR refers to the intensity modulation of the captured pattern compared to the amount of noise that is compounded from the camera, projector and environmental lighting as part of the PSFPP process. The sources of noise may include ambient light, shadowing, projector illumination noise, camera/projector flicker, camera noise, and quantization error in the frame grabber and the projector [52]. The noise is modeled as a zero-mean Gaussian distribution as in [52, 53]. Intensity modulation refers to the amplitude of the periodic fluctuation from the average intensity of the fringe pattern. When the SNR is low, the fringe intensities are less distinguishable and the noise causes the captured intensities to have error.

In many cases, camera sensor saturation and low SNR can be dealt with by adjusting the camera aperture. However, this task is difficult to perform automatically, and a change in aperture or exposure time may require re-calibration for an accurate measurement. Being able to automatically make adjustments to avoid saturation and

low SNR will improve the ability to measure a wider range of objects. This may lead to more widespread industrialization and new applications for 3D measurement using PSFPP. In summary, the problem addressed in this thesis is adjustment of the surface measurement system for saturation avoidance when measuring surfaces with a large change in luminance from the object surface between measurements and/or a large range of luminance from the object surface during measurement. This will improve measurement accuracy when measuring in uncontrolled environments or objects with a large range of reflectivity.

1.4 Research goal

The goal of the research is to develop measurement techniques that will improve measurement accuracy compared to conventional measurement when there is a large change in luminance from an object surface between measurements or a large range of luminance during measurement that causes significant saturation and/or a low SNR. In addition, the method of saturation avoidance should meet the following requirements:

1. The method should not require special or additional hardware. The surface measurement system should therefore be able to perform measurement with any off-the-shelf components.
2. Saturation should be avoided so that the accuracy of the measurements with luminance that would cause saturation should be comparable to that when luminance is low such that saturation does not occur.
3. The method should not require any changes to the surface properties of the object that would affect the luminance from an object surface.
4. The method should have no affect on the PSFPP measurement method if saturation does not occur.
5. The method should be able to adaptively adjust based on the level or amount of intensity saturation observed in the image for efficient measurement.

1.5 Thesis outline

Before exploring the main contributions of this thesis, background information on PSFPP using a triangular and sinusoidal fringe pattern is presented in Chapter 2. A

literature review, mathematical theory, and the newly-developed approach to formulate three different methods for saturation avoidance is discussed in Chapter 3. The first method processes the entire image uniformly to avoid saturation. This method is tested using real and simulated measurements to analyze the error due to camera sensor saturation and low SNR in Chapter 4. This method is improved upon in Chapter 5 by avoiding saturation pixel-by-pixel using linear adjustments. In addition to saturation avoidance, processing the image pixel-wise helps maintain a high SNR. Rather than making linear adjustments, adaptive adjustments based on the observed saturation are made using the method of saturation avoidance presented in Chapter 6. The thesis concludes with a discussion of future work in Chapter 7 and conclusions in Chapter 8.

Chapter 2

Review of 3D Surface Measurement by Phase-Shifting Fringe-Pattern Projection

This chapter provides background on 3D surface measurement using the phase-shifting fringe-pattern projection (PSFPP) technique. The chapter begins be defining the two types of fringe patterns used in this thesis: sinusoidal (Section 2.2) and triangular (Section 2.3) patterns. The 3D surface measurement process by PSFPP is summarized in Section 2.4. This is followed by the calibration procedure that is used to compute the object surface height or depth, in Section 2.5. The nonlinearity of the projector intensities is discussed in Section 2.6 along with the method used in this thesis for correcting the nonlinearity to improve measurement accuracy.

2.1 Fringe-pattern projection setup

A PSFPP system typically consists of a digital projector, computer with an image capture capability, and a camera (Fig. 2.1). A computer is used to generate the several phase-shifted fringe patterns and controls the switching between the different phase-shifts. The projector is used to project the phase-shifted fringe patterns onto the object surface. A digital camera captures each of the projected phase-shifted fringe patterns. From the camera's perspective, the fringe patterns appear distorted according to the topography of the object. Once the camera has captured each of the phase-shifted images, the height (depth) of the object can be computed for each pixel using the method and equations discussed in Section 2.2 or 2.3, for the sinusoidal and triangular patterns, respectively.

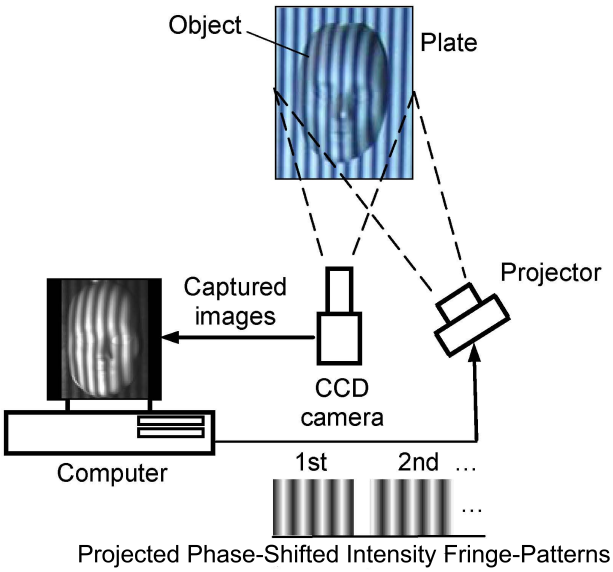

Figure 2.1: Schematic diagram of a 3D surface measurement system using fringe-pattern projection. (adapted from [54])

2.2 Sinusoidal fringe-pattern projection

The general expression for the distorted sinusoidal-intensity fringe pattern (Fig. 2.2) observed by a camera after being projected onto an object surface is as follows [6]:

$$I_i(x,y) = a(x,y) + b(x,y)cos[\phi(x,y) + \delta_i], \qquad i = 1,2,3,...N \tag{2.1}$$

The three unknowns, $a(x,y)\epsilon[0,1]$, $b(x,y)\epsilon[0,1]$, and $\phi(x,y)$ are respectively: the background intensity, amplitude of modulation, and phase at each image coordinate (x,y). The phase map, $\phi(x,y)$, contains the depth information of the object. This unknown map with N phase shifts indexed by i is solved using the following [6]:

$$\phi(x,y) = -\arctan\frac{\sum_{i=1}^{N} I_i(x,y)\sin(\delta_i)}{\sum_{i=1}^{N} I_i(x,y)\cos(\delta_i)} \tag{2.2}$$

The gray level intensity of the ith phase shift, $I_i(x,y)$, is detected by the CCD camera and δ_i is the phase shift, expressed according to the following [6]:

$$\delta_i = \frac{2\pi i}{N}, \qquad i = 1,2,3,...N \tag{2.3}$$

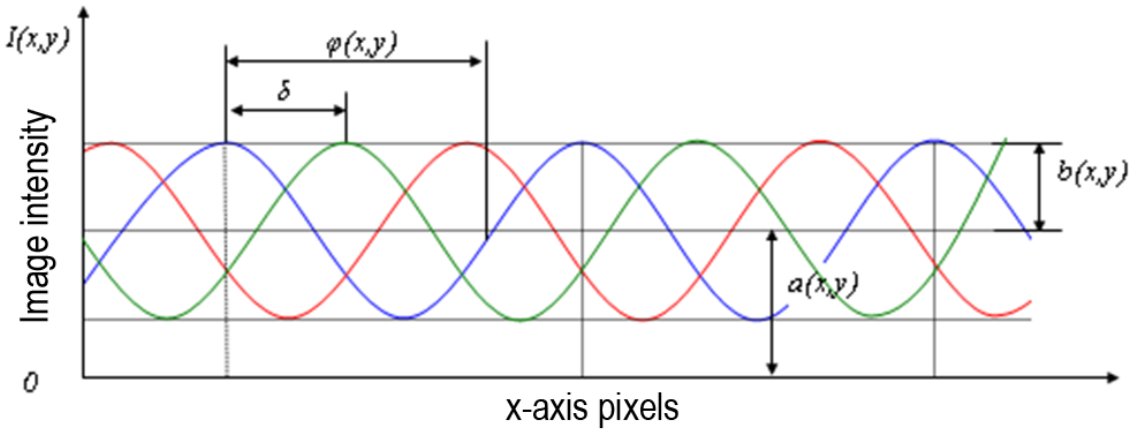

Figure 2.2: Sinusoidal pattern with three phase shifts 120°apart.

The minimum number of phase shifts required when using a sinusoidal pattern is three, one for each unknown. Thus, three equations in the form of Equation 2.1 are needed. The three patterns are sequentially projected by the projector and then captured by the camera. In the case when $N = 3$, there are several possible phase-shifts. The best accuracy is obtained when each phase shift is separated by 120°[55]. Equation 2.2 [6] can then be simplified to:

$$\phi(x,y) = -\arctan\left(\frac{\sqrt{3}I_3(x,y) - I_2(x,y)}{2I_1(x,y) - I_2(x,y) - I_3(x,y)}\right) \tag{2.4}$$

This yields the wrapped phase map $\phi(x,y)$ between 0 and 2π. The continuous phase map is obtained through a phase unwrapping [56, 57] algorithm. The phase-map is used to determine the object height as explained in Section 2.5.

2.3 Triangular fringe-pattern projection

The triangular fringe pattern (Fig. 2.3) has the advantage of requiring less processing than the more traditional sinusoidal fringe pattern [41]. This is because the minimum number of image acquisition steps is only two rather than the three needed for the sinusoidal fringe pattern. It also uses an intensity-ratio rather than the phase. Intensity ratio is less expensive to compute since it does not use the arctangent function as

in Equation 2.4. The N-step general expression for the projected triangular intensity fringe pattern is as follows [42, 54]:

$$I_i(x,y) = \begin{cases} \frac{2I_m(x,y)}{T}(x+\delta_i) + I_{\min}(x,y) + \frac{I_m(x,y)}{2} & x+\delta_i \epsilon \left[0, \frac{T}{4}\right) \\ -\frac{2I_m(x,y)}{T}(x+\delta_i) + I_{\min}(x,y) + \frac{3I_m(x,y)}{2} & x+\delta_i \epsilon \left[\frac{T}{4}, \frac{3T}{4}\right) \\ \frac{2I_m(x,y)}{T}(x+\delta_i) + I_{\min}(x,y) - \frac{3I_m(x,y)}{2} & x+\delta_i \epsilon \left[\frac{3T}{4}, T\right) \end{cases}$$

$$\begin{aligned} I_m(x,y) &= I_{max}(x,y) - I_{min}(x,y) \\ &= 2b(x,y) \end{aligned} \tag{2.6}$$

where $I_m(x,y)$ is the difference between the maximum ($I_{max}(x,y)$) and minimum ($I_{min}(x,y)$) intensities; T is the pitch or period of the pattern and δ_i is the shift according to Equation 2.7.

$$\delta_i = (i-1)\frac{T}{N}, \qquad i = 1, 2, ..., N \qquad N \geq 2 \tag{2.7}$$

Using more than the minimum number of steps improves the accuracy of the measurement at the expense of additional processing time for the additional images to be captured. To compare the effect of saturation on the number of steps, the triangular 3-step method is used in addition to the 2-step pattern for the analyses presented in this thesis. The equations for the intensity ratio $r_0(x,y)$ using the two-step [41] and three-step [42] triangular phase-shifting algorithm are shown in Equations 2.8 and 2.9, respectively. In the case of the 3-step equation, $I_{high}(x,y)$, $I_{med}(x,y)$, and I_{low} are respectively the highest, median, and lowest captured intensity at each image coordinate (x,y) of the three phase-shifted images.

$$r_0(x,y) = \frac{|I_1(x,y) - I_2(x,y)|}{I_m(x,y)} \tag{2.8}$$

$$r_0(x,y) = \frac{I_{high}(x,y) - I_{med}(x,y) + I_{low}(x,y) - I_{min}(x,y)}{I_m(x,y)} \tag{2.9}$$

The result from Equation 2.8 or 2.9 is wrapped from 0 to $2N$. This is shown in the cross-section of triangular pattern for the 2-step and 3-step algorithms along with the wrapped and unwrapped intensity ratio in Figure 2.3. The PSFPP process,

including the unwrapping algorithm and calibration procedure, is the same once the phase or intensity ratio is computed from Equation 2.2, 2.8 or 2.9, respectively for the sinusoidal and triangular patterns [58]. Since the process after computation of the intensity-ratio or phase is the same, for brevity, the remainder of the thesis refers only to the phase map, $\phi(x, y)$, which is used with the sinusoidal patterns. The same techniques are used with the triangular patterns, where $r_0(x, y)$, the intensity ratio map, would replace the phase map.

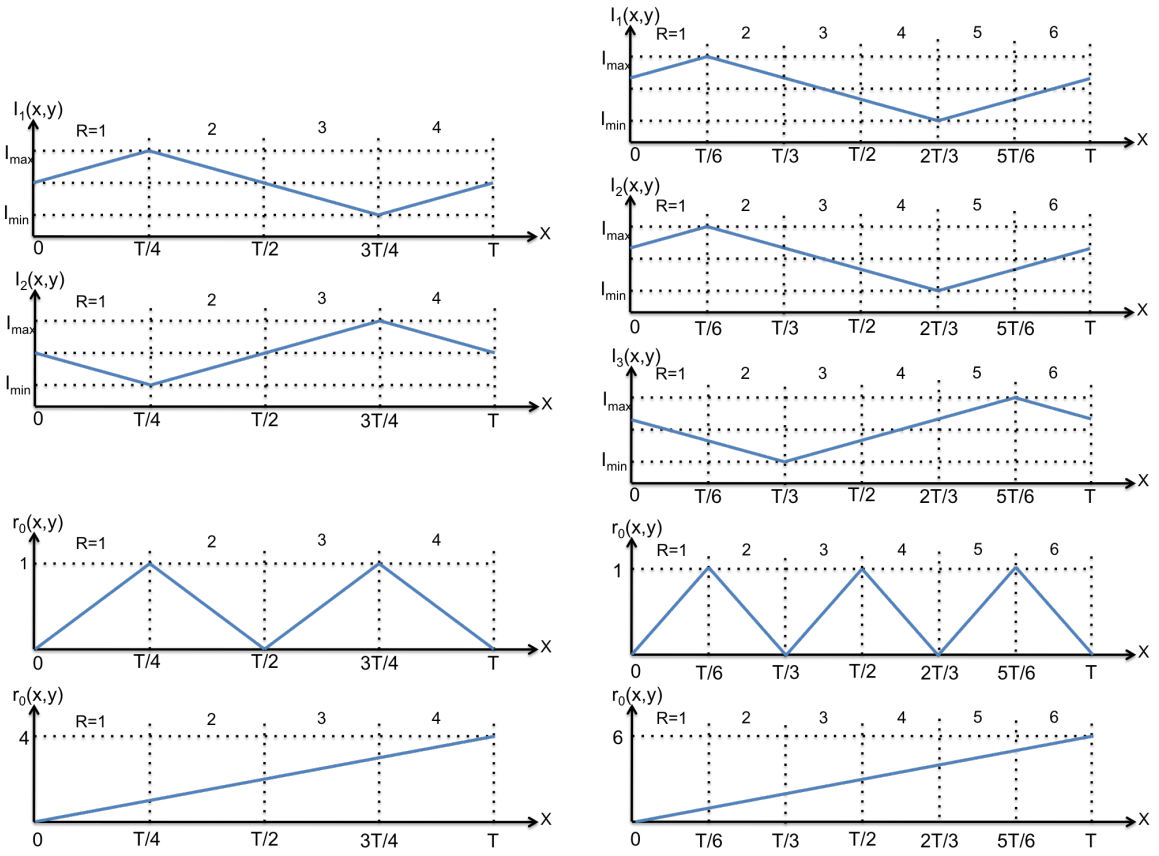

Figure 2.3: Cross-section of triangular fringe pattern: In the left column is the 2-step phase-shifted patterns while in the right column are the 3-step phase shifted patterns. The intensity ratio and the unwrapped intensity ratio are shown respectively under their set of phase-shifted patterns.(Adapted from [58])

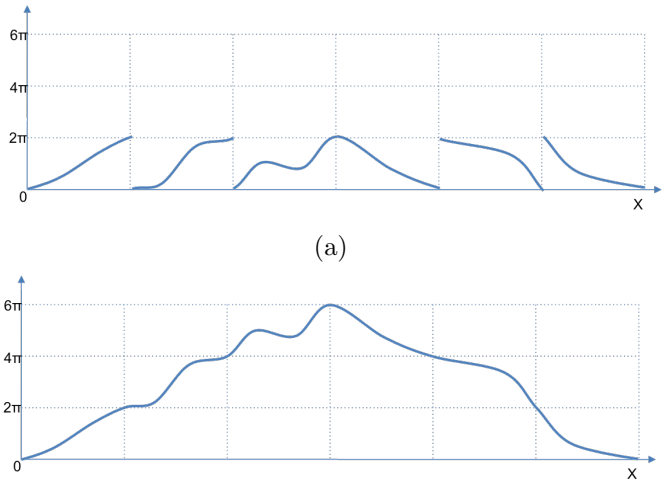

Figure 2.4: Unwrapping of an object where (a) is the wrapped pattern between 0 and 2π for the sinusoidal pattern or 0 and $2N$ for the triangular pattern and (b) is the unwrapped pattern.(Adapted from [58])

2.4 Measurement process

After applying the phase-shifting algorithm using the N phase-shifted images and computing the phase (Eq. 2.4 for phase and Eqs. 2.8 or 2.9 for intensity-ratio), the result is wrapped between 0 and 2π and from 0 to $2N$ respectively for the sinusoidal and triangular patterns. An unwrapping algorithm is used to convert the wrapped phase into a continuous phase-map. An example of phase unwrapping is shown in Figure 2.4. The details of the method of unwrapping can be reviewed in [56, 57, 58].

A continuous phase map is computed for both a reference plane and then for the object surface of interest. The surface height or depth is computed relative to this reference plane from the phase difference, which is computed according to Equation 2.10 [58].

$$\Delta\phi(x,y) = \phi_{obj}(x,y) - \phi_{ref}(x,y) \tag{2.10}$$

To compute the depth of the object, the phase-to-height map, $K(x,y)$, computed in Section 2.5, is multiplied pixel-wise with the phase-map according to Equation 2.11 to give the surface height. Figure 2.5 summarizes the different steps of the PSFPP measurement process.

$$h(x,y) = K(x,y)\Delta\phi(x,y) \tag{2.11}$$

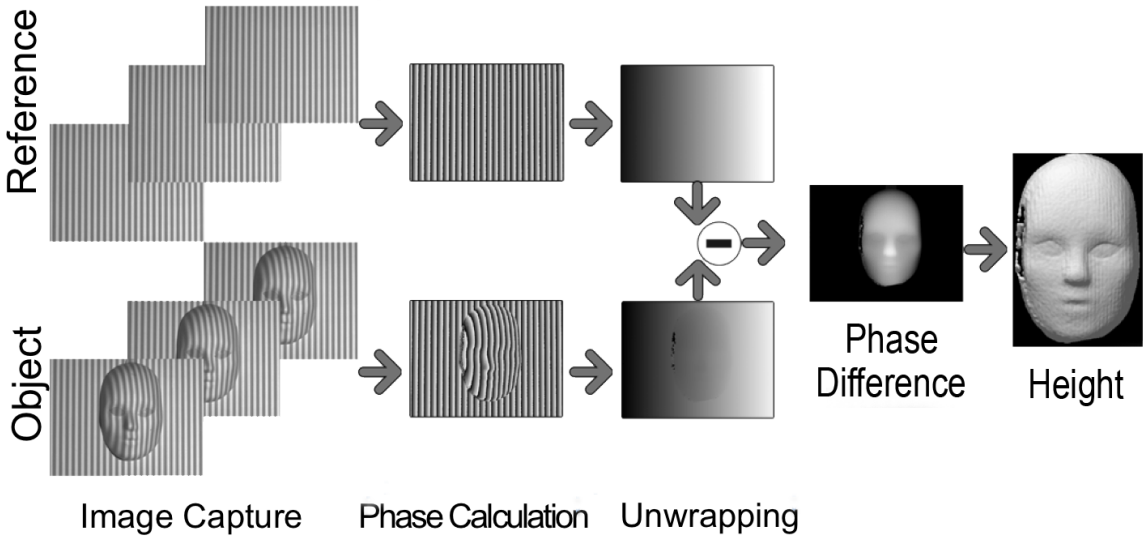

Figure 2.5: The phase shifting fringe-pattern surface measurement process requires a reference phase map and an object phase map. Using the captured phase-shifted images, the phase can be computed; however the result is wrapped between 0 and 2π. A phase unwrapping algorithm is used to obtain the continuous phase map. The difference between the object phase and the reference phase maps gives the phase difference. A measurement of the surface depth is computed by using a phase-to-height conversion based on an earlier calibration.

2.5 System calibration for phase-to-height mapping

The object surface height or depth is determined from the phase map using a phase-to-height (depth) conversion based on a calibration performed over the volume of interest prior to object measurement. The calibration method [58, 59] involves performing measurements by projecting the same phase-shifted patterns used during an object measurement onto a plane positioned at several precisely known distances along the Z-direction relative to a reference plane. A phase-to-height mapping is found for each image pixel based on the phase computed from the camera-captured grayscale image intensities.

When measuring a plane, the absolute phase must be computed to avoid the

measured phase from being wrapped over depth. This occurs because the periodic projected pattern is shifted from the perspective of the camera as the reference plane is repositioned at different depths. Computation of the correct phase requires a zero reference to compute the correct phase difference as discussed in the following section. A method to calculate the absolute phase, developed by Zhang and Huang [60], uses a projection of a separate centerline image onto the reference plane. The column of pixels in the middle of the centerline is considered as the zero phase reference. The average of the phase at these pixels, $\bar{\phi}_c$, is computed as follows [60]:

$$\bar{\phi}_c = \frac{\sum_{n=0}^{N_c} \phi_n(x,y)}{N_c} \tag{2.12}$$

where N_c is the number of pixels on the centerline and the subscript n denotes the phase of the nth row on the centerline. Using this result, the absolute phase, $\phi_a(x,y)$, can be computed by subtracting the average centerline phase, $\bar{\phi}_c$ from the "relative" phase, $\phi(x,y)$,(Eq. 2.4 for sinusoidal and Eq. 2.8 or 2.9 for triangular), as shown in Equation 2.13 [60].

$$\phi_a(x,y) = \phi(x,y) - \bar{\phi}_c \tag{2.13}$$

Once the absolute phase is computed for each of the measurement positions, the phase-to-height mapping can be obtained for each pixel using a linear least squares calibration model as follows [58]:

$$K(x,y) = \frac{\Delta\phi_j(x,y)}{h_j(x,y)} \qquad j = 1, 2, ...M \tag{2.14}$$

where $\Delta\phi_j$ is the phase difference (explained in Section 2.4) at the jth position from the reference plane. The coefficient $K(x,y)$ can be obtained from only one measurement position. However, it is good practice to use several measurement positions, M, over the control volume and compute the linear least squares fit according to [58]:

$$K(x,y) = \frac{\sum_{j=1}^{M} \Delta\phi_j(x,y) h_j(x,y)}{\sum_{j=1}^{M} \Delta\phi_j^2(x,y)} \tag{2.15}$$

Non-linear calibration models have also been used in the literature [61, 62]. The linear calibration model is used for the results presented in this thesis after performing an assessment between the linear and non-linear calibration models. A similar analysis

was also performed by Jia [59] using simulations and found that there was not a great difference between the linear and non-linear calibration models with a stand-off distance from the camera to the reference plane of 1.9 m.

Alternatively, a geometric model-based approach [63, 64, 65] can be used to determine the relationship between the phase and height. However, this is considerably more difficult and not necessarily more accurate since it requires that the intrinsic parameters of the projector and camera be known along with the extrinsic parameters between the camera and the projector. Although the projector cannot capture images like a camera, there are several methods [66, 63, 67] to determine these parameters. Zhang and Huang [60] use the camera to capture images for the projector and then transform the images so that it is as if the images were captured by the projector. Calibration of the projector is undertaken using the same procedure as the established method for camera calibration, which can be computed using Bouget's camera calibration toolbox [23]. Vargas et al. [67] perform calibration without a translation stage or computing the intrinsic and extrinsic parameters of the projector. This method is more appropriate for larger fields of view when a translation stage is not feasible.

2.6 Projector nonlinearity correction

One of the drawbacks of using a digital projector for 3D surface measurement using PSFPP is that the input gray level intensities of the computer generated images are mapped nonlinearly to the projected intensities. This causes the captured pattern to be distorted from the expected pattern shape. The effect varies between projectors and sometimes the graphics card [62], which purposely introduces the nonlinearity for a visually sharper image based on the human visual system [62]. Since the phase is computed based on the assumption that the phase-shifted fringe pattern has a certain shape (sinusoidal, or triangular), if not accounted for, the nonlinearity can result in significant measurement error. There are essentially two ways to correct the projector nonlinearity, before the projection [68] or after computing the phase [69, 70, 71, 72, 66, 62, 73].

The method used in this thesis corrects for the projector nonlinearity before the projection since this approach is slightly less computationally expensive and is independent of the camera aperture, fringe pattern pitch, camera pixel coordinate position, and the type of fringe pattern projected. This method is based on projecting the inverse of the projector nonlinearity function so that the mapping between the input intensities to the captured intensities is linear. The most common model used to represent the projector nonlinearity is an exponential as follows [62]:

$$w = u^{\gamma} \tag{2.16}$$

where $u \in [0, 1]$ denotes the normalized input pixel intensity, w is the normalized output intensity from the projector, and γ is the projector nonlinearity often referred to as "gamma". It has been argued that the projector nonlinearity is more complex than being modeled as a single parameter, however modern display technologies try to emulate the model from Equation 2.16 so that the images appear sharper to the human eye [62]. Typically the manufacturer sets γ to be greater than 1.0, and the standard of the National Television System Committee recommends γ to be at least 2.2 [62]. To linearize the relationship between the captured and projected intensities, an estimate of γ is needed so that the projected intensities behave as follows:

$$w = [u^{\gamma}]^{1/\hat{\gamma}} \tag{2.17}$$

where $\hat{\gamma}$ is the estimate of γ from Equation 2.16. Estimating the value of $\hat{\gamma}$ accurately using images captured by the camera requires modeling other illumination effects such as the ambient lighting, reflectivity, and slope of the measurement surface. Guo et al. [62] developed a method for estimating the projector nonlinearity from a captured sinusoidal fringe pattern using the model from Equation 2.16. This method was not found to produce accurate results, so instead $\hat{\gamma}$ was found through an iterative process of selecting a value for $\hat{\gamma}$ that causes the mapping between the input intensities to the captured intensities to be approximately linear. This selection process could be automated using an optimization method but since $\hat{\gamma}$ only needs to be computed once, this was not found to be necessary. Sufficiently accurate results were found after only a few iterations based on observations of the mapping between the projected and captured intensities as shown in Figure 2.6(b) and 2.6(c). The final value used for $\hat{\gamma}$ was estimated to be 2.812. A comparison of a measurement on a mask without compensating for the projector nonlinearity and then compensating for it using the estimate for $\hat{\gamma}$ is shown in Figure 2.7.

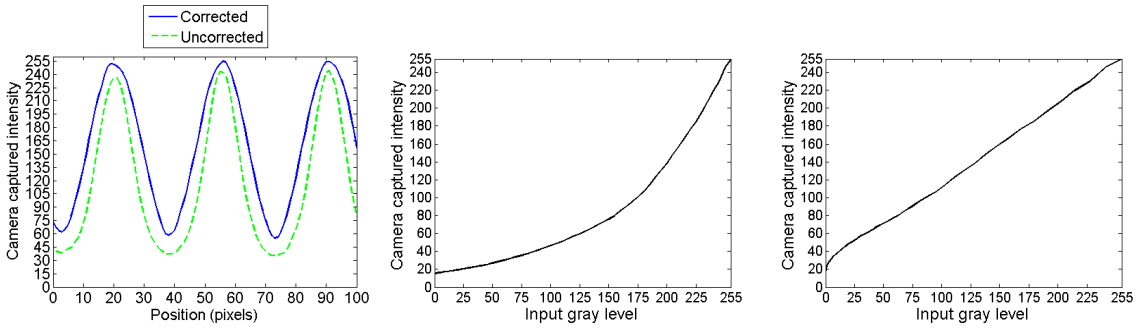

(a) (b) (c)

Figure 2.6: The effect of the projector nonlinearity on a fringe pattern. a) Comparison of the sinusoidal patterns with and without correction shows the effect of the nonlinearity when correction is not applied. The mapping of gray level intensities between the projector input and the camera b) without correction, and c) with correction.

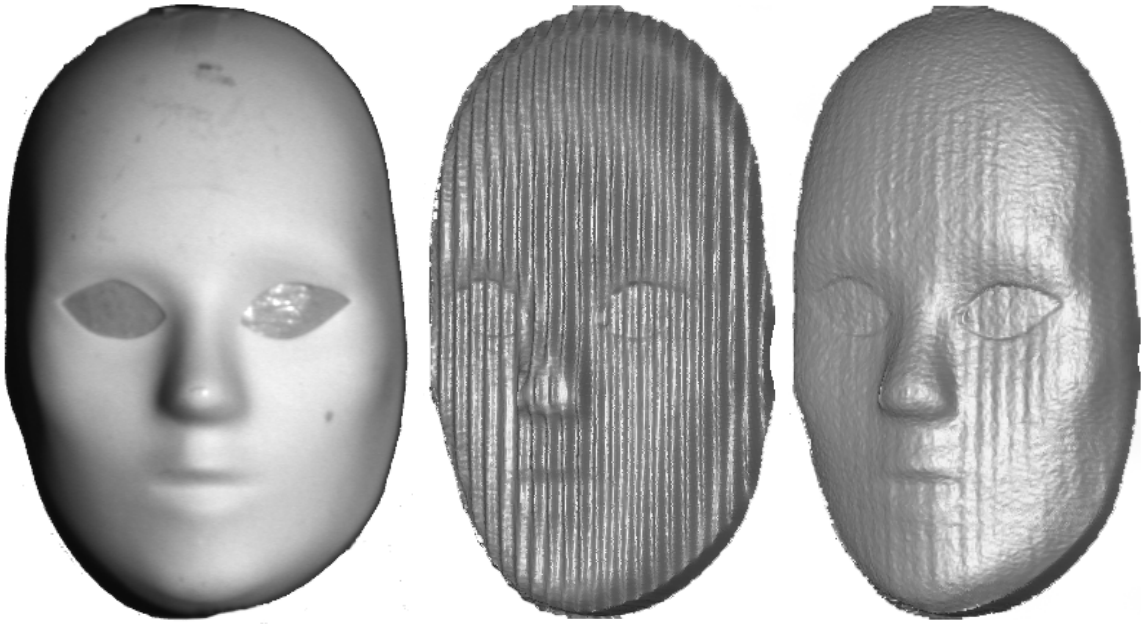

(a) (b) (c)

Figure 2.7: Reconstructed surfaces from measurement of a mask, shown in (a), showing b) projector nonlinearity which results in a ripple in the measured surface and c) nonlinearity correction which results in a much smoother surface. Both measurements where taken using the sinusoidal 3-step fringe pattern. A larger pitch of 21 pixels was used to demonstrate the effect of the nonlinearity.

Chapter 3

Intensity Saturation and Low SNR in PSFPP techniques

Errors due to saturation and low SNR are typically avoided by adjusting the camera aperture and/or exposure time. As discussed in Section 3.1, this alone is not enough to be able to perform an accurate measurement because of a trade-off that exists between robustness to intensity saturation or low SNR. A review of the literature that addresses this problem is discussed in Section 3.2. This is followed by mathematical theory to show the adjustments that can be made to avoid saturation and maintain a high SNR in Section 3.3. A new method of adjustment to avoid saturation is developed in Section 3.4 along with three methods of saturation avoidance to facilitate measurement when there is a large range or high level of luminance.

3.1 Trade-off between robustness to intensity saturation and low SNR

Error due to intensity saturation and low SNR depends on the level of luminance and the aperture setting of the camera. When choosing the appropriate aperture there exists a trade-off between the measurement system being robust to either intensity saturation or low SNR. For high robustness to saturation, one could choose a smaller aperture to permit a more accurate 3D surface measurement in the presence of bright ambient lighting that may cause intensity saturation. However, this small aperture setting may leave the captured image underexposed in some regions. Conversely, one could choose a large aperture with a high robustness to low SNR, which may leave the image overexposed in some regions. This may permit a more accurate 3D surface measurement in the presence of dim ambient lighting that may result in low SNR.

For a given aperture setting, saturation or low SNR may occur in two situations: 1) the level of luminance changes or 2) there is a large range of luminance entering the camera due to a large variation in surface reflectivity across the object, such as a checkerboard. An increase in the level of luminance causes the intensity modulation to increase, which may result in saturation. Conversely, a decrease in the level of luminance causes the intensity modulation to decrease, which may result in low SNR. In the situation with a large range of luminance, there may be regions in the image of both high and low intensity modulation, which may result in either or both intensity saturation and low SNR.

Regions of both high and low intensity modulation occur when measuring specular surfaces such as polished metals. As the ambient light or light from the projector is directed at the surface, most of the light is reflected in a single direction instead of diffusing the light like a Lambertian surface. This usually results in a region of the image with intensity saturation. The location of the intensity saturation depends on where the high intensity reflection is directed into the camera. The region of the image outside of where the intensity saturation occurs may have a low SNR since most of the light reflected from the surface at the corresponding pixel may not be directed into the camera. This gives a lower level of luminance compared to the region where the high intensity reflection is captured by the camera.

Most PSFPP measurement systems are able to avoid measurements with a change or large range of luminance by measuring in a controlled environment with controlled object surface properties. The desired controlled environment would have no change in lighting with the only source of light being the projector. With no change in luminance, the aperture is adjusted so that the peak intensity is close to the maximum gray level that can be captured by the camera for a high robustness to noise. The desired measurement surface properties are: a high level and low range in reflectivity. This can be controlled by painting the object surface with a matte white paint. This yields a high SNR since the light from the intensity fringe pattern is amplified by the surface reflectivity but is diffused by the surface so that there a low range of luminance. The reason why this surface is ideal is discussed later in Section 3.3. As a result of controlling the environment and surface properties of the system, there is no need to be robust to saturation since saturation should not occur. Thus, high measurement accuracy can be achieved with a high robustness to noise and high SNR.

While using a controlled setup achieves high measurement accuracy it also places limitations on where measurements can take place and the types of surfaces that can be measured. Eliminating these limitations may lead to more widespread industrialization and new applications of 3D surface measurement. This is because certain applications might have to be conducted in uncontrolled environments such as forensic, medical, or archaeological sites where the lighting options may be limited

and the surface properties cannot be altered. As well, certain applications may need measurement of surfaces with a large range of luminance without altering the surface properties, such as inspection for car parts [1] or solder joints [2, 3]. To eliminate these limitations, adjustments must be made during measurement to avoid saturation and seek the trade-off point that maximizes robustness to intensity saturation and low SNR. While this may be done manually by re-adjusting the aperture, the adjustment should be done automatically since manual adjustment limits the use of PSFPP in certain applications, such as autonomous navigation. The following section reviews some of the research that has been published to improve measurement of objects susceptible to saturation.

3.2 Literature review

There has not been much research specifically on the trade-off between robustness to intensity saturation and low SNR but many papers have identified the need for measuring specular surfaces. This section reviews some of the more recent and significant developments with a more general focus on performing 3D surface measurements in the presence of high ambient lighting and/or high surface reflectivity that may cause saturation.

One notable method for measuring a specular surface is presented by Jeong et al. [3] who use a Liquid Crystal Spatial Light Modulator (LC-SLM) between the camera and the scene, or object. This device restrains the incoming light intensity from exceeding the maximum quantization level so that the intensity information is not lost. Experimental measurements of specular solder-joints on a printed circuit board were performed to test the method. The results appeared reasonable but no errors were reported. While using additional hardware to solve the problem of measuring specular surfaces can be fast, it may not always be effective at measuring surfaces with different ranges of luminance and it adds cost to the system. Instead software-based approaches have more recently gathered much more interest.

Kowarschik et al. [74] recognized the trade-off between robustness to intensity saturation and low SNR based on the surface luminance from the perspective of the camera. They also stated that there is no single adjustment that can be made to address this trade-off when performing a measurement with a large range of luminance. The method developed by Kowarschik et al. was to perform measurements of an object or scene from different perspectives and then transform each measurement from its respective local coordinate system to a global coordinate system. At each perspective the captured gray level intensities changed so that, with enough measurements, the error due to low SNR and saturation was reduced. This also helped

address the issue of occlusion of surface points from the perspective of the projector or camera, which was another goal of their research. While this method may be effective at reducing the error from intensity saturation and low SNR for specular surfaces, capturing images from different view points adds considerable complexity and a difficult registration problem to avoid saturation. As well, a change of perspective may not be very effective at avoiding saturation when measuring surfaces that exhibit Lambertian behaviour, since the change in view would not result in a significant change in camera captured intensity.

Two methods for measuring specular surfaces using software were developed by Hu et al. [75]. The first method uses a single camera at multiple views along with a binary mask to block the specular region from being processed. In this method, the object is measured "patch by patch". This is a very time consuming procedure since the camera must be repositioned and re-calibrated. It also introduces a complicated registration issue between measurements at different viewing angles. The other method uses multiple cameras and color separation of color fringe patterns. Different regions have different color fringes and the cameras have a color filter to capture the desired pattern so that each camera simultaneously measures a specific area. While this method is faster than having multiple views, not all FPP systems use two cameras and both of these methods require that the shiny specular areas be known ahead of time to create the masks or the color pattern.

Other approaches [76, 77, 78] avoid saturation using a sinusoidal pattern by capturing more than the minimum number of phase-shifted images and ignoring the phase-shifted image pixels that are saturated. The phase is then calculated at each pixel using only the unsaturated phase-shifted image pixels. This limits the degree of saturation that can be avoided because no fewer than the minimum number of phase-shifted intensities can be saturated at a given pixel. The original work [77] only uses four phase-shifts, but this was later expanded to five shifts [76] and seven [78]. The algorithm was demonstrated in a simulation and experimentally on a simple cylindrically shaped surface. While this method helps to cope with the problem of saturation, it requires additional captured images that may not be necessary and it is limited to a certain level of saturation since the phase can only be computed if the minimum number of phase-shifted images are not saturated.

In the most complete work to date, Zhang and Yau [79] address the problem by capturing phase-shifted patterns at different camera exposure times and combining the different gray level intensities pixel-wise into a single set of phase-shifted images. This adaptive method avoids saturated image intensities by using the brightest unsaturated intensities among several captured images under different exposure times at each pixel. While this adaptive method is effective at avoiding saturation and maintaining a high SNR, capturing multiple images at different camera exposure times

is very time consuming. This is especially the case when it is not known how many sets of images are needed to accommodate the full range of luminance. As well, adjusting the camera exposure time may not be possible or practical for all off-the-shelf hardware.

3.3 Theory

The theory presented in this section explains the parameters that affect intensity saturation and SNR. The equations are based on the theory presented by Zhang and Yau [79] but they are modified from its original form to be more general so that it encompasses non-sinusoidal fringe patterns. The original work assumes a projected fringe image:

$$I(x,y) = a(x,y) + b(x,y)f(x) \tag{3.1}$$

where $a(x,y)$ is the background intensity and $b(x,y)$ is a multiplier that determines the amplitude of modulation, as shown in Figure 3.1, for the periodic function, $f(x)$. In the case of a sinusoidal pattern, $f(x)$ would be $\cos(x)$ as in [79], and $a(x,y)$ and $b(x,y)$ typically both have a value of approximately $(2^B-1)/2$, where B is the bit-level of the camera, and their sum equals the maximum input gray level (2^B-1) so that the projected fringe-pattern has the full range of projected intensities. The projected fringe-pattern and incident ambient light, $a_1(x,y)$, are reflected to the camera by the object surface with reflectivity, $r(x,y)$. The camera captured intensity from the reflection is as follows:

$$I(x,y) = r(x,y)[a(x,y) + b(x,y)f(x) + a_1(x,y)] \tag{3.2}$$

The reflected intensities along with ambient light that enters the camera directly from the environment, $a_2(x,y)$, rather than being reflected, are captured through the pupil of the camera and quantized into gray level values. The amount of light entering through the camera's pupil is controlled by the camera sensitivity, α, from combined effects of the aperture and exposure time. In some cameras, there may be a controllable gain, but for the widest application it is assumed here to be fixed (and controlled). The camera sensitivity, α, should be adjusted so that the captured intensity maps between 0 and the maximum intensity quantization level of the camera (255 for 8-bit camera) for it to be captured by the camera. The captured image of the fringe pattern can then be expressed as:

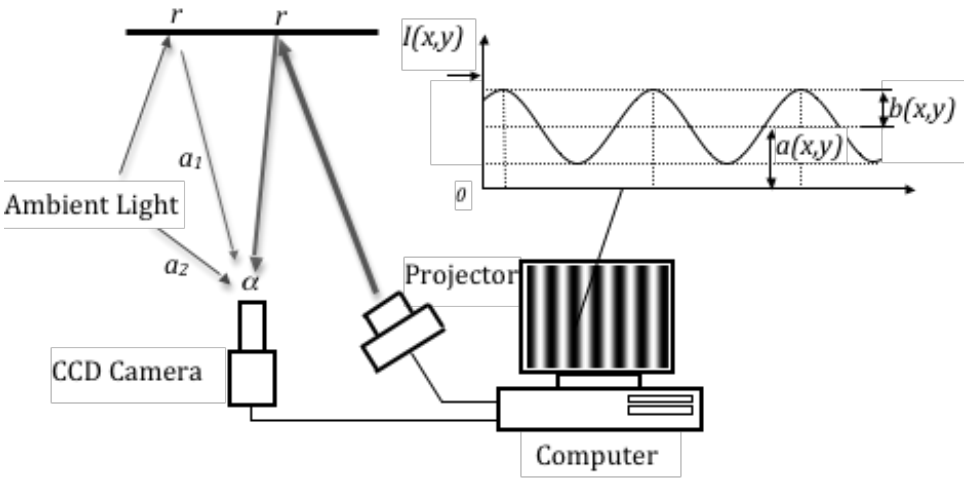

Figure 3.1: Sources of light in fringe pattern projection.

$$I(x,y) = \alpha r(x,y)[a(x,y) + b(x,y)f(x) + a_1(x,y)] + \alpha a_2(x,y) \tag{3.3}$$

the intensity modulation is

$$I'(x,y) = \alpha r(x,y)b(x,y) \tag{3.4}$$

the average intensity is

$$I''(x,y) = \alpha r(x,y)[a(x,y) + a_1(x,y)] + \alpha a_2(x,y) \tag{3.5}$$

and the data modulation is the intensity modulation divided by the average intensity.

$$\psi(x,y) = \frac{I'(x,y)}{I''(x,y)} = \frac{r(x,y)b(x,y)}{r(x,y)[a(x,y) + a_1(x,y)] + a_2(x,y)} \tag{3.6}$$

The data modulation (Eq. 3.6) is an important equation for determining the factors that affect the SNR. For a high SNR and accuracy, the data modulation should be close to one. This is the largest possible data modulation for the constraints on $a(x,y)$ and $b(x,y)$. A data modulation of one is only possible if there is no ambient light (reflected by the surface: $a_1(x,y) = 0$, directly entering camera: $a_2(x,y) = 0$) and $a(x,y)$ and $b(x,y)$ are equal to $(2^B - 1)/2$. If the reflectivity, $r(x,y)$, is very large

with respect to ambient light directly entering the camera, $a_2(x, y)$, then the data modulation equation is approximately equal to:

$$\psi(x, y) = \frac{I'(x, y)}{I''(x, y)} \approx \frac{b(x, y)}{a(x, y) + a_1(x, y)} \quad | \quad r(x, y) >> a_2(x, y) \tag{3.7}$$

which can cause the data modulation to be very close to one if $a_1(x, y)$ is negligible. If either $a_1(x, y)$ and $a_2(x, y)$ are large, then the denominator in the data modulation equation (Eq. 3.6) will also be large and this would result in a lower data modulation. This is why it is good practice to perform surface measurement and system calibration using a surface with a high level of luminance and in a dark room with negligible ambient lighting to obtain a higher quality fringe pattern.

While it may be good practice to use reflective objects to have a high data modulation, as discussed in Section 3.1, there may be environments where the reflectivity should not be controlled for saturation avoidance and low SNR since it limits the range of reflectivity of the object surfaces that can be measured. Likewise, it is not always practical that the ambient lighting be controlled since it limits where an object can be measured.

Zhang and Yau [79] chose to adjust the camera sensitivity, α, through the exposure time. This is an unobtrusive method since it does not limit the surfaces that can be measured or where measurement may take place. This method also has no effect on the data modulation, since α cancels out from the numerator and denominator in Equation 3.6. As well, the highest data-modulation, without controlling the ambient light or surface reflectivity, can always be maintained by setting the inputs $a(x, y)$ and $b(x, y)$ to the projector equal to $(2^B - 1)/2$. As mentioned in Section 3.2, while this method has been shown theoretically and experimentally to reduce error due to saturation, there are disadvantages in having to capture multiple images at different exposure time, and adjusting the camera exposure time may not be possible or practical for off-the-shelf cameras.

3.4 New gray level adjustment methods of saturation avoidance

This thesis presents, in this section, a new approach to saturation avoidance that has several advantages over previous methods. The newly-developed method is based on adjusting the maximum input gray level (MIGL), $I_{max}(x, y)$, to the projector while the minimum input gray level, $I_{min}(x, y)$, to the projector is fixed at a value close to

zero to yield a high data-modulation. This method is also unobtrusive since the MIGL does not depend on any parameters in the environment such as the object surface or the ambient lighting. Adjustment of the MIGL, $I_{max}(x, y)$, has several advantages over adjustment of α because only the projected pattern is modified, adjustment of MIGL is independent of the camera, and controlled purely in software. This allows for the adjustments to: 1) be very fine and easily repeatable 2) work with any camera hardware and 3) the degree of saturation is easier to quantify since it can be expressed in the same units of the camera captured intensity, gray level.

One of the problems with the MIGL adjustment method is that it is limited in range compared to adjustment of α. This is because adjustment of $I_{max}(x, y)$ is limited by the setting of α, which determines the range of observable intensities by the camera. However, if α is adjusted to a point so that lowering $I_{max}(x, y)$ causes the saturated intensities to be quantized by the camera then saturation can be avoided. This is because lowering $I_{max}(x, y)$ also lowers the luminance of the object at the corresponding point. Lowering the MIGL also decreases the amplitude of modulation of the input pattern to the projector as it approaches $I_{min}(x, y)$, which may result in a low SNR. The following section examines the theory behind the of MIGL to demonstrate that a high SNR can still be maintained. Section 3.4.2 discusses three methods of saturation avoidance that are developed in this thesis and explored in experiments presented in the following chapters. The experimental setup for these experiments is discussed in Section 3.4.3.

3.4.1 Theory of MIGL adjustment

This section presents newly-developed theory to examine whether adjustment of the MIGL maintains a high data modulation, and thus high SNR. The relationship between $a(x, y)$ and $b(x, y)$ to $I_{max}(x, y)$ and $I_{min}(x, y)$ is expressed as follows:

$$a(x, y) = \frac{I_{max}(x, y) + I_{min}(x, y)}{2} \tag{3.8}$$

$$b(x, y) = \frac{I_{max}(x, y) - I_{min}(x, y)}{2} \tag{3.9}$$

with the constraint

$$I_{max}(x, y) - I_{min}(x, y) \leq 2^B - 1 \tag{3.10}$$

Equation 3.8 and 3.9 can be substituted into Equation 3.6 to yield:

$$\psi(x,y) = \frac{I'(x,y)}{I''(x,y)} = \frac{r(x,y)[I_{max}(x,y) - I_{min}(x,y)]}{r(x,y)[I_{max}(x,y) + I_{min}(x,y) + 2a_1(x,y)] + 2a_2(x,y)} \quad (3.11)$$

Equation 3.11 can be simplified with $I_{min}(x,y)$ equal to zero as shown in Equation 3.12.

$$\psi(x,y) = \frac{I'(x,y)}{I''(x,y)} = \frac{r(x,y)[I_{max}(x,y)]}{r(x,y)[I_{max}(x,y) + 2a_1(x,y)] + 2a_2(x,y)} \quad (3.12)$$

Substituting $I_{max}(x,y)$ and $I_{min}(x,y)$ into Equation 3.6 is also a more general representation when using non-sinusoidal fringe-patterns. From Equation 3.12, it can be seen that lowering $I_{max}(x,y)$ would cause the intensity modulation to decrease and result in a low data modulation if there would be a low reflectivity and the ambient light reflected by the surface, $a_1(x,y)$, and entering the camera directly, $a_2(x,y)$, would have some positive non-zero value. This would adversely affect the measurement accuracy. However, this equation does not model camera sensor saturation and thus does not show that there is an upper limit to the intensity modulation. By lowering the MIGL, $I_{max}(x,y)$, the level of luminance is also lowered so that the camera can capture the correct unsaturated intensity. The point where all of the phase-shifted intensities for a given pixel becomes unsaturated represents the highest data modulation for that pixel. Therefore, each saturated pixel has some value of MIGL were it becomes unsaturated and has a high data modulation, and thus high SNR. This value at each pixel depends on the corresponding reflectivity of the surface at that pixel. This is because a high reflectivity amplifies the amplitude of modulation of the fringe pattern that is input to the projector. However, if there is a small range between the maximum and minimum input gray level then there is a greater sensitivity to having a high data modulation due to effects of ambient light. This is because a variances, or noise, in the ambient light are also amplified by the reflectivity and compounded with the projected fringe pattern. If the projected amplitude of modulation of the fringe pattern is small then this noise adds greater variance to the intensities captured by the camera. The effects of noise due to ambient lighting on measurement error is explored through experiments presented in this thesis.

3.4.2 MIGL adjustment methods of saturation avoidance

Three new methods of saturation avoidance are presented in this thesis for PSFPP techniques for 3D surface measurement. The three methods are based on the general approach of adjusting the MIGL. There is a natural progression between each of

the methods of saturation avoidance discussed in the following chapters to improve performance in a specific area. No particular method is superior in all aspects of measurement as each method has its advantages and disadvantages for different surface measurement situations.

Non-adaptive uniform adjustment of MIGL method

The first method is referred to as the non-adaptive uniform adjustment of MIGL technique and is discussed in Chapter 4. This technique is based on finding the point with the best trade-off of robustness to saturation and low SNR at a single setting of MIGL. Once this trade-off point is determined, then measurement can be performed without the need for adjustment of MIGL and the PSFPP measurement process can continue as usual. This technique should be effective at measuring when there is a low range of luminance during measurement because all pixels are treated uniformly.

Linear pixel-wise adaptive method

The second method (detailed in Chapter 5) maintains a high SNR when possible by avoiding saturation on a pixel-by-pixel basis. This method is referred to as the linear pixel-wise adaptive (LPA) technique. The LPA method stores the highest unsaturated phase-shifted intensities at each pixel in a set of composite phase-shifted intensity images. Phase-shifted intensities are captured at different linearly varying MIGL that are selected using a specific constant step size in MIGL. By avoiding saturation on a pixel-wise basis, the LPA method improves measurement accuracy when there is a large range of luminance during measurement. A good selection for the size of the steps in MIGL depends on the range of luminance and the amount of saturation in the image.

Dynamic pixel-wise adaptive method

The last method (detailed in Chapter 6) is the dynamic pixel-wise adaptive (DPA) technique. This method also avoids saturation on a pixel-by-pixel basis but dynamically selects the step size in MIGL based on the proportion of the number of saturated pixels from the previous step compared to the initial step. This improves the flexibility in handling measurement of object surfaces with different ranges of luminance. However, this method requires an additional phase-shifted image which adds greater processing time. Therefore, it is much better suited for problems where the range of luminance and amount of saturation will vary greatly between different measurements.

3.4.3 Experimental setup

Surface measurement accuracy with intensity saturation or low SNR has not been explored in the literature prior to the work by Waddington and Kofman [54] who first proposed the adjustment of the MIGL for saturation avoidance using the triangular 2-step pattern. Similar experimental analyses are presented as part of the research in the next chapter. This involves varying the ambient light to determine the trade-off point for the non-adaptive uniform adjustment of MIGL method. Different patterns, pitch, and number of steps are used to see how different parameters affect the error due to saturation and low SNR. This may help in finding the advantages or disadvantages of using a certain pattern, pitch, or number of steps when avoiding saturation. Measurements were performed using the different methods of saturation avoidance on a flat white plate, for a low range of luminance, and a checkerboard, for a large range of luminance.

The measurement system used in all experiments for the different methods of saturation avoidance included: a digital light processing (DLP) projector (In Focus LP600, 8 bit) for computer-generated fringe-pattern projection, a 648×494 pixel grayscale CCD camera (Sony XCHR50, 8 bit) for image capture via a frame-grabber image-processing board (Matrox Odyssey XA), and a computer (P4 3.04 GHz with 1 GB memory). The camera standoff distance was 1.9 m from the reference plane, and the projector-camera angle was approximately 15°.

For measurements with varying ambient light, the light was added by using two additional digital light projectors separate from the measurement system. These projectors were placed approximately 2.9 m from the reference plane to produce approximately uniform lighting across the plate and to minimize changes in lighting with different plate positions. The level of luminance was controlled by projecting uniform gray level patterns varying from 0 to 255. The illuminance of the ambient light projectors was measured with the fringe-pattern projector turned off while using an integrating incident-light meter positioned at the centre of the calibration/reference plate as shown in Figure 3.2.

The minimum input gray level, was set to 40 gray level [58] rather than zero. This was because of the observed nonlinearity shown in Figure 2.6(c) after projector nonlinearity correction for low values of input gray level. This nonlinearity at low input gray level would lead to measurement error.

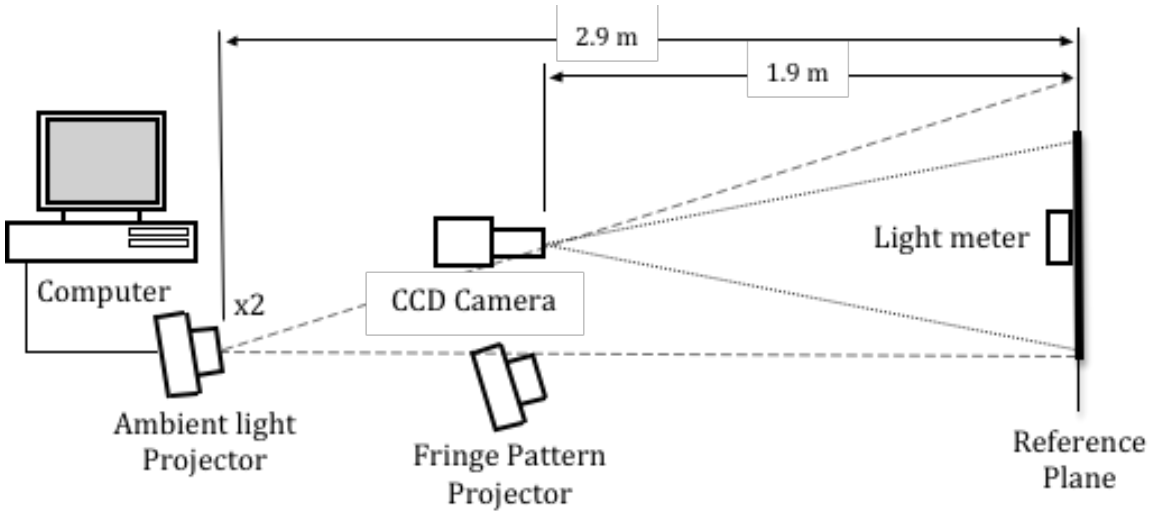

Figure 3.2: Measurement system with ambient light projectors.

Chapter 4

Saturation Avoidance by Reduction of the MIGL

Saturation can be avoided by lowering the MIGL to improve measurement accuracy. However, lowering the MIGL may also cause the intensity modulation to decrease, which can lead to measurement error due to a low SNR. The non-adaptive uniform adjustment of MIGL technique seeks the point that finds the best trade-off between robustness to saturation and low SNR for the highest measurement accuracy when capturing only a single set of phase-shifted images. Once this point is known then subsequent measurements can be performed with a similar range of luminance. The following sections demonstrate this method using real and simulated measurements which are used to analyze the effect of saturation and noise on measurement error at different MIGL. Different pitch, patterns, and number of steps are used to demonstrate that the method works for different fringe patterns and to determine the effect of these parameters on measurement accuracy.

4.1 Experimental method

Two experiments were performed to demonstrate that the newly-developed method of adjusting MIGL can be used to avoid camera sensor saturation and therefore reduce 3D surface measurement error. The experiments were performed to demonstrate how well the technique handles avoidance of camera sensor saturation and low SNR when performing a surface measurement by PSFPP. The first experiment (Section 4.2) determines the measurement accuracy of the system when added ambient light causes camera sensor saturation. The second experiment (Section 4.3) evaluates the measurement errors independently from different sources by simulating the intensity

saturation and noise. This is carried out by altering the captured experimental images to have different levels of added light and noise variance.

Both experiments made use of a dense set of 25 measurements of a flat white plate mounted on a single-axis translation stage. The flat plate was positioned using a digital micrometer from 2 to 50 mm in 2 mm increments as shown in Figure 4.1, for a range of 48 mm. These measurements were performed at 17 different pitches ranging from 4 to 20 pixels, and at 31 different MIGL's from 105 to 255 in steps of 5 for three cases: sinusoidal 3-step and triangular 2 and 3-step, for a total of 39,525 measurements. To perform the measurement and process all of these measurements efficiently, each permutation involving MIGL, pitch, patterns and number of shifts was performed at a given plate position since these parameters can be adjusted quickly by software. When all measurements at the plate position were complete, the plate position was adjusted for the next set of measurements. No digital image filters were used on any of the measurements of the flat white plate to demonstrate the raw error associated with low SNR.

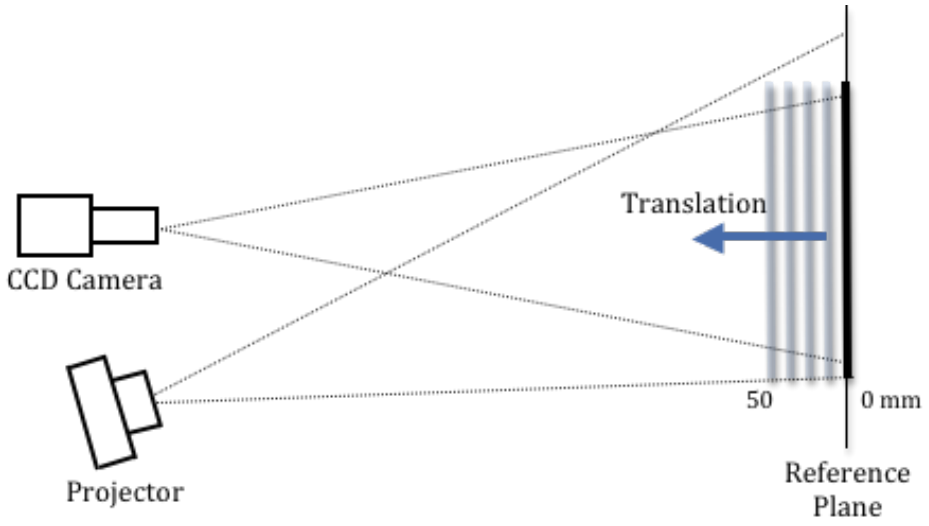

Figure 4.1: Translation of flat white plate with respect to the camera and projector.

Calibrations were performed using the 25 measurement positions for each pitch, pattern and number of shifts at 255 MIGL for a total of 51 calibrations. The calibrations were performed in a dark room with the projection of the fringe pattern as the only source of light to eliminate ambient lighting effects. To attenuate noise in the calibration, all calibrations were filtered using a median filter followed by a mean filter, each with a square window size of 21 pixels.

The reference phase used to compute the phase difference for each measurement had a MIGL of 255 for each pitch and pattern, since this MIGL yields the highest SNR and the value of the MIGL does not affect the computation of the phase. RMSE was computed as the root-mean squared difference between the measured depth and the true depth for all measurement pixels. Measurement pixels include the whole image except for a 10 pixel border around the image where the calibration map was unfiltered.

4.2 Experimental analysis of the effect of added illuminance

4.2.1 Procedure

To compare the effect of saturation due to ambient lighting on the measurement error, the 39,525 measurements described in Section 4.1 were performed with no added ambient light and then with approximately 600 lx of added ambient light using the two additional light projectors as described in Section 3.4.3. The average of the RMSE over depth for the 25 measurements at each pitch, MIGL, pattern and number of shifts were computed for the measurements with no added ambient light and 600 lx of added ambient light.

4.2.2 Results

No added ambient light

With no added ambient light, each of the cases of different patterns and shifts for each pitch shows a general trend of increasing mean RMSE as the MIGL decreases (Figures 4.2 to 4.4). The high RMSE in the region of low MIGL can be attributed to having a low SNR. As the MIGL decreases the mean RMSE is somewhat exponential with the error being approximately constant until a point at which it begins to increase. This trend is more evident for the sinusoidal 3-step method shown in Figure 4.2 which shows a region between MIGL of 205 to 255 and pitch from 4 to 20 pixels with approximately the same RMSE. This trend of having little change in RMSE up to a point is promising for the newly-developed method of lowering the MIGL to avoid saturation.

The RMSE at different pitches shows that having a smaller pitch generally produces a lower RMSE and has a greater robustness to low SNR since the MIGL can

be decreased more before the error dramatically increases. This trend is more clearly shown with the sinusoidal 3-step method in Figure 4.2(b) where the mean RMSE with a 5 pixel pitch at a MIGL of 125 has approximately the same RMSE as having an 18 pixel pitch at a MIGL around 235. However, having a pitch that is too small begins to show a higher error, which is the case for the sinusoidal 3-step method with a pitch less then 5 pixels. This error is likely attributed to the pitch being too small to represent the sinusoidal fringe pattern discretely. The error associated with having a larger pitch can be attributed to having a higher sensitivity to noise since the fringes have a more gradual slope compared to a smaller pitch. The RMSE for the two-step case is noticeably steeper than either of the three-step cases. This is because having more phase-shifts yields less sensitivity to noise since there is more information at each pixel. This helps in the case when one or a few of the phase-shifted intensities is heavily corrupted by noise. Having many phase-shifted intensities allows for the phase to still be computed accurately, while with few phase-shifted intensities, the noise corrupted intensity has a more significant role in the computation. This yields a more incorrect phase.

In Figures 4.2 to 4.4 there is also a periodic decrease in mean RMSE over pitch, which is more noticeable when using the triangular 3-step method. In Figure 4.3 the error is lowest when the pitch is divisible by three, the number of steps for phase shifted images used. This is shown by the sharp valleys of low RMSE in the contour plot. A similar trend was found in [41]. The periodic error can also be seen with the other patterns but it does not necessarily seem to correspond to the pitch being divisible by three or the number of phase-shifts used. The cause of this error is likely due to the fact that the size of the pitch accurately represents the shape of the pattern but exploring this is beyond the scope of this thesis.

Added ambient light

The addition of 600 lx of ambient light caused significant saturation at 255 MIGL, which is the highest intensity quantization level. The extent of the saturation is shown in bar graphs for each pitch (4 to 20 pixels) of the three phase-shifting methods in Figure 4.5. The different shaded stacks show the proportion of the pixels that are saturated in one or two of the phase-shifted images. No pixel was saturated in three phase-shifted images.

These results show that the shape of the pattern can cause more saturation since more pixels will saturate using the sinusoidal pattern than the triangular pattern if saturation occurs. The size of pitch affects the amount of saturation with a smaller pitch having less saturation than a larger pitch. In addition to having a greater

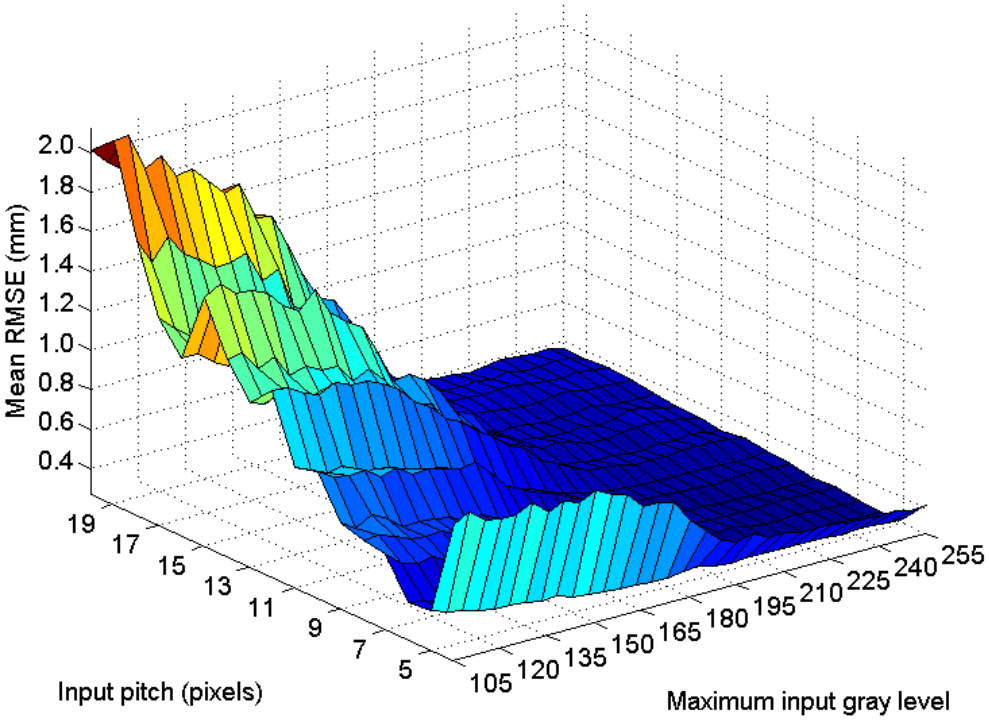

(a)

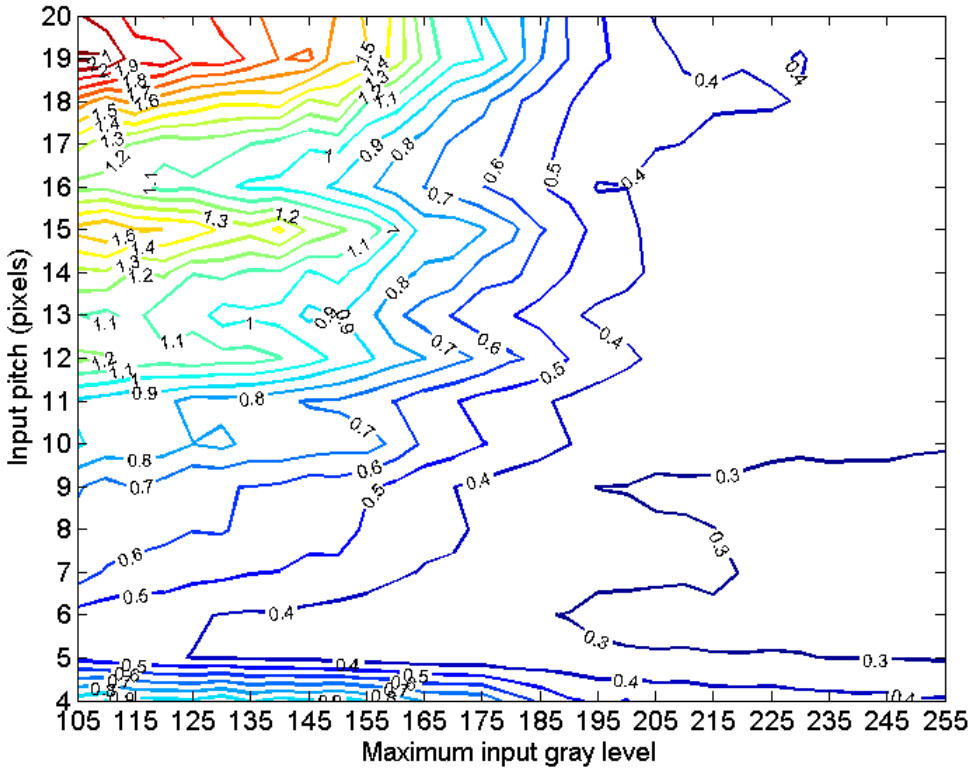

(b)

Figure 4.2: Mean RMSE (mm) over depth with no added ambient light for the sinusoidal 3-step method at different pitches and maximum input gray levels shown as a) surface and b) contours of constant mean RMSE (mm). All errors shown are raw errors without any digital filtering applied.

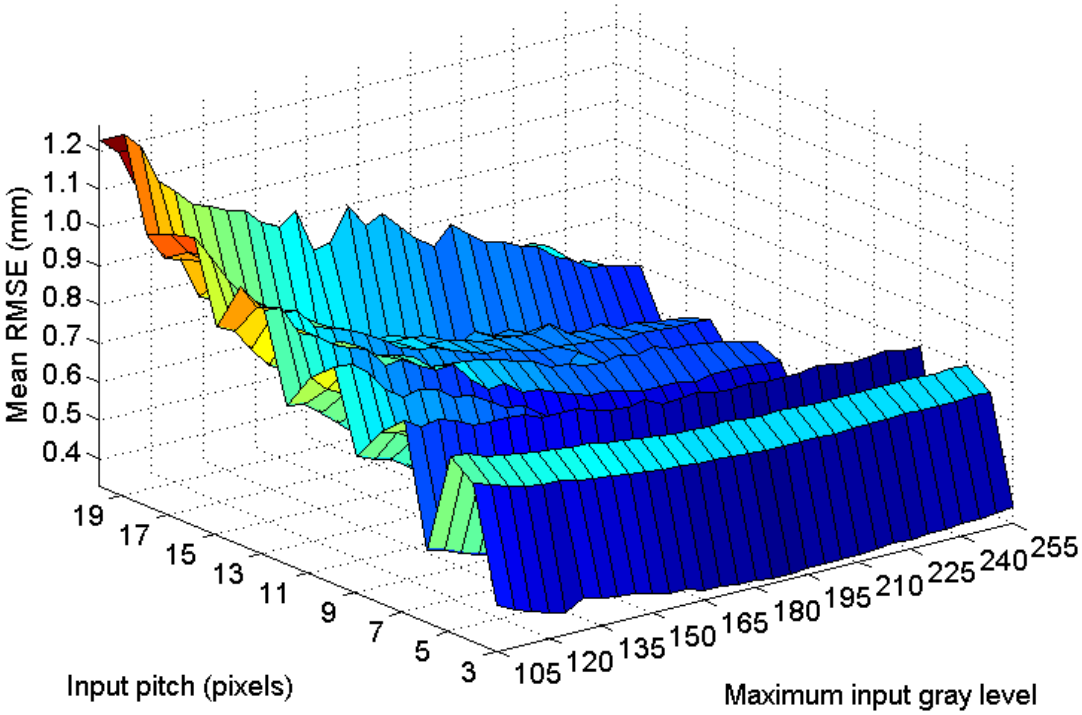

(a)

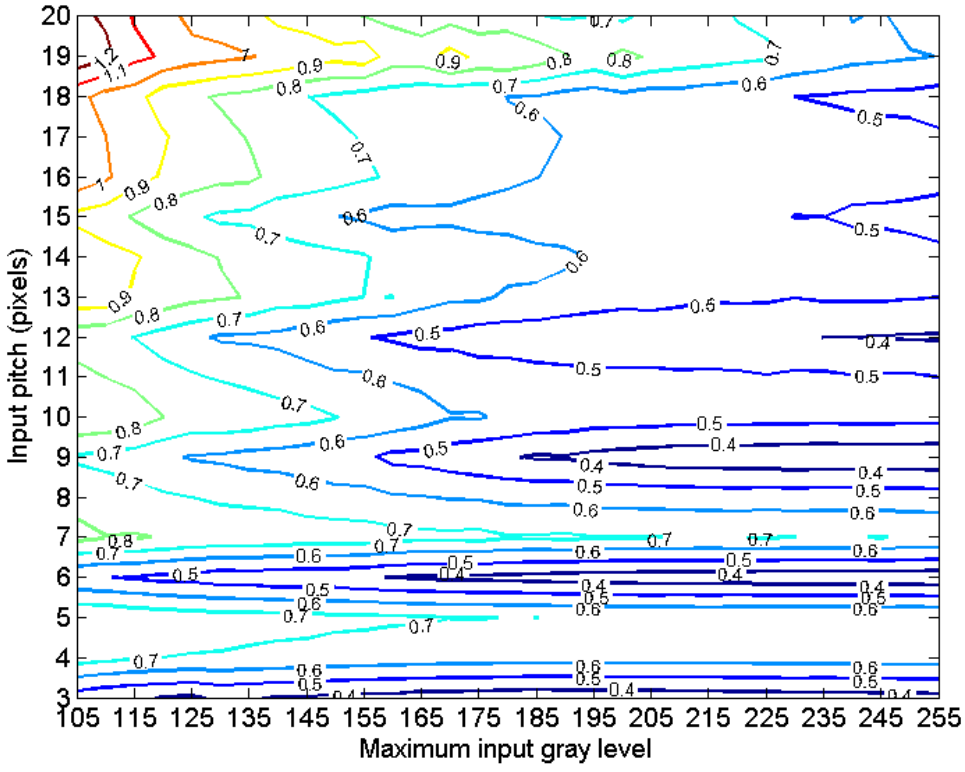

(b)

Figure 4.3: Mean RMSE (mm) over depth with no added ambient light for the triangular 3-step method at different pitches and maximum input gray levels shown as a) surface and b) contours of constant mean RMSE (mm). All errors shown are raw errors without any digital filtering applied.

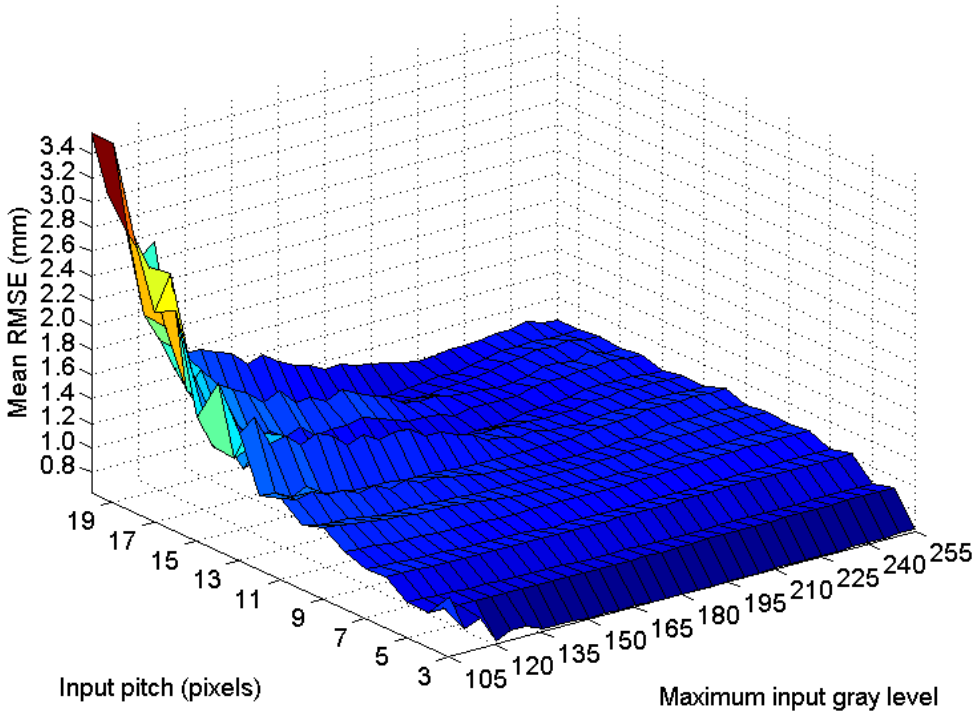

(a)

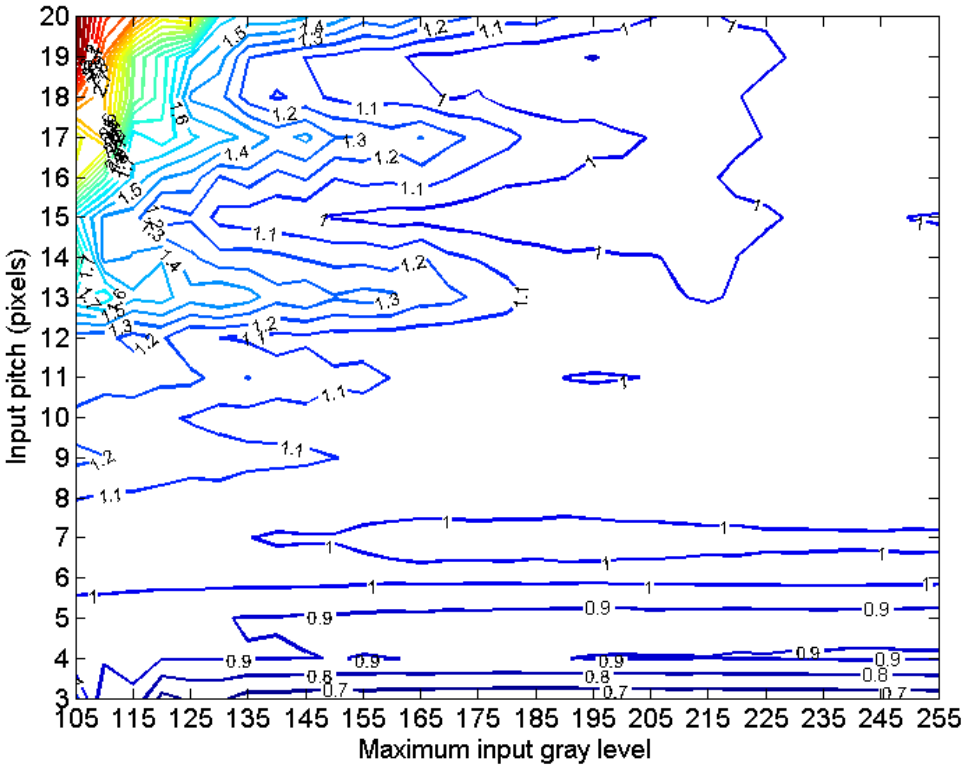

(b)

Figure 4.4: Mean RMSE (mm) over depth with no added ambient light for the triangular 2-step method at different pitches and maximum input gray levels shown as a) surface and b) contours of constant mean RMSE (mm). All errors shown are raw errors without any digital filtering applied.

robustness to low SNR, this result shows that using a smaller pitch has a greater robustness to intensity saturation than using a larger pitch.

The effect of saturation on mean RMSE is characterized by a steep curve with an exponential shape as shown in Figures 4.6 to 4.8 in the region with a high MIGL above 225. The magnitude of the mean RMSE is attributed to the amount of saturation in the phase-shifted images since the sinusoidal pattern has a much larger RMSE due to saturation than either of the triangular patterns. This follows the trends from Figure 4.5. The trend of the RMSE in the low region of MIGL is approximately the same as in Section 4.2.2 with no added light. The combined increase in RMSE attributed to camera sensor saturation in the region with high MIGL and the increase in RMSE attributed to low SNR in the region of low MIGL results in a somewhat parabolic shaped curve with a minimum point for highest accuracy. This result is very useful since the MIGL in this region represents the trade-off between robustness to intensity saturation and low SNR. It also demonstrates that the accuracy can be improved by lowering the MIGL in the presence of intensity saturation.

Corresponding surface (top row) and contour (bottom row) plots of the RMSE at 255 MIGL (left column) and at 225 MIGL (right column) are shown in Figure 4.9 to 4.11, for the sinusoidal 3-step, and the triangular 3 and 2 step, respectively. These plots show the gain in accuracy and trend for each individual measurement by lowering the MIGL when there is saturation compared to the conventional measurements at 255 MIGL. Valleys of RMSE using the triangular 2-step method occur as a function of pitch and depth.

To more easily compare the accuracies using different patterns at these two different MIGL and to recognize the advantage of lowering the MIGL for saturation avoidance, graphs using the average RMSE over depth from Figures 4.9 to 4.11 are shown in Figure 4.12. Note that all errors shown are raw errors without any digital filtering applied. It is clear that measurement errors at 255 MIGL (Figure 4.12(a)) are greater than those at 225 MIGL for each pitch (Figure 4.12(b)). At 255 MIGL, (Figure 4.12(a)) the accuracy increases (error decreases) as the pitch decreases, especially for the sinusoidal 3-step pattern, which has a mean RMSE of 0.46 mm at a pitch of 4 pixels, compared to a mean RMSE of 3.28 mm at a pitch of 20 pixels. This gain in accuracy as the pitch decreases is partly due to the lower number of pixels that are saturated and the shape of the projected pattern as shown by the results in Figure 4.5. The greater number of saturated pixels using the three-step methods as opposed to the two-step method is why there is a greater difference in error between the measurements at 225 MIGL and the measurements at 255 MIGL with the same amount of added light. This shows that it is increasingly important to have a saturation avoidance technique when using more phase-shifts, a larger pitch, and/or the sinusoidal pattern.

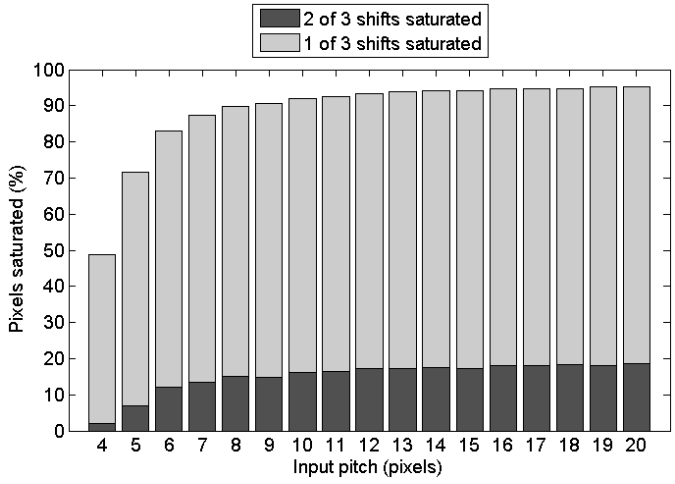

(a)

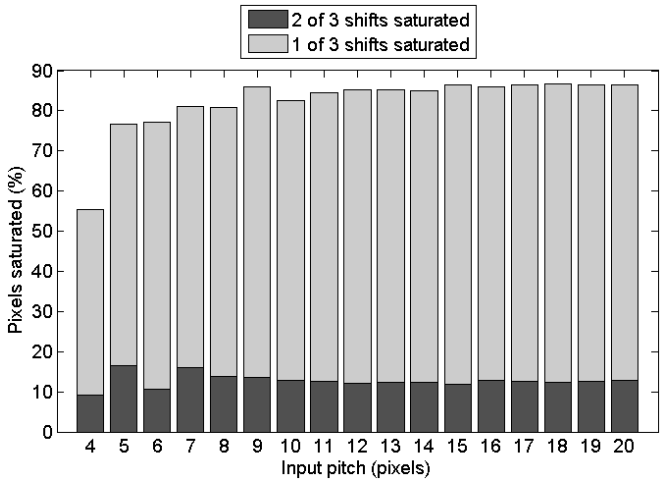

(b)

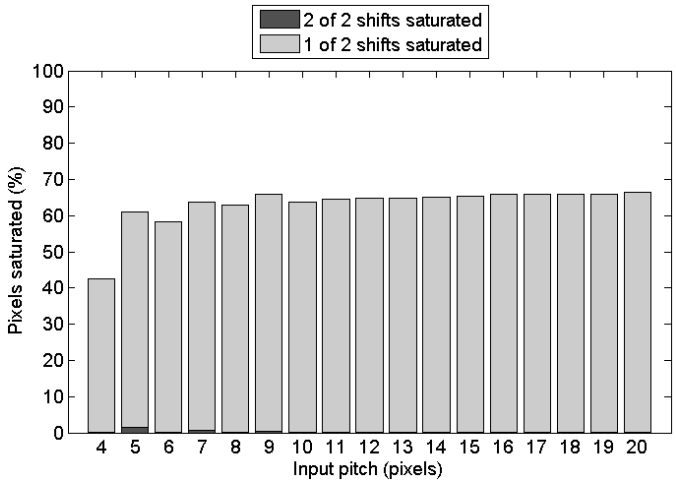

(c)

Figure 4.5: Percent of pixels saturated for each fringe pattern pitch ranging from 4 to 20 pixels with a MIGL of 255. The percentage of pixels are grouped by the number of phase-shifts that are saturated and shown for the a) sinusoidal 3-step, b) triangular 3-step, and c) triangular 2-step methods.

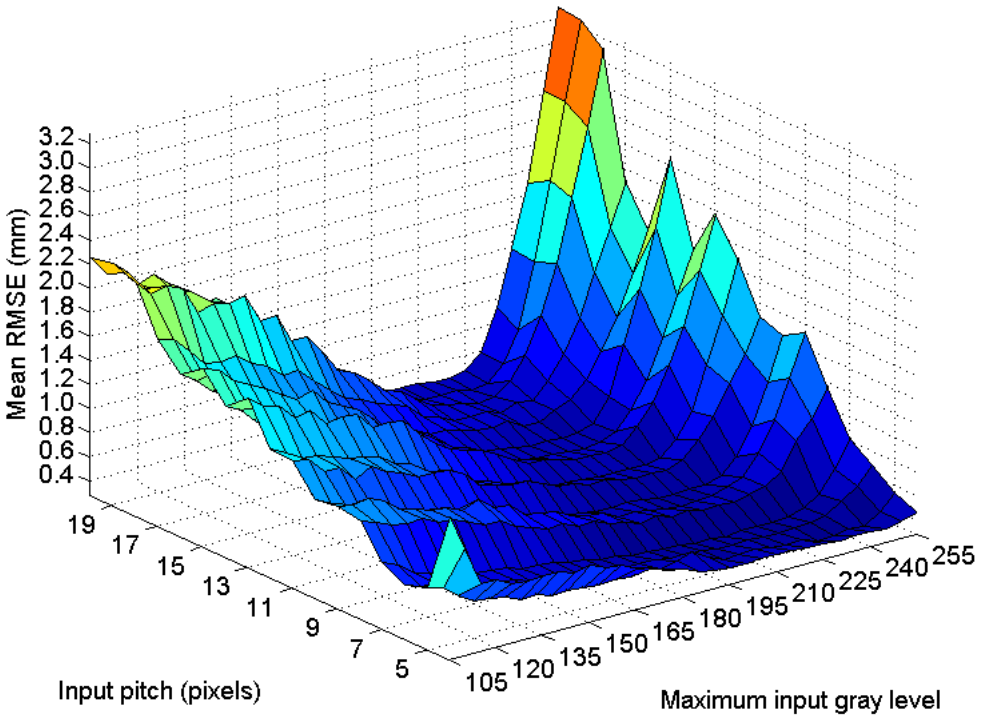

(a)

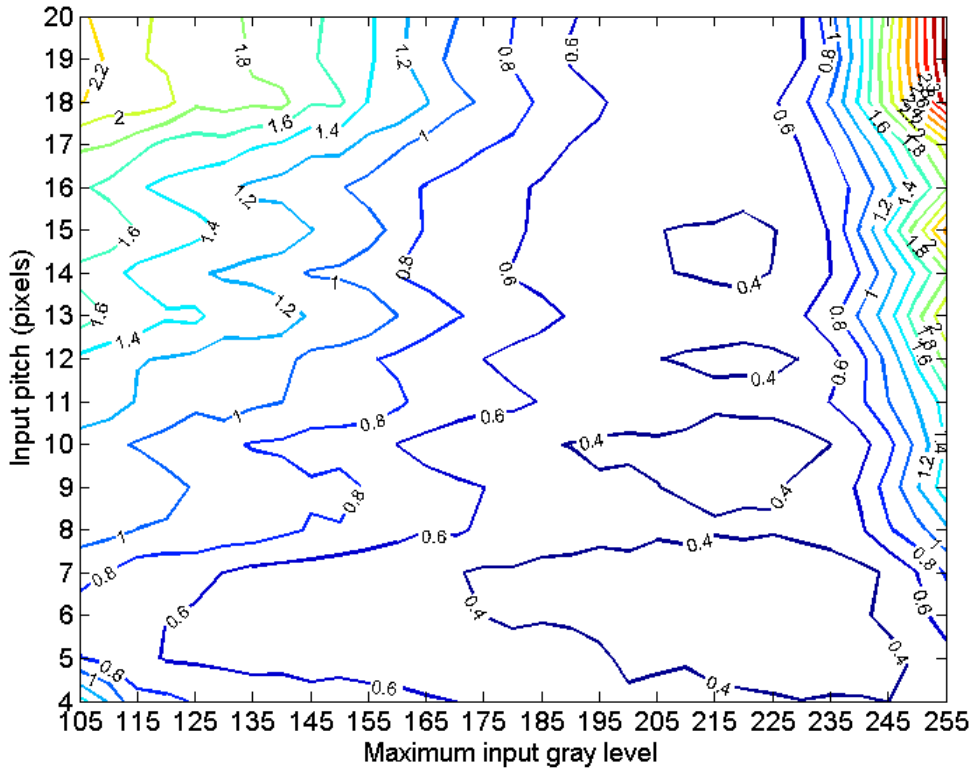

(b)

Figure 4.6: Mean RMSE (mm) over depth with 600 lx of added ambient light for the sinusoidal 3-step method at different pitches and maximum input gray levels shown as a) surface and b) with contours of constant mean RMSE (mm). All errors shown are raw errors without any digital filtering applied.

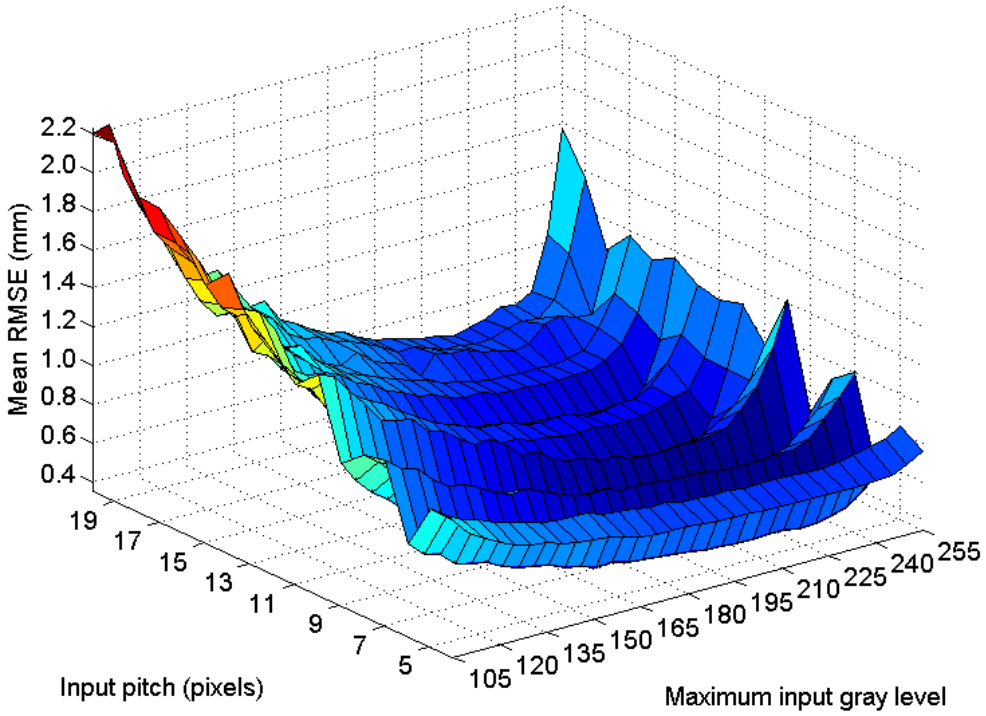

(a)

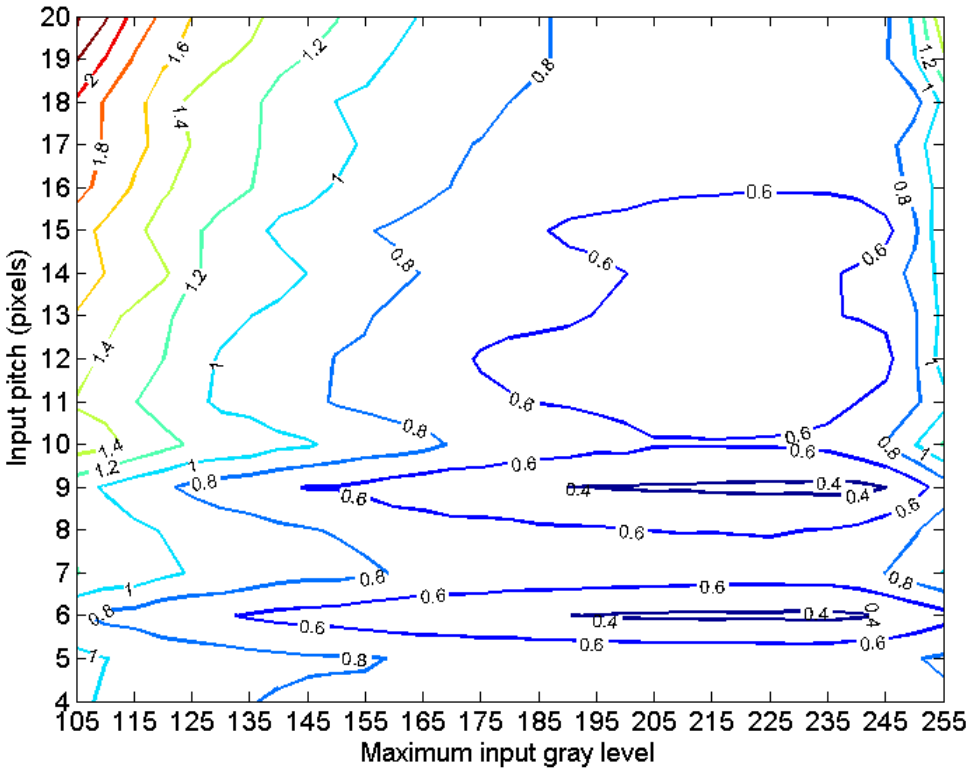

(b)

Figure 4.7: Mean RMSE (mm) over depth with 600 lx of added ambient light for the triangular 3-step method at different pitches and maximum input gray levels shown as a) surface and b) with contours of constant mean RMSE (mm). All errors shown are raw errors without any digital filtering applied.

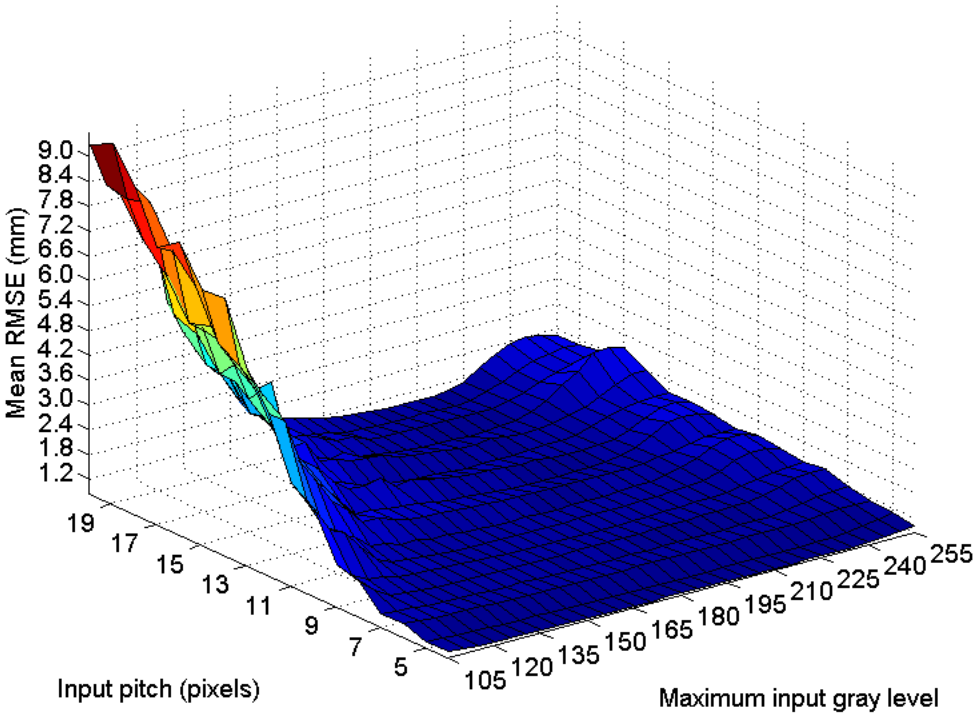

(a)

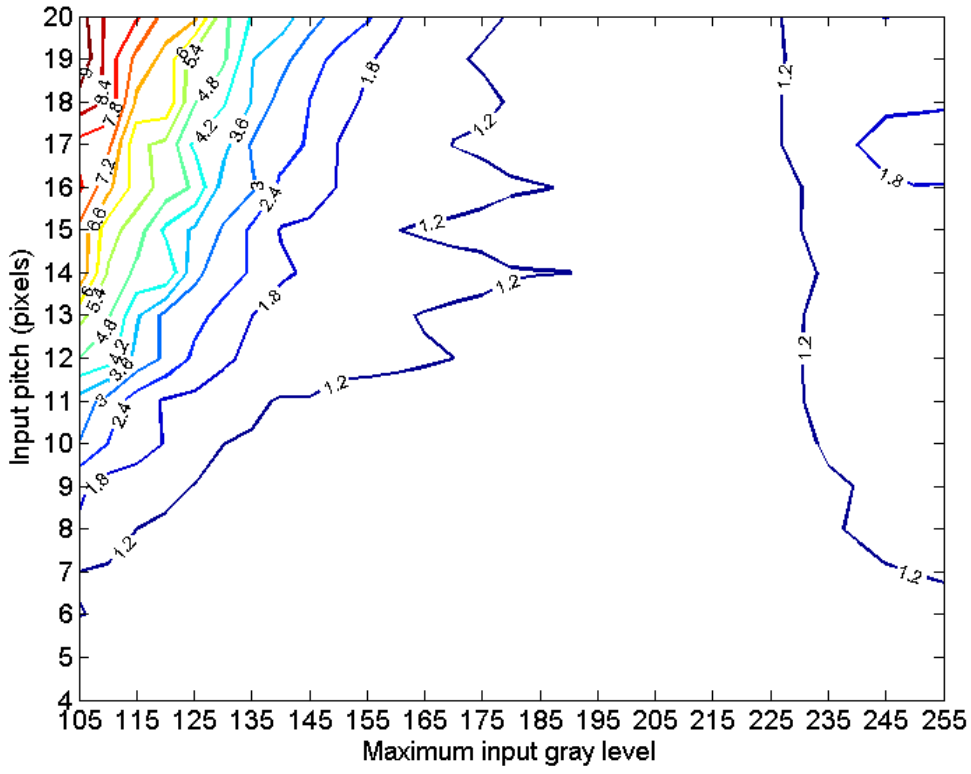

(b)

Figure 4.8: Mean RMSE (mm) over depth with 600 lx of added ambient light for the triangular 2-step method at different pitches and maximum input gray levels shown as a) surface and b) with contours of constant mean RMSE (mm). All errors shown are raw errors without any digital filtering applied.

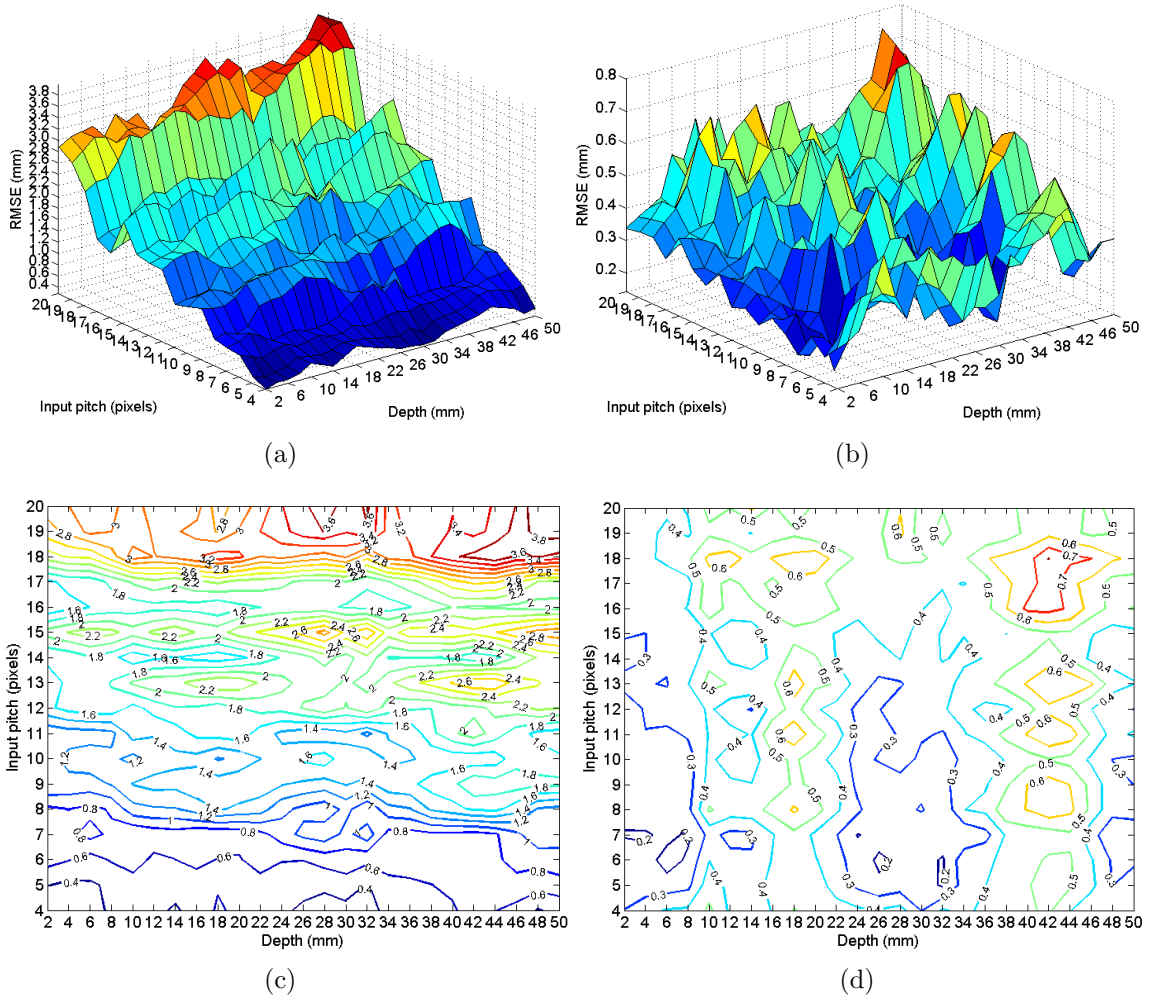

Figure 4.9: Surface and contour plots of the RMSE over the image with 600 lx of added ambient light for measurements using the sinusoidal 3-step method with different pitches ranging from 4 to 20 at 25 measurement positions spaced 2 mm apart. The left column (Figures (a) and (c)) shows measurements at 255 MIGL while the right column (Figures (b) and (d)) shows measurement at 225 MIGL. In the top row (Figures (a) and (b)) are the surface plots and (Figures (c) and (d)) are contour plots with contours of constant RMSE (mm). All errors shown are raw errors without any digital filtering applied.

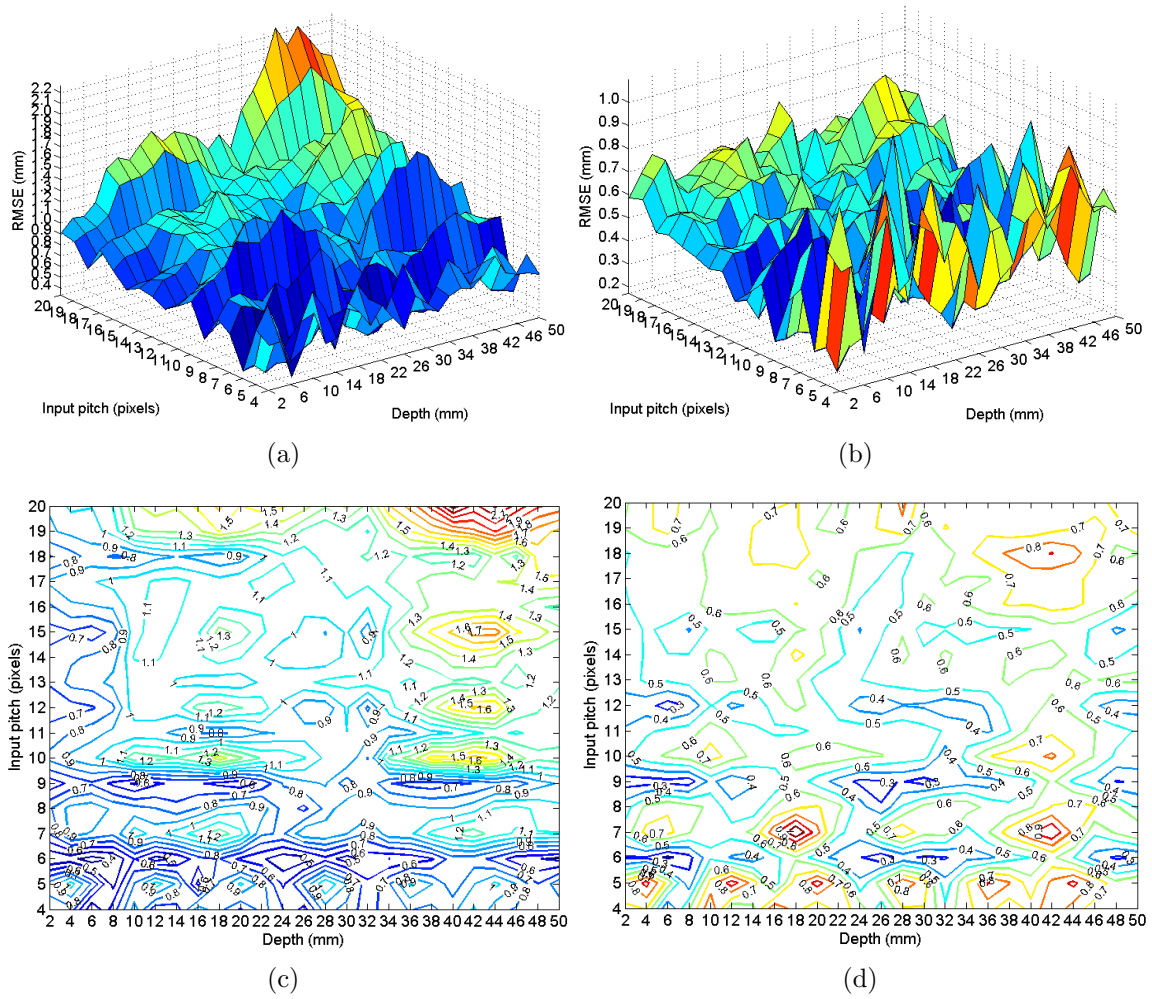

Figure 4.10: Surface and contour plots of the RMSE over the image with 600 lx of added ambient light for measurements using the triangular 3-step method with different pitches ranging from 4 to 20 at 25 measurement positions spaced 2 mm apart. The left column (Figures (a) and (c)) shows measurements at 255 MIGL while the right column (Figures (b) and (d)) shows measurement at 225 MIGL. In the top row (Figures (a) and (b)) are the surface plots and (Figures (c) and (d)) are contour plots with contours of constant RMSE (mm). All errors shown are raw errors without any digital filtering applied.

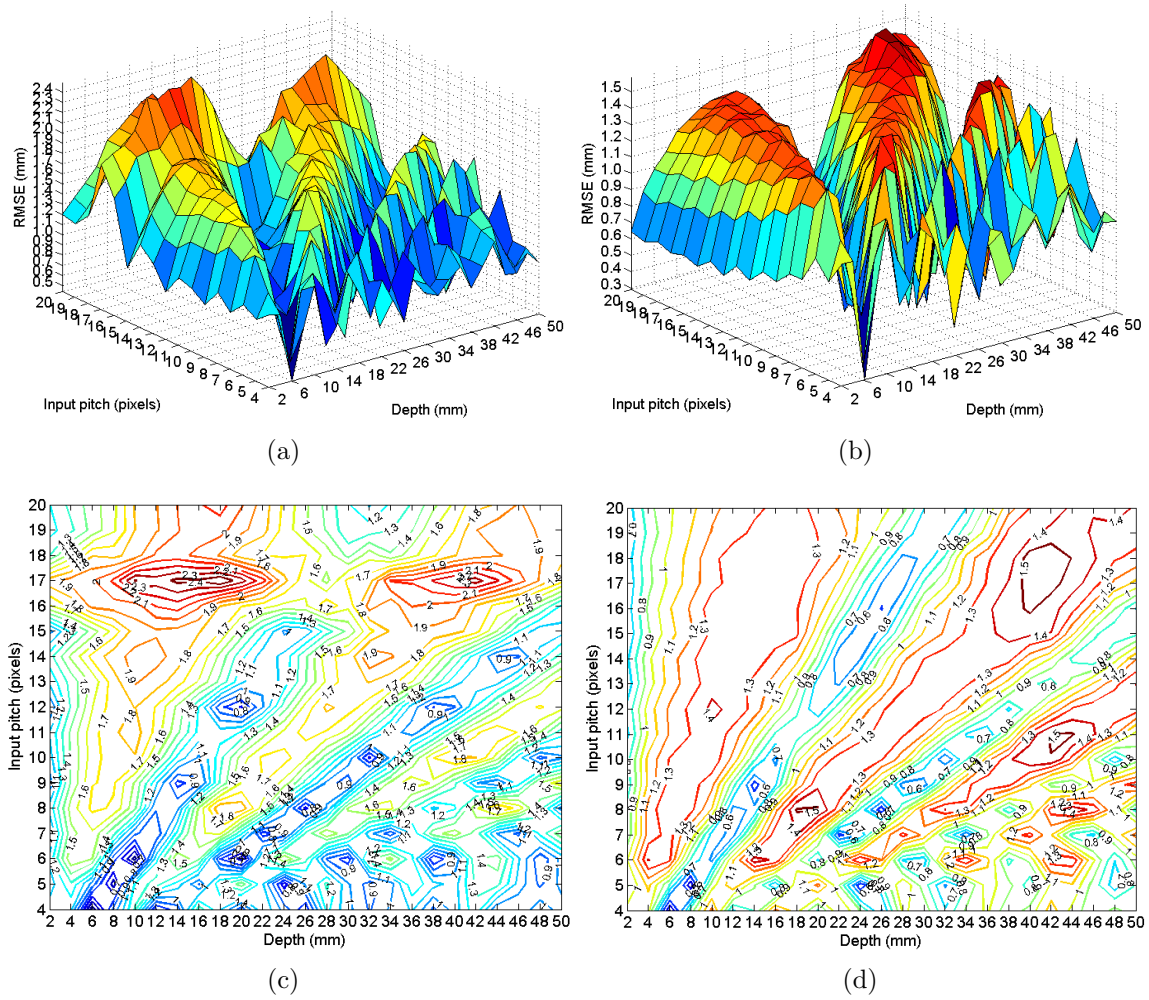

Figure 4.11: Surface and contour plots of the RMSE over the image with 600 lx of added ambient light for measurements using the triangular 2-step method with different pitches ranging from 4 to 20 at 25 measurement positions spaced 2 mm apart. The left column (Figures (a) and (c)) shows measurements at 255 MIGL while the right column (Figures (b) and (d)) shows measurement at 225 MIGL. In the top row (Figures (a) and (b)) are the surface plots and (Figures (c) and (d)) are contour plots with contours of constant RMSE (mm). All errors shown are raw errors without any digital filtering applied.

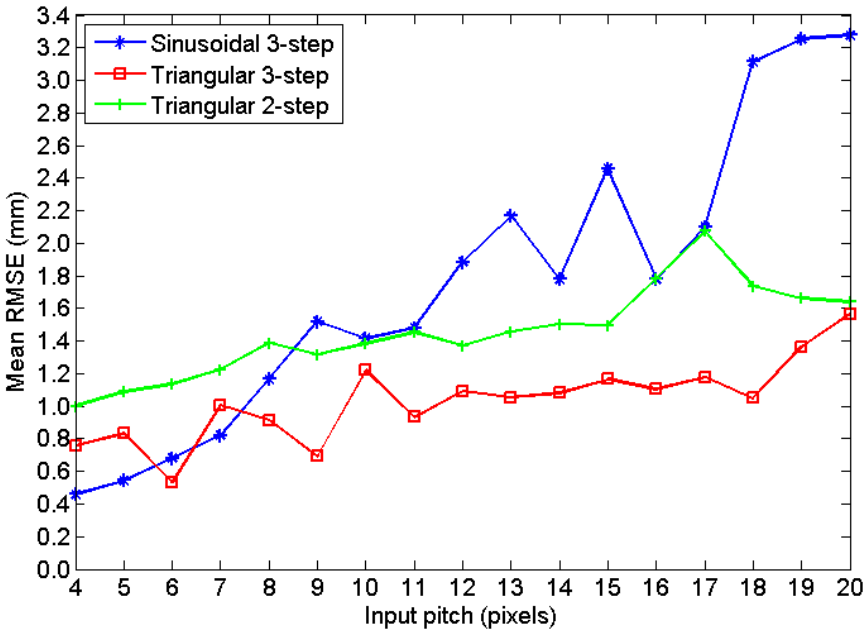

(a)

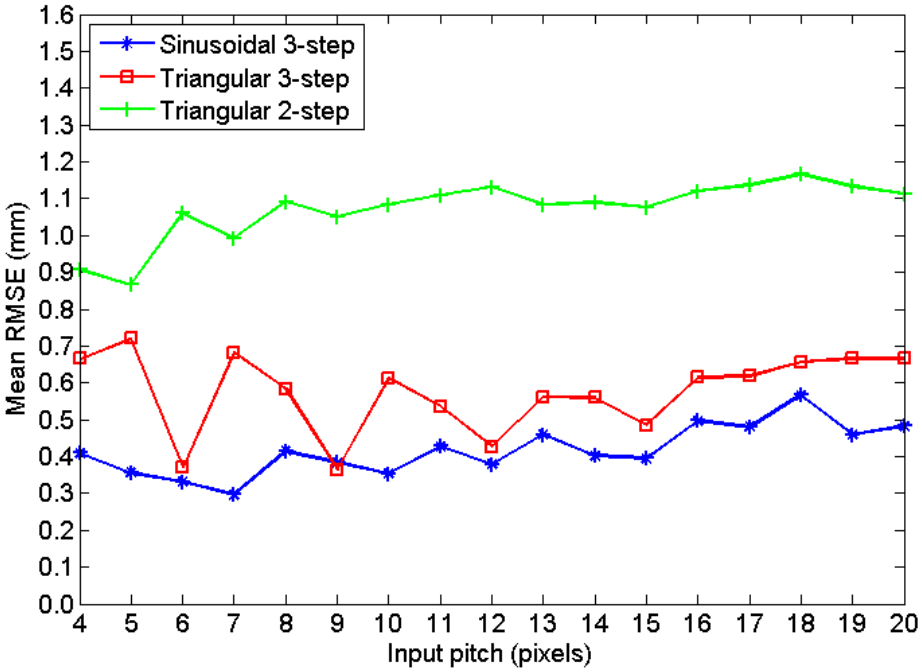

(b)

Figure 4.12: Comparison of the mean RMSE over depth and over the entire surface for measurements with 600 lx of added illuminance for different fringe patterns and number of phase-shifts with different pitches ranging from 4 to 20. (a) Errors at 255 MIGL, and (b) errors at 225 MIGL. are shown in (b). All errors shown are raw errors without any digital filtering applied.

4.2.3 Analysis of results

A pitch of 6 pixels was chosen for more detailed analysis since it gave the lowest mean RMSE in the sinusoidal case and has good results in both the two and three step triangular cases. The results from Figures 4.2 to 4.8 at a pitch of 6 pixels with both the 0 lx and 600 lx data shown in the same figure for each of the three cases (Figure 4.13). The general trends of RMSE are very similar for all three cases. When there is no added light (0 lx) the mean RMSE decreases steadily as the MIGL increases. When 600 lx of ambient light is added, the lowering of the MIGL from 255 seems to help in avoiding saturation and this results in a lower measurement error. However, as the MIGL is lowered below the trade-off point, the error increases when lowering the MIGL. This is due to the lower SNR at low MIGL. The greater steepness for the 600 lx compared to the 0 lx on the left side of the curves, and the overall offset in mean RMSE for the 600 lx curves from the 0 lx curve is likely due to the added noise of the 600 lx of added light. To show that the error offset is likely caused by added noise from the light source and to analyze the effects of noise and saturation on RMSE independently, simulations were performed as described in the following section.

4.3 Simulation of added illuminance

The results from Section 4.2 showed that, in the presence high luminance that causes camera sensor saturation, lowering the MIGL yields an improved accuracy up to a point when the SNR is too low and a higher measurement error occurs. This results in a somewhat parabolic shaped curve with a minimum point. This section further explores the errors at MIGL below and above the trade-off point seen in Figure 4.13 using two simulations. By simulating the effects of ambient light on accuracy the cause of error in the regions of low and high MIGL can be explored independently at a wider range of values than can easily be obtained in the laboratory by real measurements. The first simulation explores the effect of saturation on the mean RMSE in the region of high MIGL by simulating added ambient light. The second simulation explores the effect on low SNR on the mean RMSE in the region of low MIGL by simulating added ambient noise from the light source.

4.3.1 Procedure

The simulations were performed by modifying the real images acquired previously with no added light (Section 4.2) with a pitch of 6 pixels for each of the MIGLs,

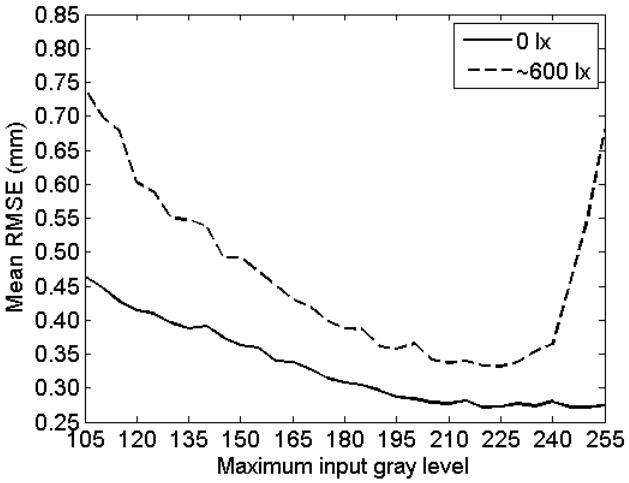

(a)

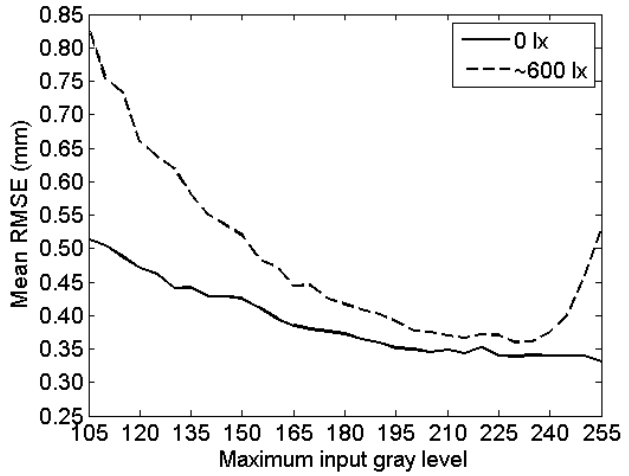

(b)

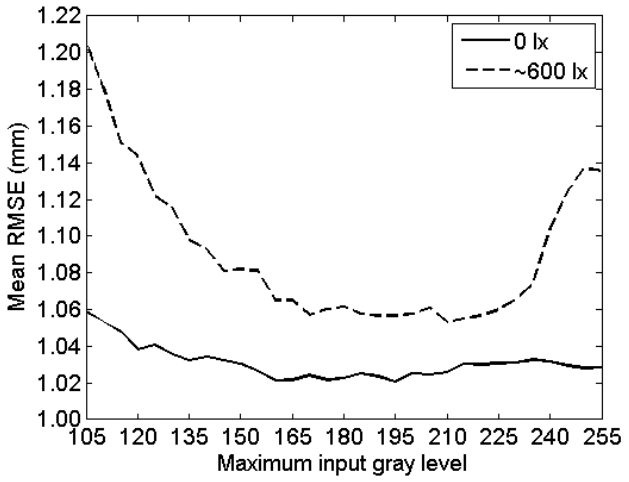

(c)

Figure 4.13: Comparison of RMSE between 0 lx and 600 lx of added ambient light with a pitch of 6 pixels for a) sinusoidal 3-step, b) triangular 3-step, and c) triangular 2-step methods. All errors shown are raw errors without any digital filtering applied.

patterns, shifts, and the 25 measurement positions. The modified images were created by adding intensity distributions $D(x, y)$ while saturating the modified image if the calculated intensity exceeded the maximum quantization level according to Equation 4.1.

$$I_i^*(x, y) = \min\left[2^B - 1, I_i(x, y) + D(x, y)\right], \quad i = 1, 2, 3 \quad M = 8 \tag{4.1}$$

where $I_i^*(x, y)$ is the modified image of the ith phase shift from the original captured image and B is the bit-depth of the camera. The PSFPP measurement method was performed on each set of modified phase-shifted images by calculating the phase difference map, $\Delta\phi(x, y)$, and computing the height using the phase-to-height map determined by prior calibration. The following subsections describe the distribution used for $D(x, y)$ and how it was determined.

Simulated added ambient light

For the first simulation, the distribution, $D(x, y)$, was uniform with a gray level that corresponded to the specified amount of added ambient light. To determine the value of this gray level, the relationship between the camera captured gray level and the object luminance of the white plate had to be determined. This relationship was found in three steps. First, the relationship between the gray level inputs to the projector and the camera captured intensities was determined by projecting known uniform gray level patterns onto the white plate, capturing images, and averaging the intensities (Fig. 4.14(a)). The second step was to determine the relationship between the gray level inputs to the projector and the object luminance of the white plate. This was achieved using an incident-light meter with an integrating hemispherical sensor located at the center of the reference plane for each of the different uniform gray level patterns projected (Fig. 4.14(b)). The final relationship between the camera captured gray levels and luminance can be determined from the first two relationships, the camera-captured intensity to input gray level (Fig. 4.14(a)) and input gray level to luminance (Fig. 4.14(b)).

The result is the approximately linear plot shown in Figure 4.14(c). Note that this result was found without using projector nonlinearity correction, which is evident by the nonlinearity in Figures 4.14(a-b). However, the same result could still be obtained when using the projector nonlinearity correction since the effect of the nonlinearity would cancel out to determine the relationship in Figure 4.14(c). The nearly linear relationship in Figure 4.14(c) shows that the nonlinearity of the mapping between the projector and the camera is mainly due to the projector and not the camera. The resulting relationship in Figure 4.14(c) is used to determine the amount to increase

the gray level for a given amount of added light for the simulation. It can also be used to approximate the amount of luminance that can be added before the camera sensor would begin to saturate. For the current experimental setup, the slope in Figure 4.14(c) was approximately 0.17 intensity gray level/lx.

Using the relationship in Figure 4.14(c), modified images were created with added ambient light ranging from 100 lx to 900 lx in increments of 100 lx.

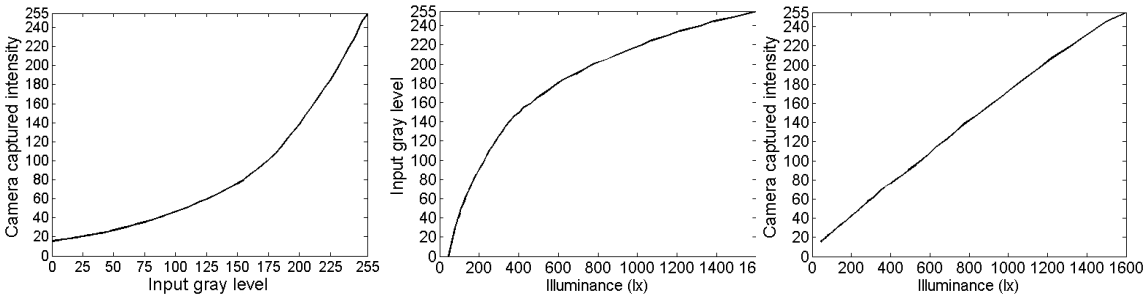

(a) (b) (c)

Figure 4.14: Relationship between captured intensity and luminance. a) Projector nonlinearity b) Conversion between projected intensities and luminance c) Camera intensities versus luminance.

Simulated ambient intensity noise

In the second simulation the distribution $D(x, y)$, had 600 lx of added uniform ambient light, as described in the previous subsection, with additive zero-mean Gaussian intensity noise with standard deviation, σ, from 1 to 8 gray level. The assumption that the noise is distributed as a zero-mean Gaussian is also made by Li et al. [52] who use a sinusoidal fringe pattern for surface-depth measurement.

4.3.2 Results

The results of the simulations of added ambient light and added noise are discussed in the following subsections. All errors shown are raw errors without any digital filtering applied.

Simulated added ambient light

The measurement simulations from 100 lx to 900 lx all had the same mean RMSE for MIGL from 105 to the trade-off points, 190, 195, and 185 for the sinusoidal 3-step,

triangular 3-step, and triangular 2-step patterns (Fig. 4.15), respectively. Above these MIGL values (190, 195, and 185) saturation begins to occur and the mean RMSE begins to deviate from the 100 lx curve with increasing error as the MIGL increases for each of the cases (100 lx to 900 lx) of simulated added ambient light. Below the trade-off points, RMSE also increases due to decreasing SNR with lower MIGL for all cases (100 lx to 900 lx) but at the same rate. The curves with the highest RMSE at high MIGL occur for 900 lx and continue in descending order to 100 lx, where little to no saturation occurs. The results of the simulation show that lowering the MIGL to the trade-off point when there is intensity saturation reduces the measurement error dramatically. This is shown in Table 4.1 where RMSE at 255 MIGL is compared to RMSE at the trade-off point using the sinusoidal 3-step method with a 6 pixel pitch. The RMSE at the trade-off MIGL with different levels of added ambient light are approximately 0.3 mm compared to 0.56 mm at 500 lx and 373.42 at 900 lx. The trade-off MIGL also shifts to a slightly lower MIGL as the ambient light increases with a trade-off MIGL of 225 at 500 lx and 190 MIGL at 900 lx.

Table 4.1: Reduction of Mean RMSE by Lowering the MIGL for the Sinusoidal 3-step Method with a 6 Pixel Pitch Determined by Simulation

Ambient light (lx)	Trade-off MIGL	255 MIGL Mean RMSE (mm)	Trade-off MIGL Mean RMSE (mm)
500	225	0.56	0.31
600	215	0.86	0.31
700	210	1.21	0.32
800	190	85.05	0.32
900	190	373.42	0.32

Simulated ambient intensity noise

The results of measurement simulations with added noise are shown in Fig. 4.16. In this simulation, noise affects the measurement accuracy for all MIGL values, however it becomes increasingly worse as the SNR decreases with either decreasing MIGL or increasing noise variance, or both, as seen by the increasing distance between curves of different noise standard deviation as the MIGL decreases. Because of the presence of saturation from the 600 lx of added simulated light, there exists a trade-off point between robustness to saturation and low SNR. Above the trade-off point, noise has a negligible effect and saturation is the dominant source of error. For the 3-step cases

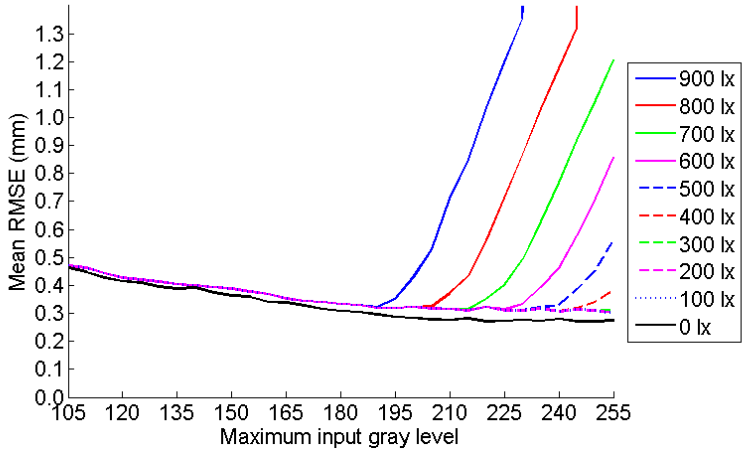

(a)

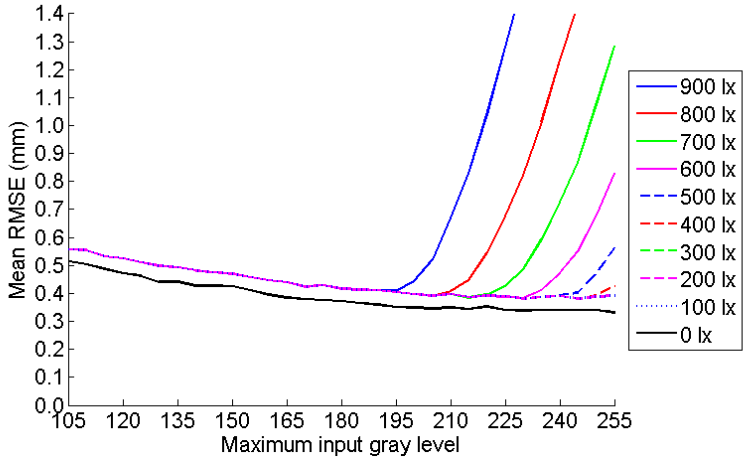

(b)

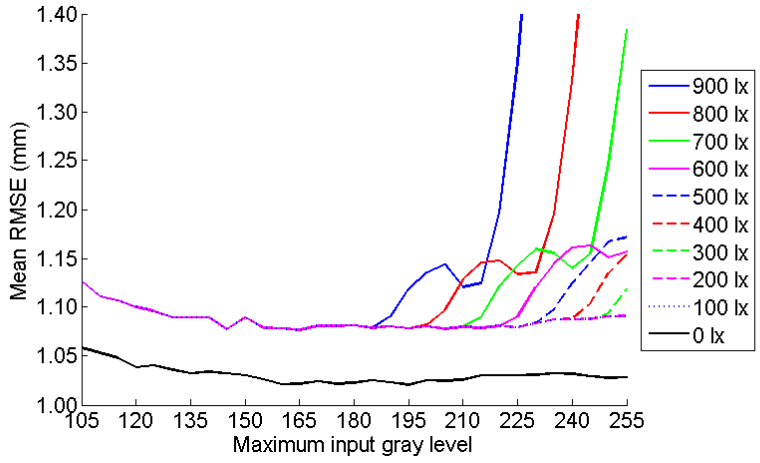

(c)

Figure 4.15: Mean RMSE (mm) for simulations of varying added ambient light with a pitch of 6 pixels for the a) sinusoidal 3-step, b) triangular 3-step, and c) triangular 2-step methods. All errors shown are raw errors without any digital filtering applied.

(Fig. 4.16(a-b)) this trade-off is at approximately the same MIGL (225-230 for the sinusoidal pattern and 230-235 for the triangular pattern) for the different levels of noise standard deviation. As the noise variance increases the MIGL trade-off shifts to a slightly higher MIGL. This is shown in Table 4.2 where the trade-off point is at 225 MIGL with a standard deviation of one gray level and at 230 MIGL with a standard deviation of eight gray level. The shift to a higher trade-off MIGL shows that it may be advantageous (in the RMSE sense) to tolerate some saturation in the image rather than have regions with low SNR. The RMSE at the trade-off MIGL using the sinusoidal 3-step method with a 6 pixel pitch for different noise standard deviations is also shown in Table 4.2. The results from the table show that as the noise standard deviation increases from one gray level to eight gray level that the RMSE gradually increases from 0.32 mm to 0.58 mm.

Table 4.2: Mean RMSE at the Trade-off MIGL in Measuring a Flat White Plate with 600 lx of Added Ambient Light and Intensity Noise using the Sinusoidal 3-step Method with a 6 Pixel Pitch

σ	Trade-off MIGL	Mean RMSE(mm) at the Trade-off MIGL
1	225	0.32
2	225	0.34
3	225	0.37
4	225	0.40
5	225	0.45
6	230	0.49
7	230	0.53
8	230	0.58

4.4 Measurement and simulation results and discussion

The results of the real measurement with added ambient light of 600 lx from Section 4.2 and results of the measurement simulation at 600 lx with noise, $\sigma = 1$, which matched most closely to the real measurement, are shown in Figure 4.17. The real measurement verifies the simulation, showing the lower measurement error with reduced MIGL above the trade-off point of MIGL and higher measurement error below

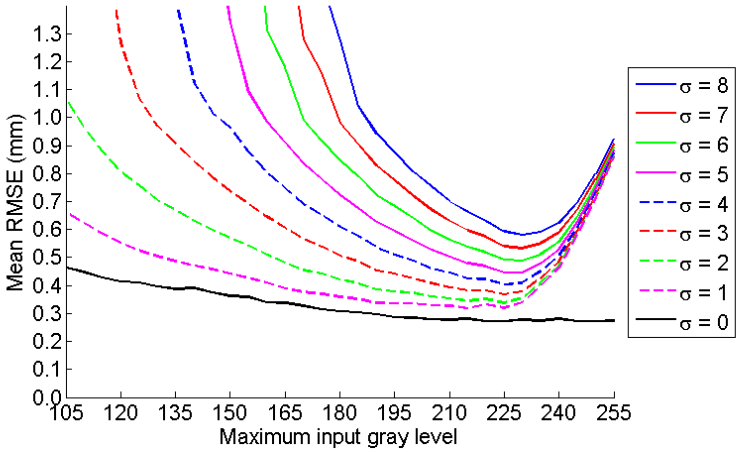

(a)

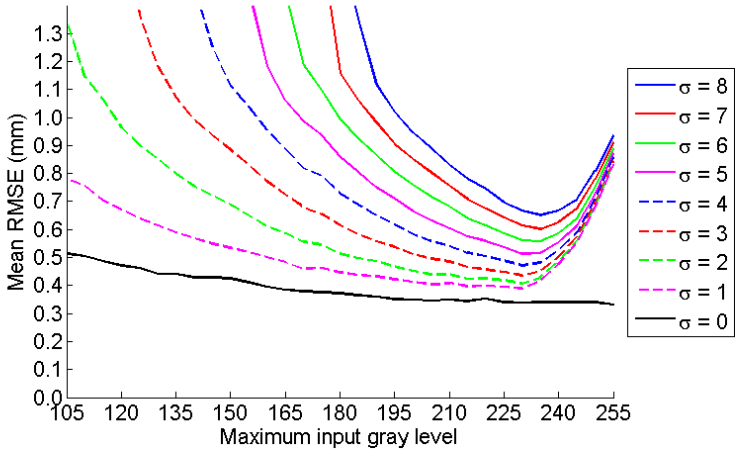

(b)

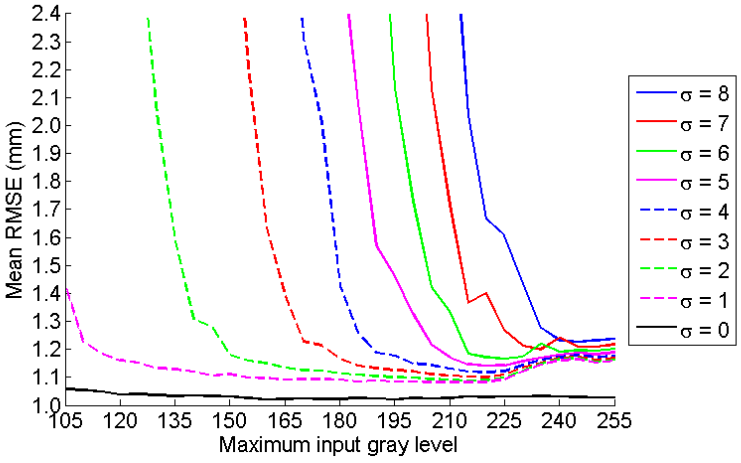

(c)

Figure 4.16: Measurement simulation of added zero-mean Gaussian noise with different gray level noise standard deviations at a pitch of 6 pixels and simulated 600 lx of added light for the a) sinusoidal 3-step, b) triangular 3-step, and c) triangular 2-step methods.

Table 4.3: Comparison Between Real Measurements at the Trade-off MIGL and at 255 MIGL for Different Fringe Patterns

Pattern	Trade-off MIGL	RMSE at 255 MIGL		RMSE at trade-off
		0 lx (mm)	600 lx (mm)	600 lx (mm)
Sinusoidal 3-step	225	0.27	0.68	0.33
Triangular 3-step	230	0.33	0.53	0.36
Triangular 2-step	215	1.03	1.35	1.05

the trade-off point where measurement is sensitive to noise. The measurement at 600 lx also verifies that reducing the MIGL can achieve approximately the same minimum error in the presence of added light as that obtained with no ambient light (0 lx) and MIGL 255. This demonstrates the effectiveness and advantage of the newly-developed MIGL adjustment method for avoiding saturation and improving measurement accuracy. The results at the 255 and trade-off MIGL for the real measurements with a 6 pixel pitch are shown in Table 4.3. This table shows that the raw RMSE without any digital filtering applied at the trade-off MIGL with 600 lx of added light is comparable, although slightly higher, than the RMSE with no added light. There is an evident gain in accuracy by lowering the MIGL to avoid saturation when comparing the RMSE at the trade-off MIGL to 255 MIGL with 600 lx of added light for each of the different patterns and number of shifts.

The results from Figure 4.17 show that reducing the MIGL will lower the measurement error by removing saturation. This MIGL reduction should ideally be carried out until the trade-off point, where image intensity sensitivity to noise will begin to diminish the advantage of further MIGL reduction. MIGL reduction to the trade-off point will provide some tolerance in allowing additional ambient light without saturation or increase in error.

The effectiveness of the method of saturation avoidance is demonstrated in Figure 4.18 by surface measurements of a white plastic mask using the sinusoidal 3-step method with a pitch of 6 pixels for select MIGL values of 105, below the trade-off point; 225, the trade-off point; and 255 with no MIGL reduction applied (across figure columns). The top and bottom rows have no ambient light (0 lx) and 600 lx ambient light, respectively. The measured mask surfaces reflect the results shown in Figures 4.2. With no added ambient light (0 lx), a smoother surface is seen when the MIGL is higher and therefore the range of gray levels and intensity SNR is higher. The best result occurred at 255 MIGL (top right corner) with the smoothest surface, however there was only a marginal difference when using a slightly lower MIGL at 225 (top row, middle column) despite having a lower intensity modulation. When the MIGL was

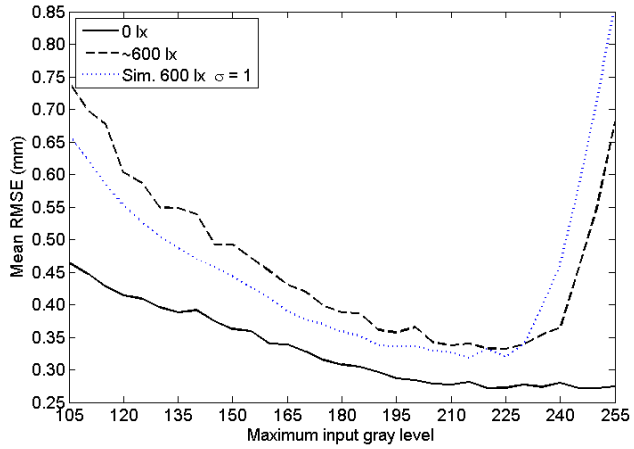

(a)

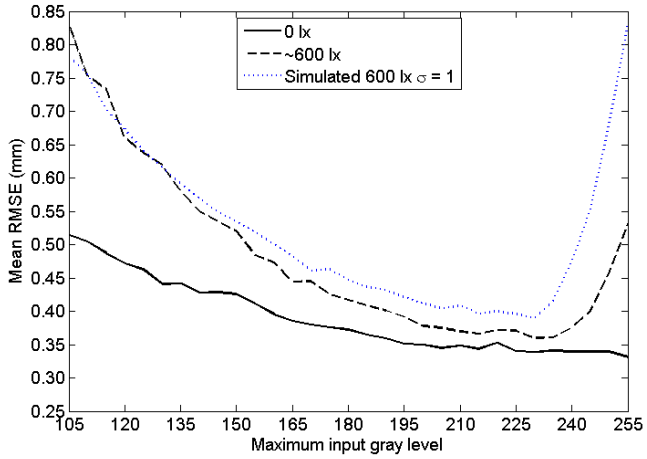

(b)

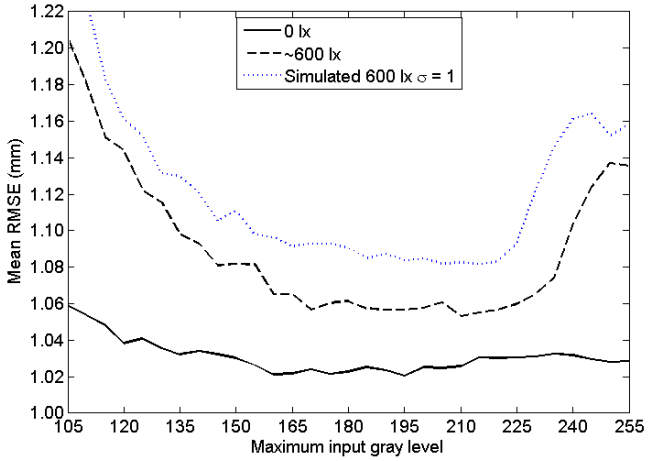

(c)

Figure 4.17: Comparison between experimental measurements with 0 lx, and 600 lx added light along with a simulated measurement with 600 lx of added ambient light and noise standard deviation of 1 gray level all with a pitch of 6 pixels for the a) sinusoidal 3-step b) triangular 3-step and c) triangular 2-step method. All errors shown are raw errors without any digital filtering applied.

greatly reduced to a MIGL of 105 (top left corner) the result was a rough surface and noisy measurement as a result of having a low intensity modulation and thus low SNR. Under ambient light of 600 lx at MIGL 255 (bottom right corner), measurement errors in the form of periodic ripples (seen as vertical lines) are apparent. The effectiveness of the method of adjusting the MIGL is seen where the MIGL has been reduced to 225 (the trade-off point) with 600 lx of added illuminance (middle column, bottom row), and the artifacts due to saturation are greatly reduced. Further reduction of the MIGL below the trade-off point (MIGL 105, left column, bottom row) results in high measurement error, as in the case with no added ambient light.

These results show that saturation was successfully avoided by lowering the MIGL. One problem with this method of saturation avoidance is that it is difficult to know how much the MIGL should be lowered to reach the trade-off point, since this point is based on having the lowest RMSE. The trade-off point seems to often be close to the point with the highest MIGL where there is no saturation; however, this may not always be the case. If there were a higher amount of added light, then there would be more saturation causing the trade-off MIGL to be lower. However, the error due to low SNR may prevent the trade-off MIGL from decreasing so that there is both error due to low SNR and saturation. In this case, the trade-off point will have a higher MIGL than the highest MIGL where there is no saturation. Another problem with this method of saturation avoidance is that it does not always maintain a high SNR since it only finds the best trade-off point in errors due to intensity saturation and low SNR. This may cause low accuracy when performing measurement with a large range of luminance since regions with low luminance, and therefore already having a low SNR, will have an even lower SNR when the MIGL is lowered to avoid saturation for the regions with high luminance. The LPA method, presented in the following chapter, aims to improve upon this method of saturation avoidance to MIGL by maintaining a high SNR when possible, and without requiring the trade-off MIGL to be known beforehand.

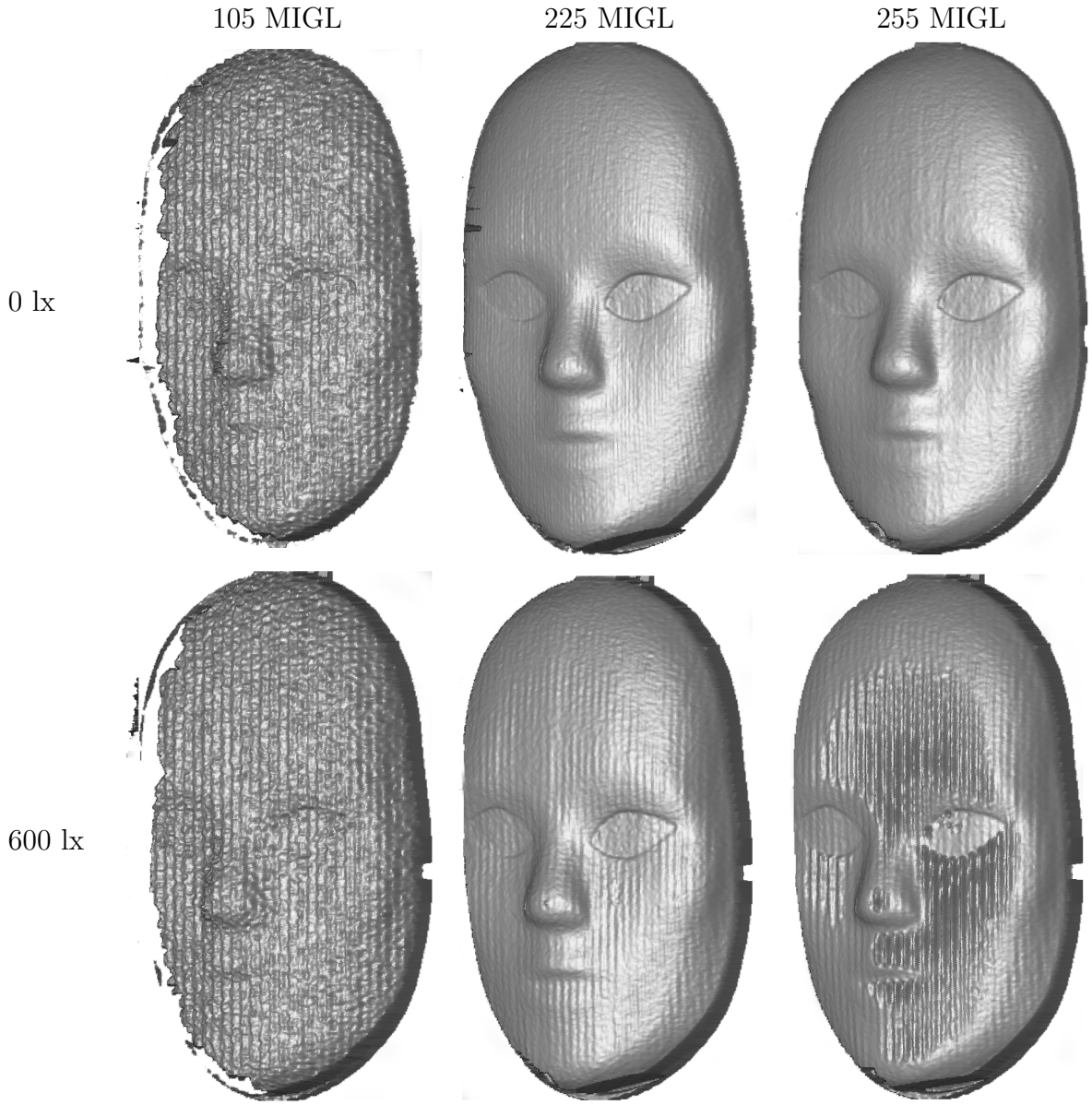

Figure 4.18: Measured mask surfaces with 105, 225, and 255 MIGL (across columns) and 0 lx (top row) and 600 lx (bottom row) of added ambient light during measurement.

Chapter 5

Linear Pixel-wise Adaptive Technique

While the previous method of lowering MIGL over an entire image was successful at avoiding saturation, the method may not be effective at measuring an object surface with a large range of reflectivity since it does not always maintain a high SNR across the entire image corresponding to the surface. This chapter presents another newly-developed method to avoid saturation and maintain a high SNR across the entire image when performing measurement with a large range of luminance. This method handles saturation avoidance pixel-by-pixel adaptively rather than uniformly as in the method discussed in the previous chapter. This helps to maintain a higher intensity modulation across the entire projected pattern than that by simply capturing images at the trade-off MIGL using the non-adaptive uniform adjustment of MIGL method described in Chapter 4. The linear pixel-wise adaptive method (LPA) presented in this chapter was inspired by the method of Zhang and Yau [79] who handled the captured images pixel-wise based on adjustment of the camera exposure time to eliminate saturation while maintaining a high SNR. The LPA method of saturation avoidance is described in Section 5.1. Experiments are presented in Section 5.2, and the results are compared with those of the non-adaptive uniform adjustment of MIGL method previously described in Chapter 4.

5.1 LPA Method

The LPA method of saturation avoidance makes use of one of the advantages of the phase-shifting technique, the ability to calculate the phase-map on a pixel-by-pixel basis. This allows the phase to be calculated from composite images with intensities

from the phase-shifted images captured at different MIGLs for different pixels in the composite image. This permits the handling of saturation avoidance while also maintaining a high SNR on a pixel-wise basis. Because of the pixel-wise treatment of images, the SNR of the LPA method would be higher that of the non-adaptive uniform adjustment of MIGL method and would thus better handle measurement with a large range of luminance. Essentially, the LPA method selects, for every pixel, the highest intensity-modulation without saturation in all of the intensities in a set of phase-shifted images among sets acquired at different MIGL. A pixel is identified as being saturated if any of its phase-shifted intensities are equal to the maximum gray level, $2^B - 1$, which, for an 8-bit camera ($B = 8$), is equal to 255. A set of composite phase-shifted images is formed from the selected unsaturated pixels chosen from different images. The image pixel intensities from sets of phase-shifted images can be acquired at different MIGL from pixel-to-pixel, but for a given pixel, all phase-shifted images must be acquired at the same MIGL. The composite images are expressed according to Equation 5.1 where $\breve{I}_i(x, y)$ is the ith phase-shift of the composite image, N is the number of steps or shifts used, and $I_i^{(k)}(x, y)$ is the ith phase-shifted image captured at k MIGL. The size of the MIGL steps is a predetermined by a constant S. The MIGL is decremented by S from the previous MIGL with the initial MIGL being the highest quantization level, $2^B - 1$. This initial MIGL yields the highest intensity modulation, and thus highest SNR, for a given camera aperture, and exposure time.

$$\begin{array}{c} \breve{I}_i(x,y) = \max(I_i^{(k)}(x,y) | I_1(x,y) < 2^B - 1, ..., I_{N-1}(x,y) < 2^B - 1) \\ i\text{=}0,1,2,3,...,\text{N-1} \qquad k\text{=}\ 2^B - 1, 2^B - S - 1, 2^B - 2S - 1, ..., 0 \end{array} \tag{5.1}$$

To create the composite images during a surface measurement the intensities from the phase-shifted images of the unsaturated pixels at the initial MIGL are captured and copied to the composite image. Then the intensities of the remaining pixels that are saturated at the initial MIGL are incrementally copied to the phase-shifted composite images as the pixels become unsaturated by repeatedly decrementing the MIGL by the predetermined constant step size, S. At each step, it is determined if saturation has still occurred for some pixels. If there are saturated pixels, then the MIGL is further decremented to the next step in MIGL, otherwise the composite images are considered complete. At this stage the phase-shifted composite images will be completely formed of unsaturated gray level intensities. Once the composite images have been computed, the phase calculation and unwrapping process proceed as with the conventional method to determine the height of the object surface of interest. The steps of this algorithm are summarized in the flowchart in Figure 5.1.

An example of a composite phase-shifted image formed using the LPA method using a sinusoidal pattern with a 6 pixel pitch is shown in Figure 5.2(b). On the

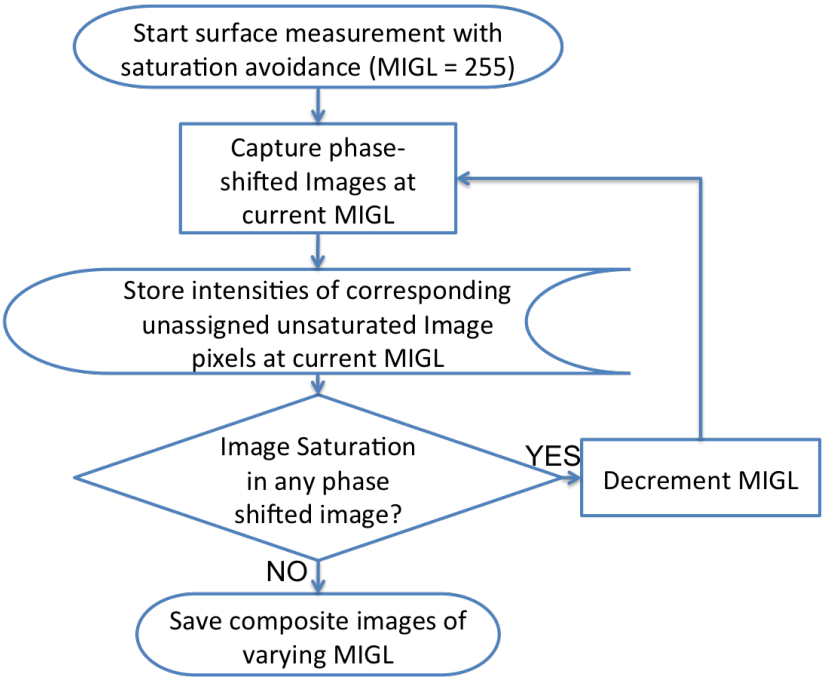

Figure 5.1: Flowchart for the linear pixel-wise adaptive method.

right, in Figure 5.2(c), is the corresponding index image, $N(x, y)$, which shows the MIGL used at each pixel. In this image, the gray level intensity corresponds to the MIGL chosen for that pixel.

The following experiments in Section 5.2 were used to determine the accuracy of the LPA method in the presence of a high degree of saturation.

5.2 Experiments

The intent of the LPA method is to maintain a higher SNR than the non-adaptive uniform adjustment of MIGL method while avoiding saturation. This section presents two separate experiments to examine the LPA method's ability to avoid saturation while maintaining a high SNR. The first experiment (Section 5.2.1) examines the ability to avoid saturation by measuring an object with a small range in reflectivity and camera sensor saturation caused by added ambient light. The second experiment (Section 5.2.2) examines the accuracy when measuring an object with a large range in reflectivity and no added ambient light. Saturation is caused by adjusting the aperture so that pixels corresponding to regions with low luminance have a high intensity modulation and pixels corresponding to regions with high luminance, saturate.

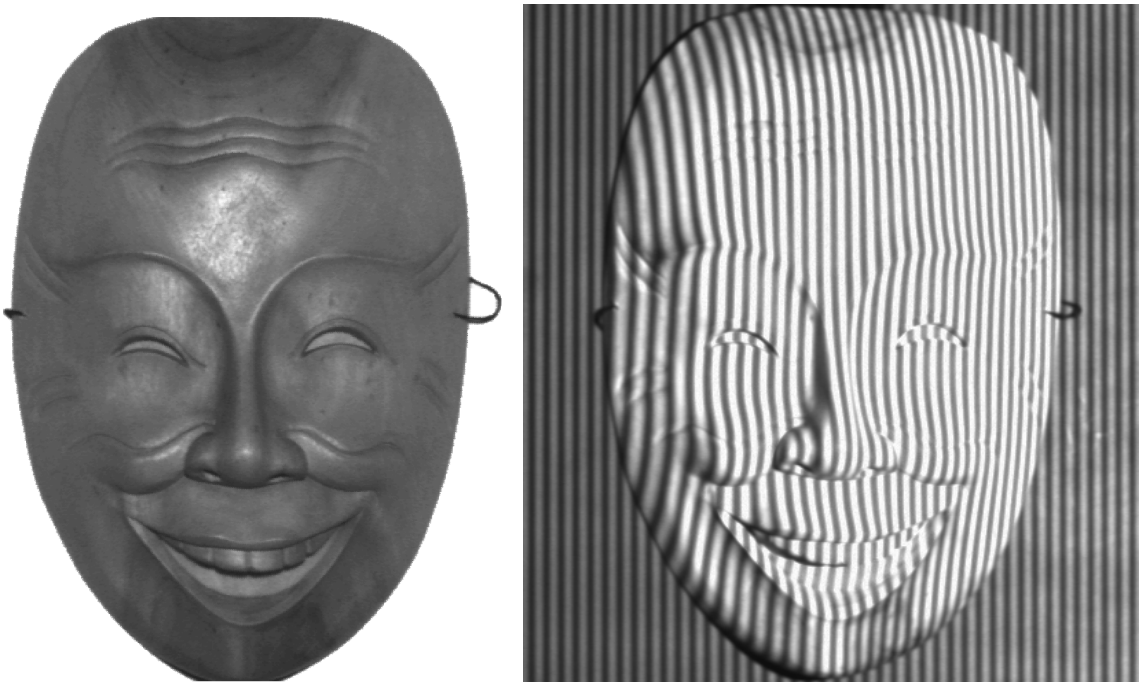

(a) (b)

(c)

Figure 5.2: Measurement of a wooden mask, shown in (a), using the linear pixel-wise adaptive (LPA) method of saturation avoidance with a constant step size of 5 gray level resulting in b) a composite phase-shifted image and c) the corresponding MIGL index image.

5.2.1 Small range in luminance and added ambient lighting

To compare the measurement accuracy using the LPA method with the non-adaptive uniform adjustment of MIGL method from Chapter 4 and the conventional method of measurement at 255 MIGL, 25 measurements with depths 2 mm apart, of a flat white plate using linearly decreasing MIGL of constant step size by 5 gray levels from the maximum gray level were taken with the pitch ranging from 4 to 20 at each plate position. Approximately 600 lx of light was added to the scene to cause saturation (as in Section 4.2). The composite phase-shifted images were computed using the phase-shifted images at different MIGL using the method described in Section 5.1. The RMSE was computed for each LPA measurement, and compared to earlier results from Chapter 4 for the non-adaptive uniform adjustment of MIGL method and conventional measurement at 255 MIGL. No image filters were used for the measurements presented in the following section to demonstrate the effect of low SNR on the raw error.

Results

Corresponding surface (right column) and contour (left column) plots of the RMSE for the LPA method (right column) are shown in Figure 4.9, for the sinusoidal 3-step, and the triangular 3- and 2-step, top to bottom rows, respectively. The mean RMSE computed with respect to depth is shown in Figure 5.4 which compares the measurement accuracy between the different patterns and number of shifts.

The RMSE of the measurements at 25 depths with a 6 pixel pitch using the LPA, conventional method at 255 MIGL, and the trade-off MIGL using the non-adaptive uniform adjustment of MIGL method are shown in Figures 5.5(a-c) for the sinusoidal 3-step, triangular 3-step, and triangular 2-step methods, respectively. The trade-off MIGLs used in the non-adaptive uniform adjustment of MIGL method for the different patterns are those shown in Table 4.3. Table 5.1 summarizes these results by showing the mean RMSE for each pattern and measurement method with 600 lx of added illuminance and a 6 pixel pitch. The table shows that the accuracy at the trade-off MIGL from the non-adaptive uniform adjustment of MIGL method is comparable, but slightly better, than the accuracy using the LPA method for each of the different fringe patterns and number of steps. Both methods clearly show a definite improvement over the conventional measurement at 255 MIGL for the 3-step patterns.

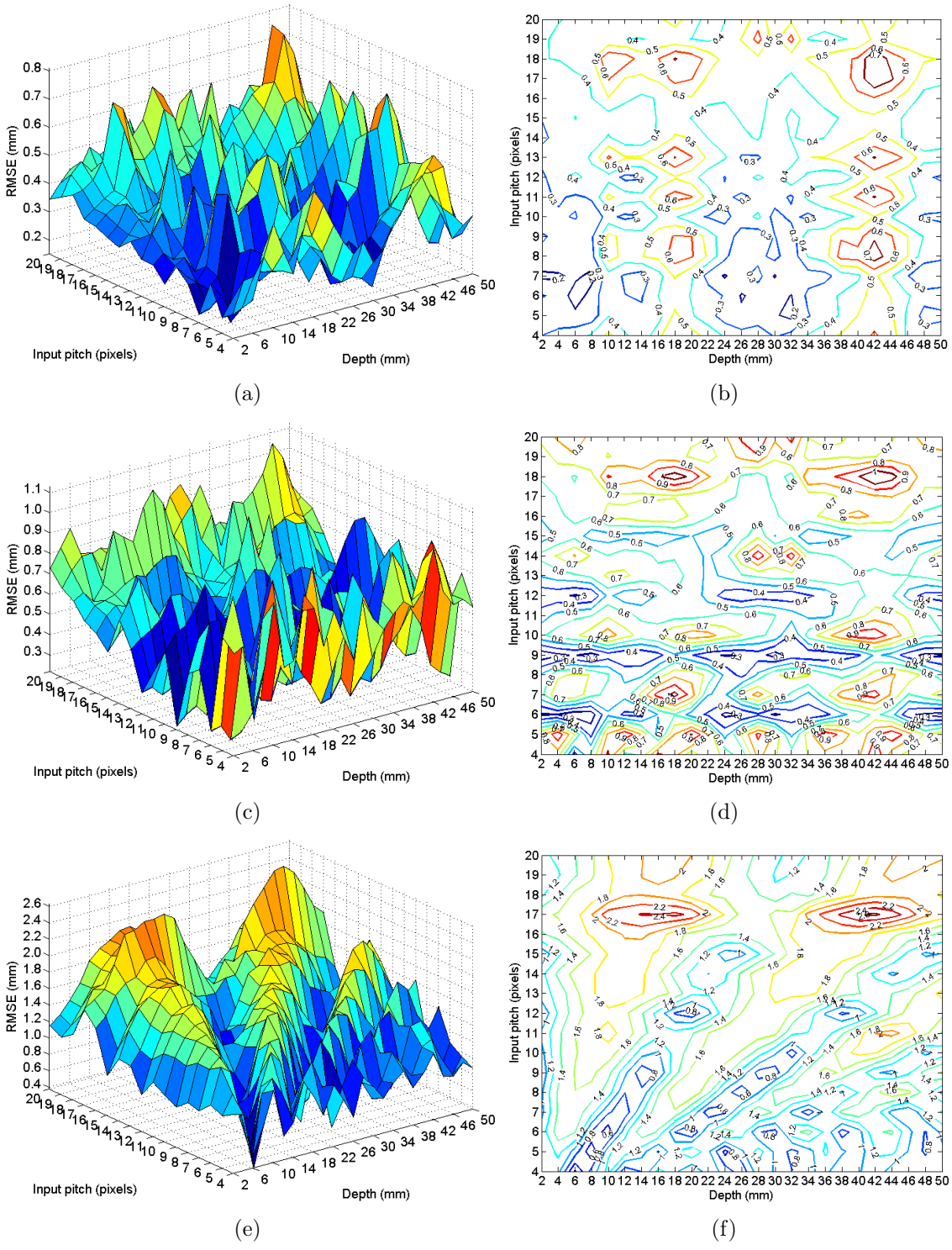

Figure 5.3: RMSE over the image with 600 lx of added ambient light for measurements using the LPA method with a constant step size of 5 gray levels, shown in (a,c,e) surface and (d,e,f) contour plots. Each row represents the (a,b) sinusoidal 3-step, and the (c,d) triangular 3 and (e,f) 2-step, respectively, with different pitches ranging from 4 to 20 at 25 measurement positions spaced 2 mm apart. The contours represent constant RMSE (mm).

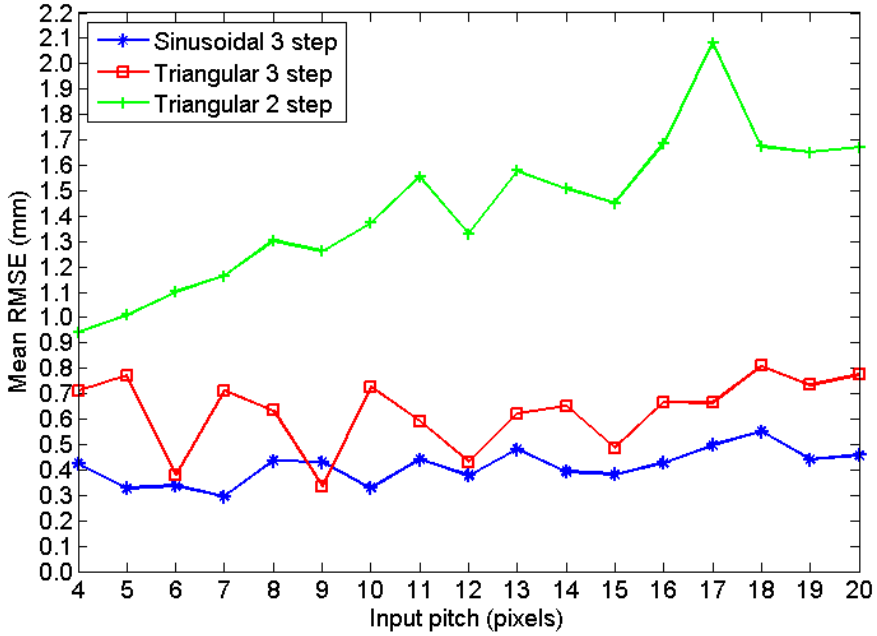

Figure 5.4: Comparison of the mean RMSE over depth and over the entire surface for measurements with 600 lx of added illuminance to cause saturation for different fringe patterns and number of phase-shifts with different pitches ranging from 4 to 20 pixels using the LPA method with a constant step size of 5 gray levels ranging from 255 to 225 to create the composite image.

Table 5.1: Mean RMSE for Measurements of a Flat White Plate with 600 lx of Added Illuminance at a 6 Pixel Pitch for each Method and Pattern

Pattern	LPA RMSE (mm)	255 MIGL RMSE (mm)	Trade-off MIGL RMSE (mm)
Sinusoidal 3-step	0.34	0.68	0.27
Triangular 3-step	0.38	0.53	0.33
Triangular 2-step	1.10	1.14	1.03

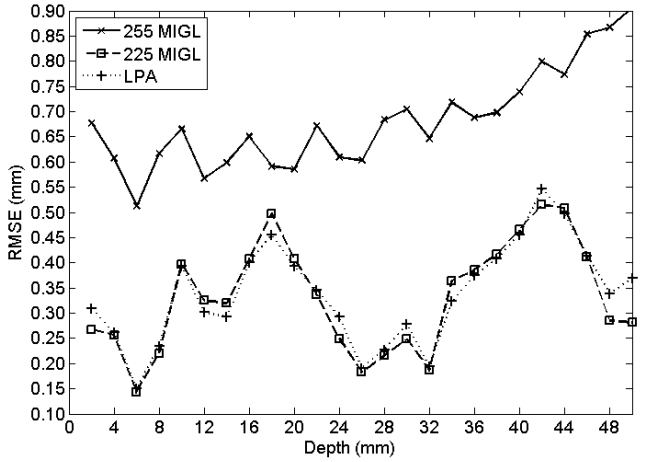

(a)

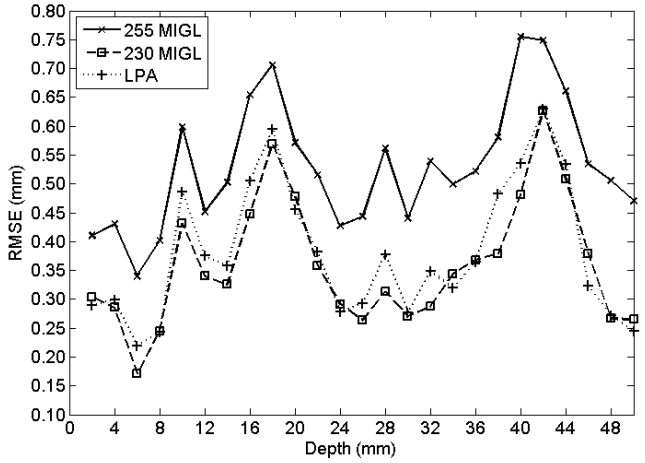

(b)

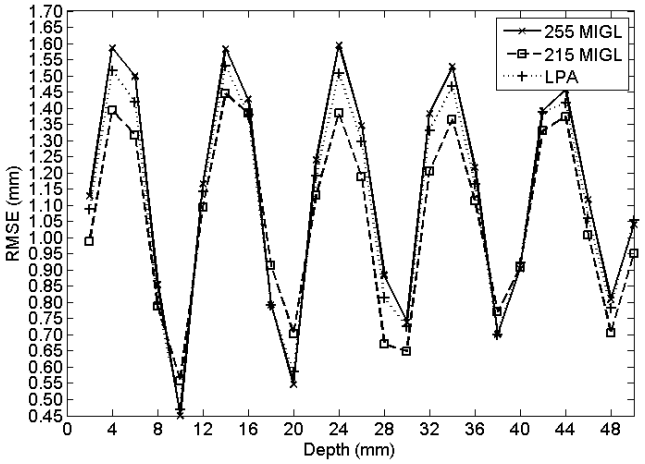

(c)

Figure 5.5: Comparison of errors between measurements at 255 MIGL (solid line), the trade-off MIGL (dashed line), and using the linear pixel-wise adaptive (LPA) method with a constant step size of 5 gray levels (dotted line). All methods including the (a) sinusoidal 3-step, (b) triangular 3-step, and (c) triangular 2-step method, have a pitch of 6 pixels and 600 lx of added ambient light.

Discussion

The results from measurement on the flat white plate with camera sensor saturation due to 600 lx of added ambient light show that the LPA method of saturation avoidance has higher accuracy than the conventional method of measurement at the maximum gray level (255), and approximately the same accuracy as the non-adaptive uniform adjustment of MIGL method from Chapter 4. These results are highly noticeable for individual measurements at all depths for the 3-step patterns and slightly more noticeable for the triangular 2-step pattern as shown in Figure 5.5.

The fact that measurement accuracy at the trade-off MIGL using the non-adaptive uniform adjustment of MIGL method is approximately the same as the LPA method shows that the pixel-wise approach with a composite image successfully avoids saturation. As well, the LPA method successfully overcomes the limitation of the uniform adjustment of MIGL method by finding the appropriate trade-off MIGLs at every pixel. However, according to the data modulation equation (Eq. 3.6) and the results from Section 4.2, it was hypothesized that the LPA method would have a higher accuracy than measurement at the trade-off MIGL using the non-adaptive uniform adjustment of MIGL method since the composite images used in the LPA method maintain a higher SNR at each pixel when it is possible. This is likely due to the small range of reflectivity across the surface when measuring the flat white plate. The LPA method would be expected to have higher accuracy when there is luminance variation across the object. However, this result gives merit to the non-adaptive uniform adjustment of MIGL method for measurement of surfaces with uniform reflectivity and thus luminance since it requires only one step, once the trade-off point is known, compared to the LPA method, which requires multiple steps, to avoid saturation.

To demonstrate that there is a negligible improvement in accuracy when measuring an object, such as a white plate, with a small range of luminance using the LPA method compared to the non-adaptive uniform adjustment of MIGL method, the RMSE was computed using only the pixels that just became unsaturated at each step in MIGL for the LPA method at the 25 depths. The results are shown in the left column of Figure 5.6 where the solid line is the RMSE computed over all pixels at the corresponding MIGL of the adaptive step and the dashed lines are one standard deviation of error from the mean. The standard deviation is computed over all pixels at the corresponding MIGL of the adaptive step. The right column shows a pie chart for the percent of pixels in the image that are grouped by the MIGL used to create the composite image. This corresponds to the graph in the left column of its respective row. Each row represents the different methods based on the combination of patterns and number of steps used for the measurement. In general, the RMSE over the different MIGL for the three cases have a constant error over different MIGL. The difference between the maximum and minimum RMSE for the MIGL used in the

composite image of the three step cases is approximately 0.05 mm. The two-step method has a larger difference between the maximum and minimum RMSE of 0.2 mm but this is still quite small since the standard deviation of error for the two-step method is much larger than the three step cases. The curves are somewhat flat in Figure 5.6 showing that there is no change in error using the pixel-wise approach with a constant step size of 5 gray levels from 255 to 225 MIGL when measuring the flat white plate. As previously shown in Figure 4.5, summing the percentages below the 255 MIGL in the pie charts from Figure 5.6 shows that there is significantly less saturation using the two-step case with 58% of the image saturated compared to 83% and 77% when using the sinusoidal and triangular three step cases, respectively. As well, the sinusoidal pattern is more prone to saturation with 6% more than the triangular 3-step pattern despite having the same number of steps and the same pitch.

The flat white plate measurement with an approximately uniform reflectivity is the simplest measurement object that can be used and does not represent most applications. In the following section, the potential ability of the LPA method to maintain a high SNR when possible to help increase accuracy when measuring with a large range of luminance was evaluated.

5.2.2 Large range of luminance and no added light

The results from the previous subsection showed that there was little difference in RMSE between the LPA and the non-adaptive uniform adjustment of MIGL method for saturation avoidance when measuring an object surface with a small range of reflectivity. The experiment presented in this section compares the LPA with the non-adaptive uniform adjustment of MIGL method for saturation avoidance when measuring a black and white checkerboard, an object with a large range of reflectivity across the surface. The checkerboard was mounted onto a 1 cm thick board which was attached to the reference plane and translation stage. Phase-shifted images using the sinusoidal 4-step method were captured at 10 measurement positions, 2 mm apart from 10 mm to 28 mm for 255 to 60 MIGL with a constant step size of 1 gray level and different pitches ranging from 5 to 20 pixels at each measurement position. The sinusoidal 4-step method was used as opposed to the other methods for comparison to the results for the method presented in the following chapter, which requires an additional phase-shift.

The PSFPP system was calibrated over 25 measurement positions from 2 mm to 50 mm using a flat black plate with the aperture adjusted for a high intensity modulation without camera sensor saturation. A black plate was used as opposed to the white plate so that calibration and measurement could be obtained using an aperture that is more sensitive to light (more open) so that intensity saturation would occur at the

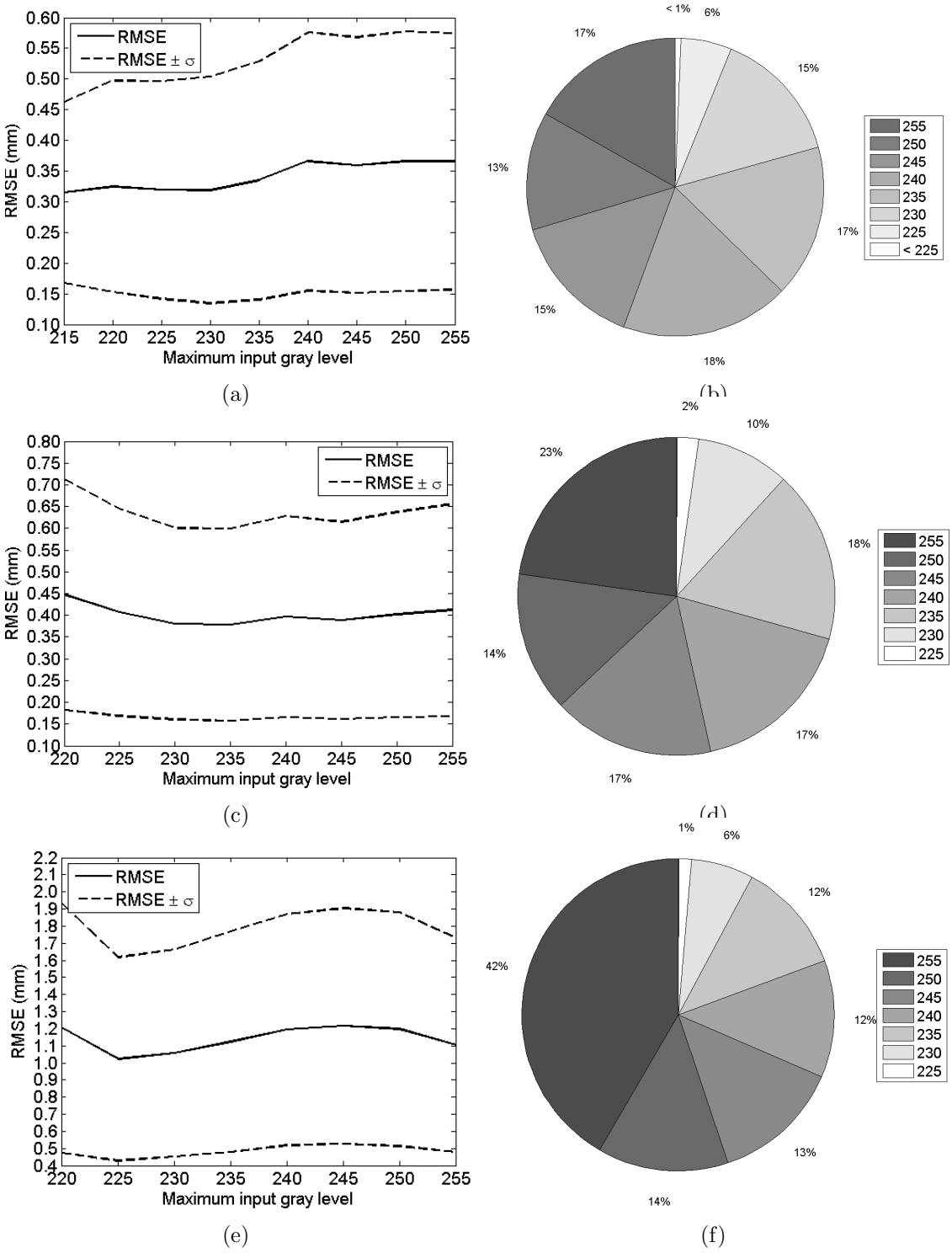

Figure 5.6: RMSE (a, c, e) computed at each step of the adaptive method over all pixels at the corresponding MIGL of the adaptive step and over 25 measurement depths spaced 2 mm apart. Pie charts (b, d, f) show the percentage of pixels copied to the composite image at the corresponding adaptive MIGL step. Each row represents the (a,b) sinusoidal 3-step, and the (c,d) triangular 3 and (e,f) 2-step, respectively, with a 6 pixel pitch.

pixels corresponding to the white squares when the checkerboard was measured at the maximum gray level. Calibration and measurements were conducted in a dark room with no ambient light. Composite phase-shifted images were computed using the phase-shifted images at different MIGL in eight separate sets of tests using constant step sizes of 1, 2, 3, 10, 15, 20, 30, and 45 gray levels using the method described in Section 5.1. The trade-off MIGL was found to be 96 using the non-adaptive uniform adjustment of MIGL method of saturation avoidance.

Results

The mean RMSE (Fig. 5.7(a)) and mean over depth of the standard deviation of measurement error (Fig. 5.7(b)) for the checkerboard using the LPA method are shown in Figure 5.7. Only constant step sizes of 10, 15, 20 and 30 gray levels are shown in Figure 5.7(a)(a-b) for clarity since a constant gray level step size of 1, 2, and 5 gray levels showed nearly identical results to the constant step size of 10 and 15 gray levels. This shows that there is little gain in RMSE having a constant step size below 15 gray levels when measuring the checkerboard using the LPA method. With a larger constant step size above 20 gray levels there is a large increase in RMSE as the pitch increases above 10 pixels. There does not appear to be any other trend associated with pitch accept that, in general, the RMSE is relatively low with a pitch between 8 and 13 pixels for a constant step size between 1 to 15 gray levels.

Unlike the RMSE, the mean standard deviation of error (Fig. 5.7(b)) shows a definite trend associated with having different gray level step sizes since a smaller step size gives a lower mean standard deviation for all the different values of pitch. An 8 pixel pitch has the lowest mean standard deviation of error when measuring the checkerboard and the mean standard deviation of error increases as the pitch increases or decreases with respect to the 8 pixel pitch. With an 8 pixel pitch there is only a small difference between the mean standard deviation of error with constant step sizes ranging from 1 to 30 gray levels as shown in Table 5.2 . However, as the pitch increases above 8 pixels there is a noticeable increase in the mean standard deviation of error for all step sizes especially with 20 and 30 gray levels. The mean standard deviation of error for these step sizes corresponds with the RMSE observed in Figure 5.7(a), which shows that the error is largely attributed to a low SNR.

Figure 5.8 shows the RMSE (Fig. 5.8(a)) and standard deviation of error (Fig. 5.8(b)) for the 10 individual measurements using a pitch of 8 pixels along with the measurements at the trade-off MIGL (96 gray levels) using the non-adaptive uniform adjustment of MIGL method with the sinusoidal 4-step pattern. Table 5.2 summarizes these results with constant step size of 1 and 15 gray levels along with the accuracy at the trade-off MIGL. Other constant step sizes are not shown in Figure 5.8 for clarity.

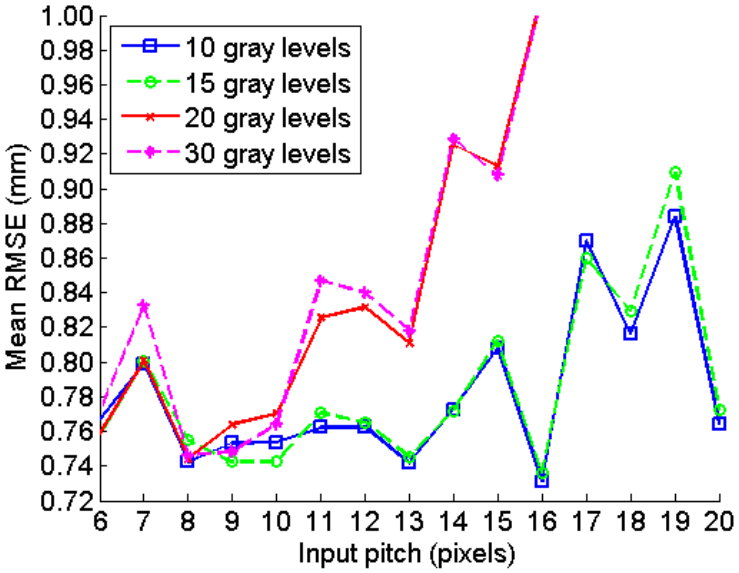

(a)

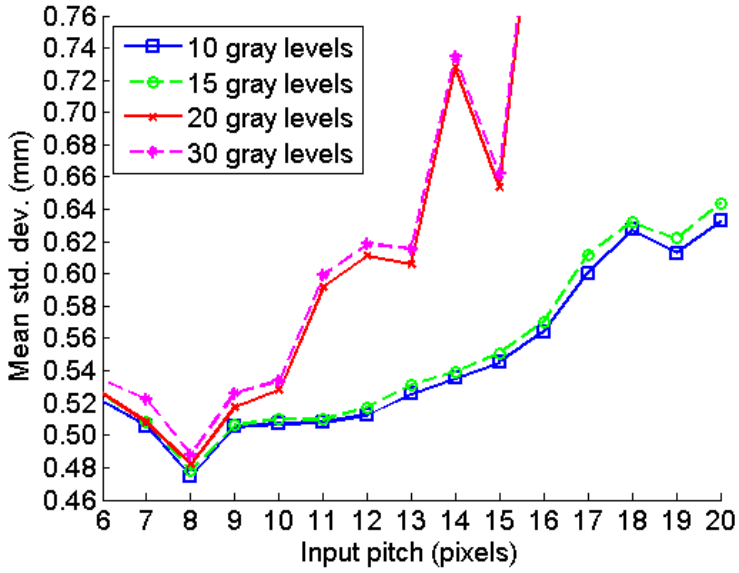

(b)

Figure 5.7: Results of measurements of a checkerboard using the sinusoidal 4-step method and linear pixel-wise adaptive (LPA) method for saturation avoidance with different pitch ranging from 5 to 20 pixels. (a) RMSE and (b) standard deviation of error computed over depth.

Table 5.2: Measurement Accuracy of a Checkerboard with a 8 Pixel Pitch

Step size (gray level)	# of Steps	Mean RMSE (mm)	Mean Std. Dev. (mm)
1	196	0.75	0.47
2	98	0.75	0.47
5	40	0.75	0.47
10	20	0.74	0.47
15	14	0.76	0.48
20	10	0.74	0.48
30	6	0.75	0.48
45	5	0.78	0.50
96 MIGL	1	1.01	0.83

5.3 Discussion

The results show that when performing a measurement with a large range of luminance (black and white checkerboard), as opposed to a small range of luminance (flat white plate), higher accuracy can be achieved by using the LPA method compared to the non-adaptive uniform adjustment of MIGL method. The higher accuracy is noticeable in Figure 5.8 using a pitch of 8 pixels. A 0.26 mm average improvement in RMSE was found when using the LPA method with a step size of one gray level compared to the measurement at the trade-off MIGL(96) using the non-adaptive uniform adjustment of MIGL method. The increase in accuracy with the LPA method was due to the higher SNR across the image that is obtained by using composite phase-shifted images rather than uniform MIGL phase-shifted images. This allowed the pixels corresponding to the dark square regions of the checkerboard, which have a lower reflectivity than the white squares, to have a higher SNR than with the non-adaptive uniform adjustment of MIGL method by capturing their intensities from the phase-shifted images at a high MIGL. Conversely, the pixels corresponding to the white squares, which have a high reflectivity, are captured at a low MIGL to avoid saturation. Although the input intensity modulation to the projector is somewhat small (only 30 gray levels with a MIGL of 70 and minimum input gray level of 40) the captured intensity modulation is still large, according to Equation 3.4, since the reflectivity of the surface is large and the camera sensitivity is large (open aperture).

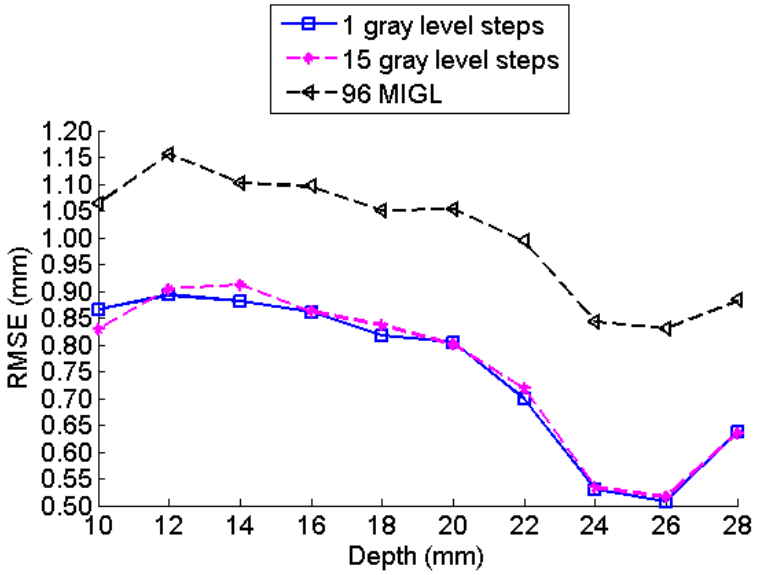

(a)

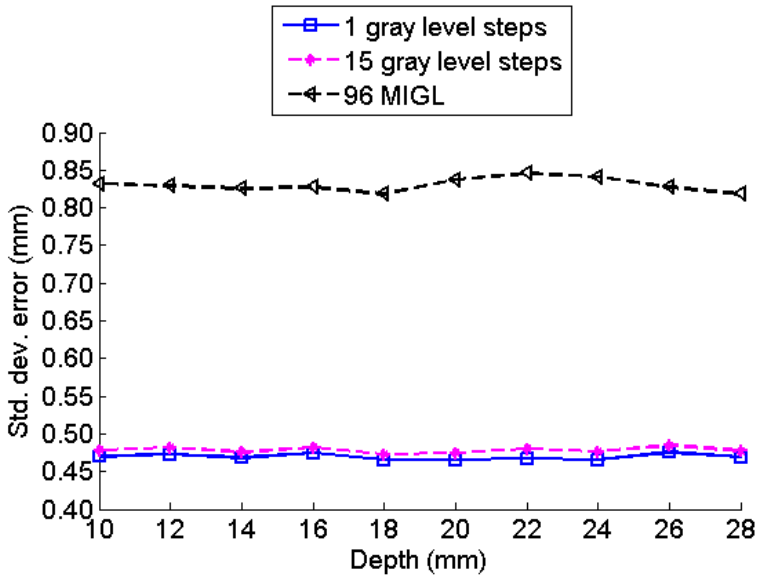

(b)

Figure 5.8: Results of measurements of a checkerboard using the sinusoidal 4-step method and linear pixel-wise adaptive (LPA) method for saturation avoidance with an 8 pixel pitch. (a) Mean RMSE and (b) mean standard deviation of error computed over depth.

Measurement at the trade-off MIGL (96 gray levels) using the non-adaptive uniform adjustment of MIGL method is not able to achieve the level of accuracy of the LPA method because intensity noise caused the trade-off MIGL to be larger than the MIGL where saturation no longer occurred (70 MIGL). This means that with a large range of luminance the non-adaptive uniform adjustment of MIGL method is unsuccessful at fully avoiding saturation and instead attempts to get the best trade-off in error due to saturation and low SNR to achieve the minimum error with only a single step once the trade-off MIGL is known.

A 3D rendering of the checkerboard obtained using the non-adaptive uniform adjustment of MIGL method with the trade-off at 96 MIGL is shown in Figure 5.9. In this figure, the dark and light regions of the checkerboard are recognizable since the dark regions appear rougher than the white squares due to low SNR. A profile of the checkerboard on the right shows large spikes in measurement error due to the low SNR in the dark regions. The SNR is worst for the black squares of the checkerboard on the left which had the lowest captured intensity at the initial MIGL. This is caused by a light gradient that is created by having the projector at an angle so that the right side of the plate is closer to the projector than the left side of the plate. This causes the right side to receive a higher projected light intensity and therefore have higher SNR than the left side.

The measurement accuracy using the LPA method was higher than for the non-adaptive uniform adjustment of MIGL method for a large range of luminance and had comparable accuracy for a small range of luminance. The LPA method takes more steps than the non-adaptive uniform adjustment of MIGL method since it needs several sets of phase-shifted images at different MIGL to compute the composite phase-shifted images. This may lead to extensive processing if the linear step size is chosen to be too small. This was the case in Section 5.2.1 when measuring the flat white plate with added ambient light since only a single capture at the trade-off MIGL was needed to achieve high accuracy. If the linear step size is too large then this may lead to high measurement error. This was the case when measuring the checkerboard in Section 5.2.2, where a linear step size less than 20 gray levels achieved higher accuracy.

To handle these two situations, an operator must determine the linear step size ahead of time if there is a large pitch. Even if the operator selects a good step size for the problem, the LPA method does not ensure that there will be newly unsaturated pixels that can be added to the composite image at each step. This would be inefficient processing when computing the composite phase-shifted image. As well, the LPA method is restricted to only using a predetermined constant step size in gray level. Instead the step size should ideally be based on the range of luminance from an object surface. To resolve these issues, an improved method should have a

dynamic step size based on the degree of saturation or range of luminance.

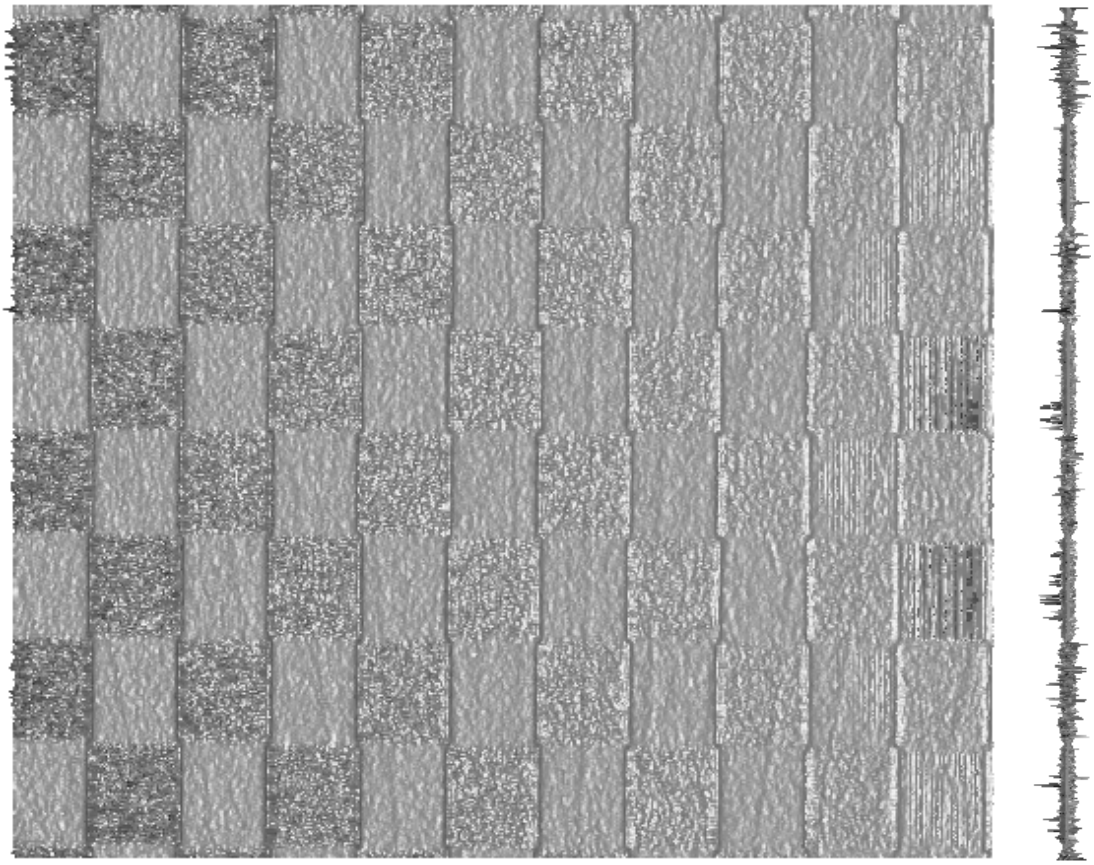

Figure 5.9: Three-dimensional surface rendering of a checkerboard at the trade-off MIGL (96 gray level) when using the non-adaptive uniform adjustment of MIGL method with the sinusoidal 4-step fringe pattern and an 8 pixel pitch. To the right of the checkerboard is a profile view of the checkerboard surface. A single pass by a 3×3 pixel mean and 3×3 pixel median filter were performed on the measurement result to reduce high frequency noise.

Chapter 6

Dynamic Pixel-wise Adaptive Technique

The LPA method, used in Chapter 5, improves the measurement accuracy compared to the non-adaptive uniform adjustment of MIGL method in the presence of image saturation when performing measurement with a large range of luminance. However, the LPA method requires multiple steps at different MIGL to compute the composite phase-shifted images and the method does not ensure that newly unsaturated pixels are added to the composite images at each step. This makes the LPA method inefficient. The saturation avoidance method presented in this chapter improves upon the LPA method from the previous chapter by dynamically choosing the step size based on the degree of saturation. The dynamic pixel-wise adaptive (DPA) method is described in Section 6.1, while Section 6.2 details the experiments followed by results in Section 6.3 and discussion in 6.4, respectively.

6.1 DPA Method

Rather than using a constant predetermined step size as in LPA, the DPA method dynamically chooses the step size at each iteration. This helps to ensure that at least some newly unsaturated pixels are added to the composite image at each iteration. The step size is estimated using a cumulative distribution function (CDF) of the highest true intensities among phase-shifted images for the saturated pixels at the initial MIGL if camera sensor saturation had not occurred. As the MIGL is lowered to avoid saturation, the CDF gives the estimated percentage of pixels that should become unsaturated at the next step. The estimated percentage of pixels is compared to the cumulative percentage of pixels which was estimated at the previous step. If the

percentage difference is greater than some threshold percentage then phase-shifted images are captured at that corresponding MIGL. Otherwise the MIGL is lowered further, without projecting patterns and capturing images at that MIGL.

The saturated intensities must be determined to calculate the CDF used to determine the step size. Because not all of the intensities in the phase-shifted images are known, due to saturation, the unknown intensities are estimated using the phase-shifting relationship between the intensities of all the phase-shifted images at the same pixel. This is illustrated in Figure 6.1 which shows the cross-section of four phase-shifted sinusoidal fringe-patterns with one of the phase-shifted intensities saturated. Using the three known intensities from the phase-shifted images at a given pixel, the unknown intensity can be estimated based on the relationship between the phase-shifts. This pixel-wise relationship is also what is used to compute the depth at a given pixel and is holds true regardless of the reflectivity of the object surface. However, a higher intensity modulation improves the accuracy of the estimate because there will be less quantization error. The method used to estimate the unknown intensities with the relationship between intensities from the phase-shifted images is discussed in Section 6.1.1. Even with a high intensity modulation, this method of estimating the unknown intensities is very sensitive to inaccuracies in the phase-shifted fringe pattern intensities such as projector nonlinearity, and intensity noise. This results in significant error in estimating the saturated intensities. To cope with this problem, a compensation method, described in Section 6.1.2, is used to correct the estimate to a closer approximation of the unknown intensity. Once the unknown intensities are known, then a histogram of saturated intensities can be calculated. This histogram is used to create the CDF by summing the scores in the bins across the histogram and dividing by the total number of saturated pixels. A more detailed description of how the CDF is created is given in Section 6.1.3. The method then continues in a similar manner as the LPA method in Chapter 5 but it uses non-constant step sizes of MIGL to create the composite image, which is used to compute the object surface depth.

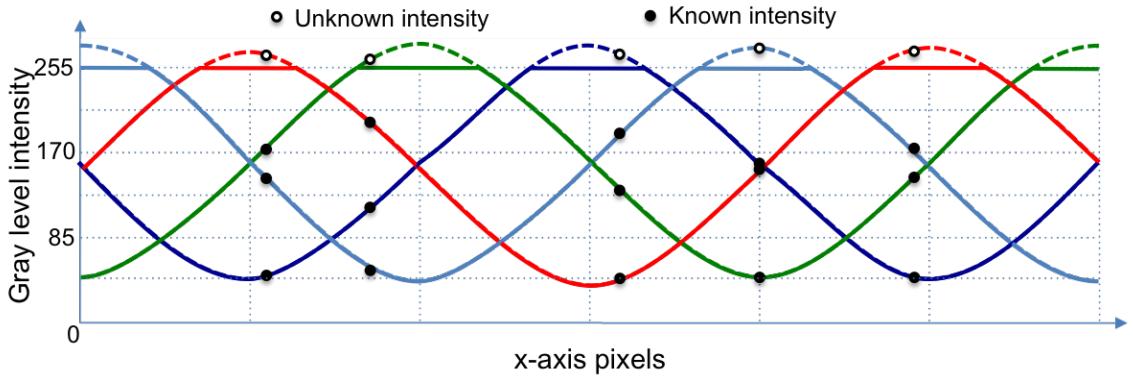

Figure 6.1: Pixel-wise sinusoidal relationship with four phase-shifted patterns. The dotted curves indicate the true intensities if camera sensor saturation had not occurred but saturated when captured by the camera. The known unsaturated intensities can be used to estimate the unknown saturated intensity based on the relationship that exists between the sinusoidal phase-shifted patterns at a given pixel.

6.1.1 Unknown saturated intensity estimation

The method to determine the unknown saturated intensities is a deterministic approach. The approach computes the unknown saturated intensities using the equations of the fringe pattern (Eq. 2.1 for the sinusoidal fringe pattern and Eq. 2.3 for the triangular fringe pattern). The advantage of this approach is that it does not depend on the pattern pitch. However, the deterministic approach is specific for a certain pattern and number of phase-shifts. Only the sinusoidal pattern is used in this chapter to solve for the saturated intensity since equations for the sinusoidal pattern are simpler than for the piece-wise triangular fringe pattern. A probabilistic approach, which does not depend on the type of pattern, was also tested. However, this approach was less successful and is discussed further in Chapter 7 regarding future work.

The deterministic approach treats the saturated intensity as an unknown but the approach requires additional phase-shifts, and thus additional equations, to solve for these unknowns. Using a sinusoidal fringe pattern with m saturated phase-shifted intensities at a given pixel, a total of $3 + m$ phase shifts ($2 + m$ for the triangular pattern) are needed to solve for the unknowns. The expression for the unknown saturated intensity using a sinusoidal pattern is derived using the $3 + m$ phase shifts from Equation 2.1. This is shown below using four phase-shifts ($m = 1$) to solve for one saturated intensity.

$$I_i(x,y) = a(x,y) + b(x,y)cos[\phi(x,y) + \frac{2\pi i}{N}], \quad i = 1,2,3,4 \quad N = 4 \tag{6.1}$$

As described in Section 2.2, this equation has three unknowns: $a(x,y)$, $b(x,y)$, and $\phi(x,y)$. In the case when saturation occurs at a given pixel in one of the phase-shifts, $I_i(x,y)$, then there is an additional unknown. By solving, and simplifying the system of equations from Equation 6.1 the unknown saturated intensities can be solved in terms of the known intensities from the phase-shifted images as shown in Equation 6.2. In these equations the subscript on $I(x,y)$ indicates the ith phase-shift according to $\frac{2\pi i}{N}$ and $\hat{I}_i(x,y)$ is the unknown saturated intensity estimate.

$$\begin{array}{l|l} \hat{I}_1(x,y) = I_4(x,y) - I_3(x,y) + I_2(x,y) & \mathrm{I}_1(x,y) = 2^B - 1 \\ \hat{I}_2(x,y) = I_3(x,y) - I_4(x,y) + I_1(x,y) & \mathrm{I}_2(x,y) = 2^B - 1 \\ \hat{I}_3(x,y) = I_2(x,y) - I_1(x,y) + I_4(x,y) & \mathrm{I}_3(x,y) = 2^B - 1 \\ \hat{I}_4(x,y) = I_1(x,y) - I_2(x,y) + I_3(x,y) & \mathrm{I}_4(x,y) = 2^B - 1 \end{array} \tag{6.2}$$

6.1.2 Unknown saturated intensity correction

Ideally, the result from Equation 6.2 gives the true unsaturated intensity for a given saturated pixel from the phase-shifted images. However, various sources of error such as inaccurate projector nonlinearity correction, noise, and camera quantization may prevent the projection of a purely sinusoidal pattern, which these equations assume. To correct the estimated intensity, a function for the error is estimated using training data. This function is used to correct the result from Equation 6.2. The true intensity value of the unknown saturated pixel is accurately estimated by applying the LPA method with a constant step size of one gray level and recording the highest MIGL for a pixel when each phase-shifted intensity becomes unsaturated. The unknown saturated intensity $I_i^{**}(x,y)$ can then be computed when the MIGL is at the maximum gray level (255 for an 8-bit camera) using Equation 6.3.

$$I_i^{**}(x,y) = 2^B - 1 + (2^B - 1 - N(x,y)) \tag{6.3}$$

where $N(x,y)$ is the highest MIGL at pixel (x,y) given that all of the phase-shifts are unsaturated. This result is added to the unknown saturated intensity estimate in Equation 6.2 to give error ($\hat{\varepsilon}$) according to Equation 6.4.

$$\hat{\varepsilon} = \hat{I}_i(x, y) - I_i^{**}(x, y) \tag{6.4}$$

After gathering enough training data with a wide range of intensities, a low order polynomial is fit to the data to create an equation that gives the expected error for the unknown saturated intensity estimate from Equation 6.2. This error estimate, $\hat{\varepsilon}$, is subtracted from $I_i^{**}(x, y)$ to get a better estimate of the unknown saturated intensity.

The training data that is used for the experiment of the DPA method in Section 6.2 are 25 sets of phase-shifted images with a projected sinusoidal fringe pattern using a large pitch of 20 pixels on a flat white plate. This is sufficient since the sinusoidal relationship between the intensities from the phase-shifted images is the same regardless of the reflectivity or shape of the surface from the perspective of the camera. Using a large pitch helps to obtain a wide range of phase-shifted intensity relationships. These are needed to fit a polynomial between the error estimate, $\hat{\varepsilon}$, and the full range of estimated saturated intensities from Equation 6.2. The polynomial and the error estimates corresponding to the estimated saturated intensity from Equation 6.2 are shown in Figure 6.2. After unknown saturated intensity correction is applied, the RMSE computed from Equation 6.4 was 2.99 gray level compared to 71.05 gray level without correction.

6.1.3 Estimation of the cumulative distribution of saturated intensities

After correcting the estimated saturated intensities from Equation 6.2 using the polynomial from Figure 6.2, a histogram of the intensities is created. This is in turn converted into a CDF by summing the scores in the bins as the MIGL decreases. This initial estimate of the CDF is used to determine the step size by computing the difference in CDF values for the current MIGL step and the previous MIGL step when phase-shifted images were captured. If the value from the CDF at the current step is greater than a threshold percentage, then phase-shifted images are captured at the corresponding MIGL, otherwise, the MIGL is decremented.

At each step where the phase-shifted images are captured, the CDF is updated so that there is not an accumulation of error when estimating the step size. The CDF must also be updated because the deterministic saturated intensity estimation (DSIE) method is only able to estimate saturated pixels with one saturated intensity. Two updates are made to the CDF. The first is to estimate the intensity of pixels, using Equation 6.2 and the polynomial from Figure 6.2, which formerly had more than one saturated intensity in a phase-shifted image but at the current MIGL step has only one saturated intensity in a phase-shifted image. These pixels are added to

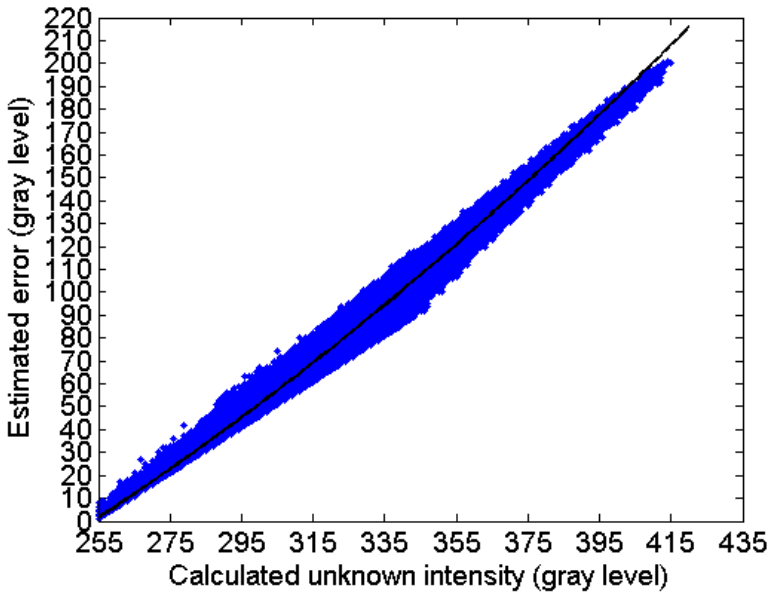

Figure 6.2: The compensation map to correct the estimate from the unknown saturated intensity from Eq. 6.2. The X-axis is the output from Eq. 6.2 and the Y-axis is the expected error. The black line shows a polynomial function that is fit through training data to relate calculated unknown intensity to the estimated error. This relationship is used to correct the calculated unknown intensity by added the error back into the result from Eq. 6.2 to get a better estimate.

the CDF by creating a histogram, summing the scores in the bins and then adding to the CDF. The second update is to add the number of pixels that formerly had more than one saturated intensity at a given pixel in the phase-shifted image but are unsaturated at the current MIGL step. These two updates to the CDF allow pixels with multiple saturated phase-shifted intensities to be added to the CDF.

If the threshold percentage to determine whether the CDF needs to be updated is too large, and the range of luminance for the measurement is large, then updates may be too infrequent to estimate the next step size using the CDF. This prevents the MIGL from being decremented and the addition of unsaturated intensities to the composite images. This is because the DPA method relies on the updates of previous steps to estimate the next step size. This issue is resolved by capturing the phase-shifted images at the MIGL step when the difference between the CDF value at the current MIGL and CDF value at the lowest MIGL is less than a small threshold (0.01% is used in the experiment). Since the CDF is monotonically increasing, the CDF value at the lowest MIGL is always greater than or equal to the CDF value at the current MIGL. This method of invoking the capturing of phase-shifted images before reaching the percent threshold helps to prevent the CDF value at the current MIGL from being equal to the CDF value at the lowest MIGL unless the lowest MIGL value has reached 100%. This method is invoked less if the CDF is somewhat continuous and/or has a steep slope due to there being a smaller range of luminance. The CDF is often continuous since the fringe pattern itself offers a variety of intensities causing saturation to vary slightly between pixels. Using a larger pitch offers a wider variety of intensities and this helps when updating the CDF at each step. This is explored further in the experiment presented in the following section.

6.2 Experimental procedure

The intent of developing the DPA method is to achieve a comparable accuracy to the LPA method but with a fewer number of steps, and without having to manually make adjustments to parameters based on the range of luminance or degree of saturation. Experiments were performed on a flat white plate and a checkerboard, which represent a small and large range of reflectivity, respectively, to determine the accuracy and number of steps by adjustment of the MIGL. The measurements of the checkerboard using the DPA method were performed using the same phase-shifted images captured for the LPA method in Section 5.2.2. The same procedure to acquire the checkerboard images was also used to acquire images of the flat white plate using the sinusoidal 4-step method but with 600 lx of added ambient light to cause saturation. Calibrations were re-performed on the white plate rather than the black plate to ensure that no

error was introduced by the adjusting the aperture for measurement of the white plate.

6.3 Experimental results

The actual (left column) and estimated (right column) CDF of the measurements for the flat white plate (top row) and checkerboard (bottom row) with a 8 pixel pitch is shown in Figure 6.3. The actual CDF was generated by computing the histogram using the unknown saturated intensities calculated by Equation 6.3 and summing the scores in the bins. While not exact, the two estimated CDFs share a similarity in shape with the actual CDFs. The actual and estimated CDFs for the checkerboard more closely resemble each other compared to the CDFs for the flat white plate since more steps were needed with a large range of luminance when measuring the checkerboard. The discontinuities in the estimated CDFs indicate where MIGL estimates have taken place by updating the CDF by adding unsaturated and unestimated pixels to the CDF as described in Section 6.1.3.

The results for the mean RMSE computed over depth for the different values of pitch are shown in Figure 6.4. For the white plate (Fig. 6.4(a)) the mean RMSE computed at different pitch is slightly better with the DPA method than the LPA method when averaged over the different pitches as shown in Table 6.1. The results of the DPA method for the checkerboard (Fig. 6.4(b)) are nearly the same as the best case shown using the LPA method with a constant step size of 15 gray level. In this plot, both the 10% and 20% step size have the same accuracy since they have the same MIGL steps because capturing of the phase-shifted images at the MIGL step is invoked before reaching the 10% or 20% threshold as discussed in Section 6.1.3. This prevents the DPA method from having too few steps which would have resulted in poor accuracy as exhibited by the LPA solutions for the cases of 20 or 30 gray level step size.

The mean over depth of the standard deviation of error over pixels, shown in Figure 6.5, reflect the RMSE results from Figure 6.4. The DPA curves are similar to the LPA method for all flat white plate measurements and for the checkerboard using a 15 gray level steps size. Step sizes shown for the LPA method above a 15 gray level step size have growing mean standard deviation of error as the pitch increases above 8 pixels.

The number of MIGL steps to compute the composite images is shown in Figure 6.6. For the flat white plate (Fig. 6.6(a)) the 10% step size using the DPA method has a comparable number of steps to the 10 gray level step size when using the LPA method. The 10% step size had slightly higher accuracy than the 10 gray level step

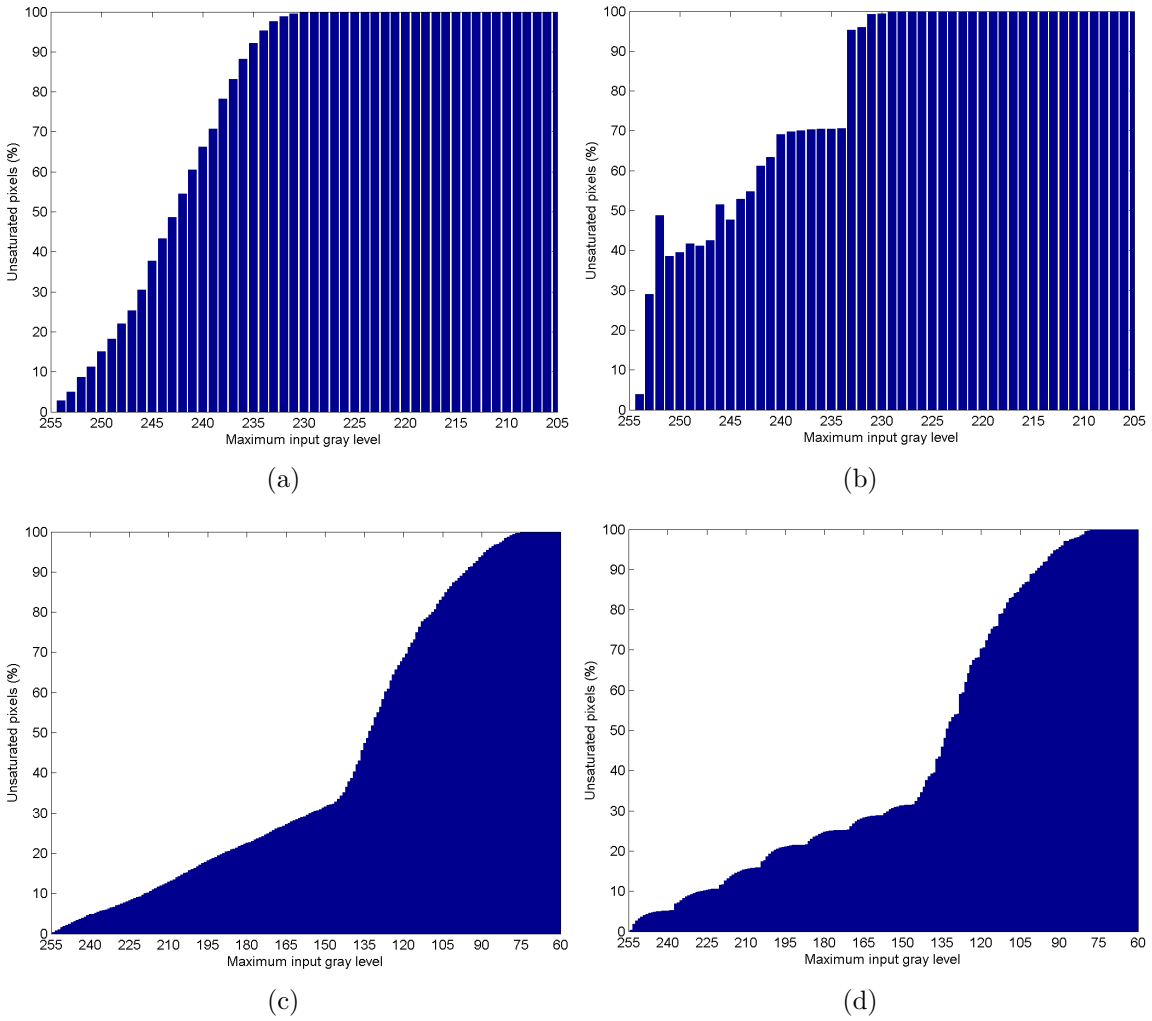

Figure 6.3: Cumulative distribution function (CDF) of the saturated intensities from the measurement of (a,b) a flat white plate and (c,d) a checkerboard using a sinusoidal 4-step fringe pattern with an 8 pixel pitch. (a,c) The actual CDF is derived from the intensities calculated using Eq. 6.3 and (b,d) the estimated CDF is derived from estimated intensities calculated using Eq. 6.2 and the DPA method.

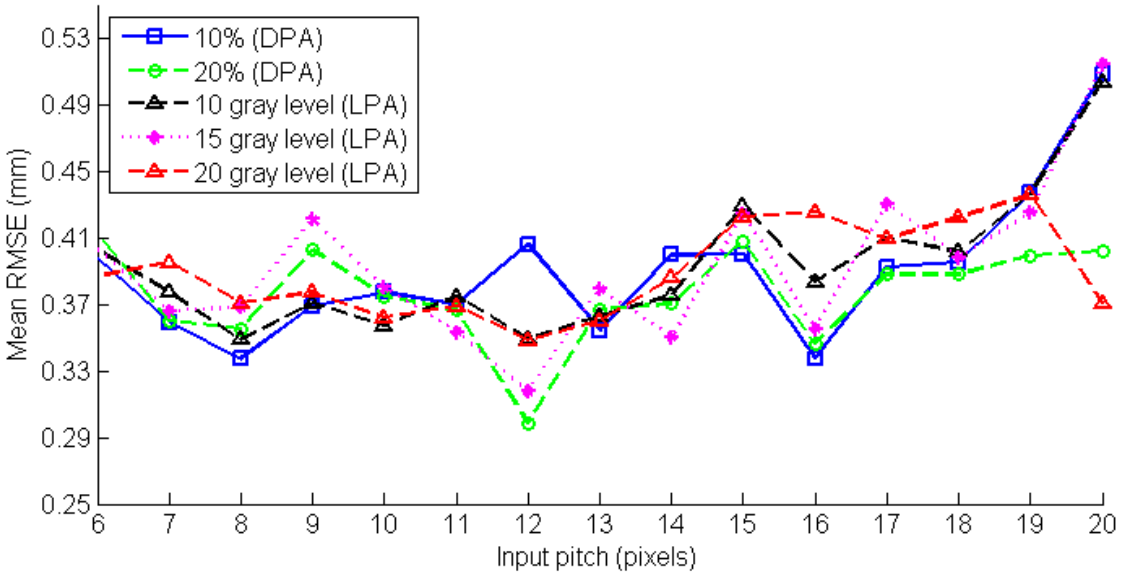

(a)

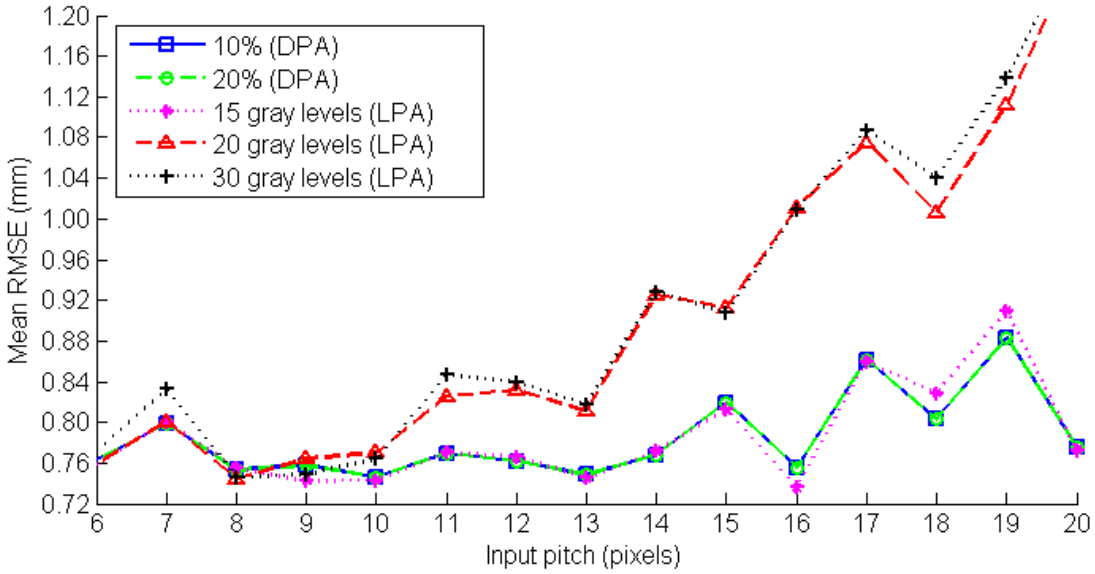

(b)

Figure 6.4: Results of measurements of (a) a flat white plate and (b) checkerboard with curves of mean RMSE over depth using the sinusoidal 4-step method with different pitches ranging from 6 to 20 pixels. Measurements were performed using the dynamic pixel-wise adaptive (DPA) method for saturation avoidance with dynamic step sizes of 10% and 20% and the linear pixel-wise adaptive (LPA) method with constant step sizes of 10, 15, and 20 gray level for the flat white plate and 15, 20, and 30 gray level for the checkerboard.

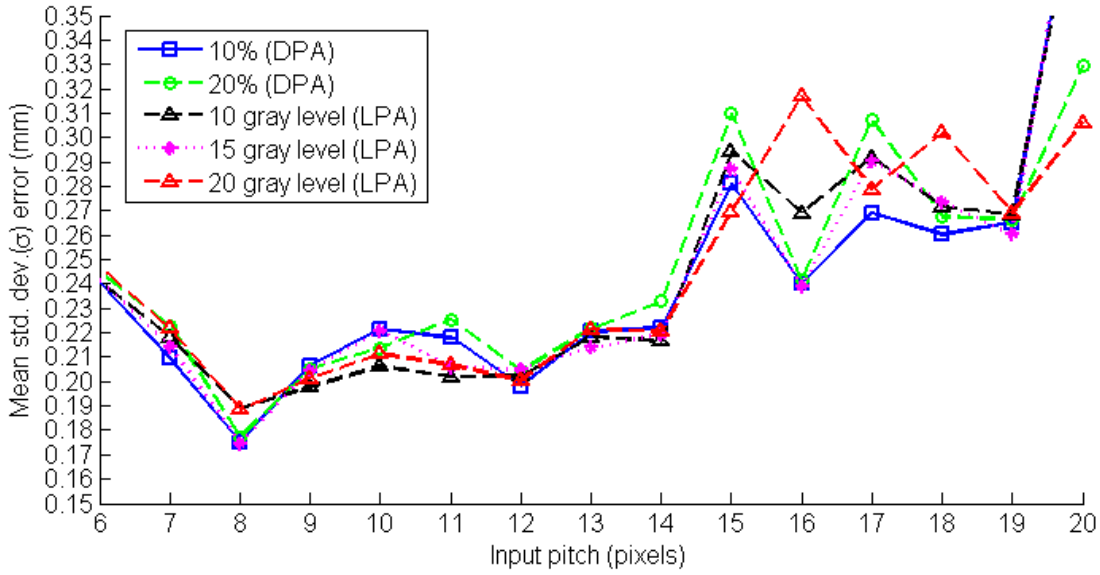

(a)

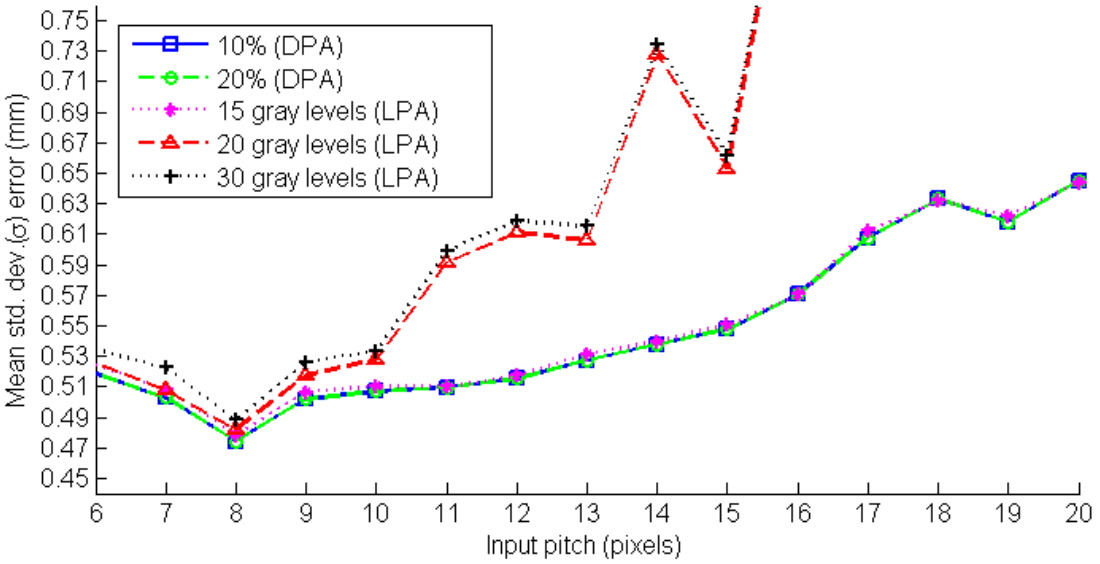

(b)

Figure 6.5: Results of measurements of (a) a flat white plate and (b) checkerboard with curves of mean standard deviation of error over depth using the sinusoidal 4-step method with different pitches ranging from 6 to 20 pixels. Measurements were performed using the dynamic pixel-wise adaptive (DPA) method for saturation avoidance with dynamic step sizes of 10% and 20% and the linear pixel-wise adaptive (LPA) method with constant step sizes of 10, 15, and 20 gray level for the flat white plate and 15, 20, and 30 gray level for the checkerboard.

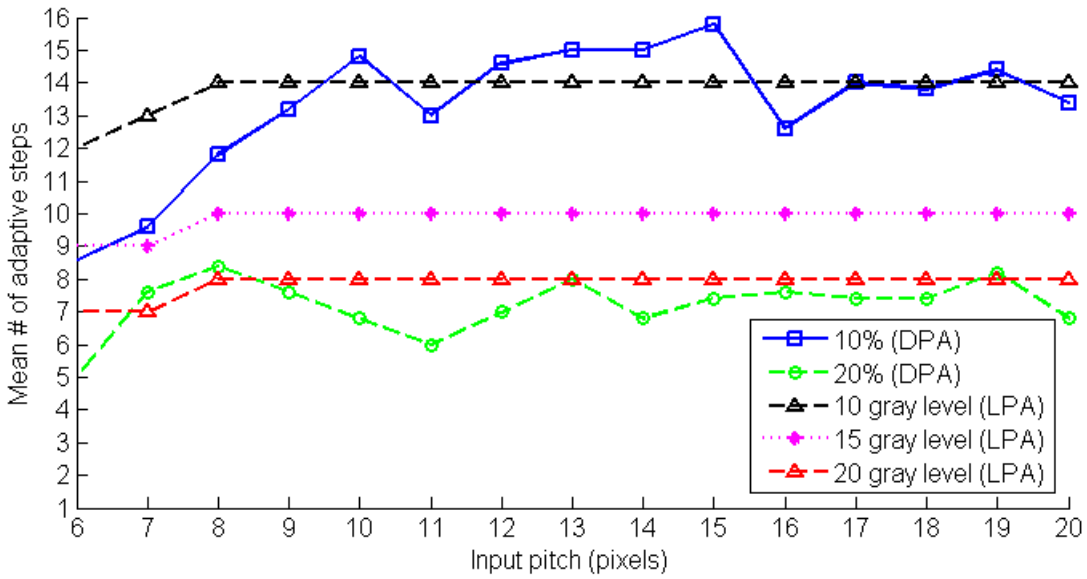

(a)

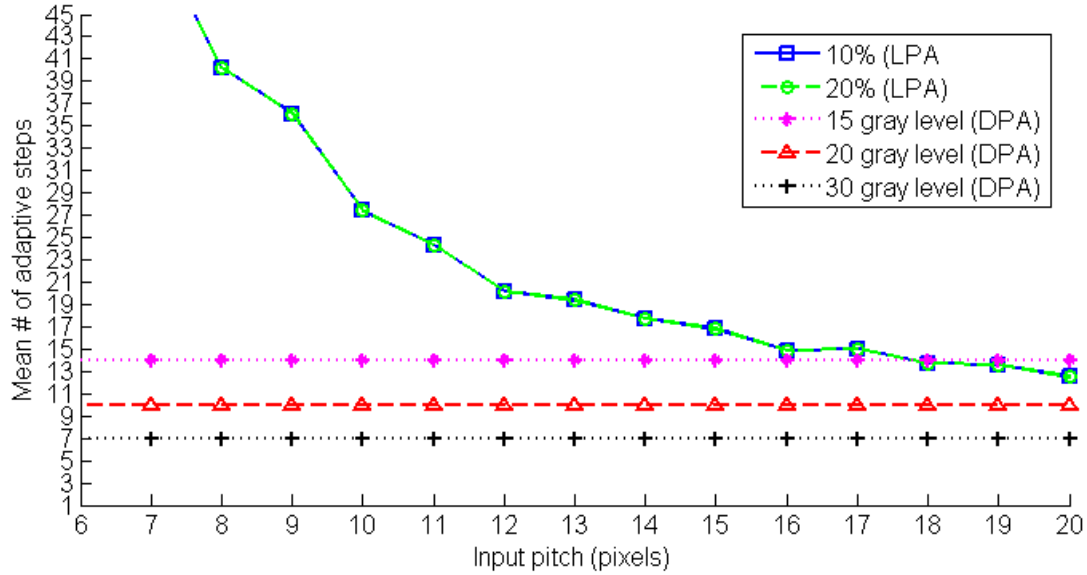

(b)

Figure 6.6: Comparison of the number of steps from measurement of (a) a flat white plate and (b) checkerboard using the sinusoidal 4-step method with different pitches ranging from 6 to 20 pixels. Measurements were performed using the dynamic pixel-wise adaptive (DPA) method for saturation avoidance with dynamic step sizes of 10% and 20% and the linear pixel-wise adaptive (LPA) method with constant step sizes of 10, 15, and 20 gray level for the flat white plate and 15, 20, and 30 gray level for the checkerboard. The curves using the DPA with 10% and 20% step size coincide with one another in the case of the (b) checkerboard.

size for almost all cases of different pitch as shown in Figure 6.5(a) and a lower mean RMSE over pitch as shown in Table 6.1. With a 20% step size using the DPA method, the number of steps is comparable to having a 20 gray level step size using the LPA method (Fig. 6.6(a)), but for most values of pitch, having a 20% step size gives slightly fewer steps on average and better accuracy (Fig. 6.6(a)) as shown in Table 6.1.

For the checkerboard (Fig. 6.6(b)), the DPA method has significantly more steps than the different cases of the LPA method for small values of pitch. As the pitch increases the number of steps needed for the DPA method with either a 10% or 20% step size decreases and approaches the number of steps needed for the LPA method with a 15 gray level step size. This is because with a small pitch, there is a smaller variety of different intensities that are used to update the CDF. For large values of pitch, fewer steps are needed since more intensities can be used at each step to estimate the CDF.

Table 6.1: Mean Accuracy Computed Over Pitch and Depth for Measurements of a Flat White Plate

Method (step size)	# of steps	Bias	Std. Dev.	RMSE
DPA (10%)	12.86	-0.02	0.25	0.39
DPA (20%)	7.06	-0.01	0.25	0.38
LPA (15 gray level)	13.75	-0.04	0.25	0.39
LPA (20 gray level)	9.81	-0.04	0.25	0.39
LPA (30 gray level)	7.81	-0.02	0.25	0.39

Table 6.2: Mean Accuracy Computed Over Pitch and Depth for Measurements of a Checkerboard

Method (step size)	# of steps	Bias	Std. Dev.	RMSE
DPA (10%)	29.33	-0.52	0.56	0.79
DPA (20%)	29.33	-0.52	0.56	0.79
LPA (15 gray level)	14	-0.53	0.56	0.79
LPA (20 gray level)	10	-0.53	0.70	0.91
LPA (30 gray level)	7	-0.53	0.71	0.92

6.4 Discussion

For accurate measurement using the LPA method of saturation avoidance, the linear step size would have to be manually adjusted to measure the flat white plate and then the checkerboard. This is evident when comparing the constant 20 gray level step size using the LPA method to the 20% step size when using the DPA method for the flat white plate. For the flat white plate. both these methods perform with almost the same in terms of accuracy and number of steps, with the DPA method being only slightly better. However, when measuring the checkerboard using the LPA method with a 20 gray level step size has significant error for high values of pitch while the DPA method with a 20% step size have similar accuracy to the 15 gray level steps size using the LPA method. This shows that the LPA method would require that the size of steps be adjusted to 15 gray levels in order to achieve the same accuracy as the 20% step size when using the DPA method.

While more steps are needed for small values of pitch when measuring an object with a large range of reflectivity using the DPA method, the method of updating the CDF at each step, used by the DPA method, prevents overshooting the MIGL where there is no saturation when decrementing the MIGL to avoid saturation. This may occur when using the LPA method since the method does not adjust its step size based on the percent of pixels that have become unsaturated compared to the number of saturated pixels at the initial MIGL. This can result in significant error when performing a measurement with a large range of luminance, since the intensities could be captured at a much lower MIGL than necessary. The error due to low RMSE has an exponential trend as shown in Figure 4.17. As well, significant overshoot may cause the MIGL to be close to the same as the minimum input gray level. This would prevent the projector from projecting a fringe pattern. Instead it would project a uniform image at the minimum input gray level. Overshoot is likely the cause of the increase in error for the LPA method with gray level step sizes of 20 and 30 when measuring the checkerboard. Since the DPA method prevents overshoot, the accuracy should always be very good at different values of pitch. This is not true for the LPA method. As well, the DPA method slightly outperformed the LPA method with lower error and fewer steps when measuring object surfaces with a low range in luminance from an object surface.

The deterministic approach of using additional phase-shifts to solve for the saturated intensity in m phase-shifts is similar to Chen and Hu's method [76, 77, 78] (discussed in Section 3.2). However, instead of solving for an the unknown intensity, Chen and Hu's method solve for the phase using unsaturated intensities from the phase-shifted images. Solving for the phase directly would eliminate the need to create a composite image of unsaturated intensities. However, Chen and Hu's method

was limited to measurement using only m saturated phase-shifts making it difficult to measure objects with a large range in reflectivity, such as a checkerboard. There may also be inaccuracies associated with Chen and Hu's method when calculating the phase due to the intensity noise and nonlinearity. This also affected the estimation of the unknown saturated intensity using the deterministic approach, which is why the unknown saturated intensity estimate was corrected using the method described in Section 6.1.2. However, since the saturated intensities are used in aggregate by the DPA method, to create the CDF, these inaccuracies likely have less of an effect on measurement accuracy compared to Chen and Hu's method of calculating the phase directly, assuming zero-mean noise. While determining the unknown intensity is not necessary to solve for the phase, as in Chen and Hu's method [76, 77, 78], doing so will result in higher accuracy for the given pixel.

The accuracy of the calibrations on the white plate was significantly better than those on the black plate. This is shown when comparing the accuracies in Table 6.1 for the white plate to Table 6.2 for the checkerboard. This difference in RMSE between the white plate and checkerboard measurement is attributed to both a higher magnitude of bias or mean error, and a higher standard deviation of error. There are two known factors that contribute to this error. The first source is due to the calibration being conducted on a flat black surface for the checkerboard and a flat white surface for the white plate with added ambient light. As shown by the data modulation equation (Eq. 3.6) in Section 3.3, measurement and calibration on a surface with low luminance (black plate) has a lower SNR than measurement and calibration on a surface with high luminance (white plate), which results in higher SNR. Secondly, the contrast between the black and white squares of the checkerboard resulted in a more evident measurement error than when measuring on the white plate. This error is shown in Figure 6.7, in a 3D rendering of the measured surface of the checkerboard using the DPA method of saturation avoidance. The measurement of the checkerboard using the DPA method appears much smoother than the one shown in Figure 5.9 using the non-adaptive uniform adjustment of MIGL method at 96 MIGL (trade-off), which highlights the advantage of using the DPA method. A checkerboard rendering using the LPA method is not shown since it appears almost identical to the one rendered using the DPA method. The error attributed to the high contrast between the black and white squares is shown by vertical lines. This error only occurs between the edges on the checkerboard that are parallel to the fringe pattern. This is likely due to blending of the light between the edges of the black and white squares for the different intensities from the phase-shifted images which causes a non-sinusoidal pattern. The bias error may be attributed to inaccuracies when calculating the absolute phase using the vertical line as discussed in Section 2.5. This is because the projected vertical line on the black plate during calibration is not as distinct as it is on the white plate because the black plate has a much

lower reflectivity than the white plate. With a less distinct vertical line, the absolute phase would not be calculated as accurately, and would result in a slight bias when computing the phase difference.

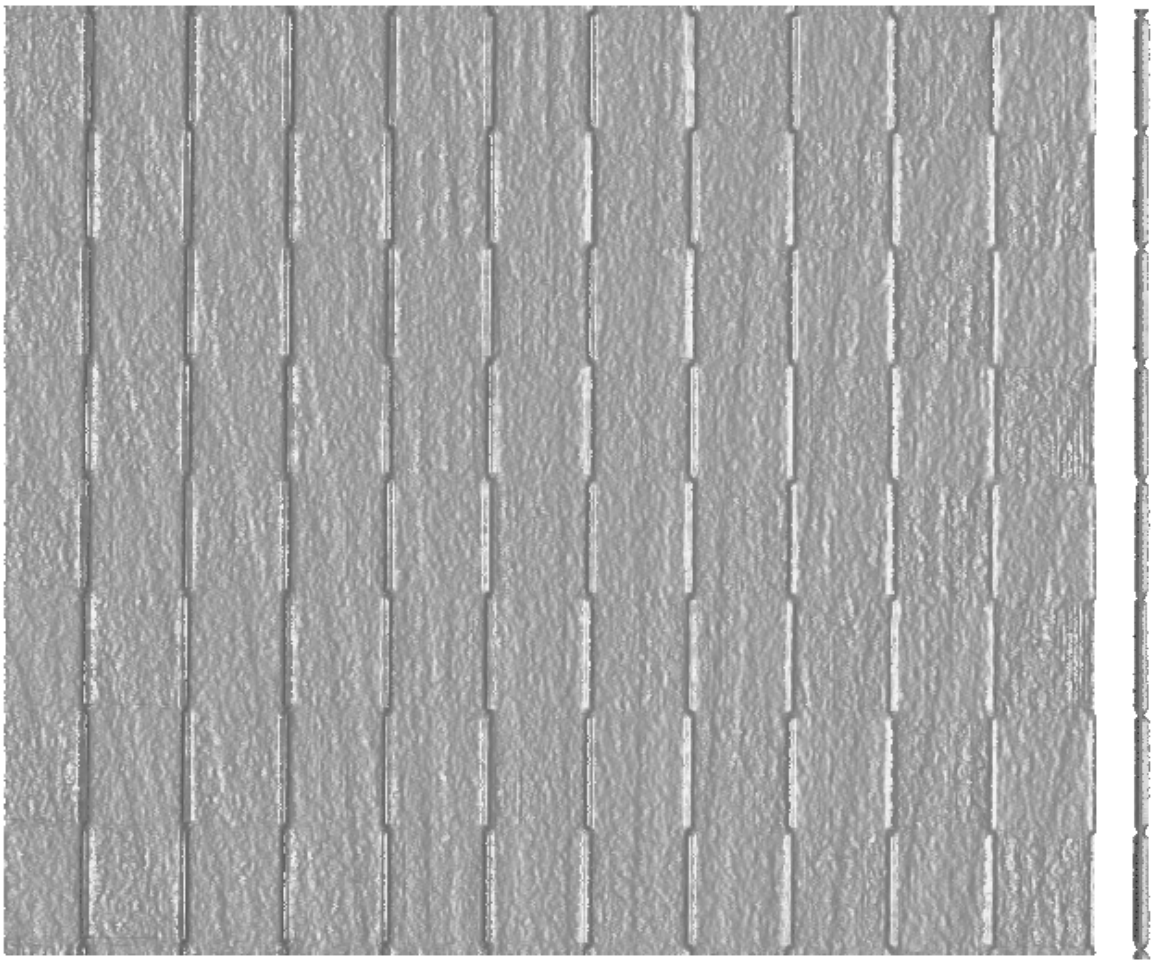

Figure 6.7: Three-dimensional surface rendering of a checkerboard using the DPA method of saturation avoidance with the sinusoidal 4-step fringe pattern and an 8 pixel pitch. To the right of the checkerboard is a profile view of the checkerboard surface. A single pass by a 3×3 pixel mean and 3×3 pixel median filter were performed on the measurement result to reduce high frequency noise.

Chapter 7

Future work

The methods of saturation avoidance presented in this thesis proved to increase accuracy when measurement would otherwise cause saturation. In the case of the LPA and DPA methods, a high SNR was also maintained. This helped when performing measurements with a large range of reflectivity and luminance from an object surface. The DPA method added greater flexibility than the LPA method by automatically adapting to the different ranges of luminance without having to manually adjust any parameters. However, some observations for improvements or alternative solutions to the system were made and are left as recommendations for future work. These improvements or alternative solutions are discussed in this chapter.

7.1 Probabilistic saturated intensity estimation

An alternative method to the deterministic method described in Section 6.1 would be to use a probabilistic approach. This approach would have a few advantages over the deterministic approach. One is that it would not require any more than the minimum number of phase-shifted images to solve for the unknown intensities, so three phase-shifts could be used when using the sinusoidal fringe pattern. Another is that it would not make any assumptions about the nature of the pattern, so no adjustments would need to be made to perform measurement using the triangular fringe pattern.

For a three-step method, the proposed probabilistic approach would use an estimate of probability distribution functions (PDF) given that phase-shifted images are saturated and the leading phase-shifted intensity ($I_p(x, y)$), with respect to the saturated phase-shifted intensity ($I_s(x, y)$), is equal to y while the lagging phase-shifted intensity ($I_n(x, y)$), with respect to the saturated intensity ($I_s(x, y)$), is equal to z ($P(x|I_s(x, y) = 2^B - 1, I_p(x, y) = y, I_n(x, y) = z)$). This should be computed for each

possible combination of y and z. A parametric approach assuming a Gaussian PDF and a nonparametric approach were both tested but the nonparametric approach was slightly more accurate. Both methods required training data of saturated fringe patterns with a large range of saturated intensities. The estimate of the unknown saturated intensity was found using the method from Equation 6.3. For the nonparametric approach, a normalized histogram was created for the intensities grouped by each combination of y and z intensities. This large number of probability distributions could then be added together according to the observed y and z intensity values of the saturated pixels from a measurement. This would give an estimate of a PDF for the unknown saturated intensities in the image and could be used to determine the CDF needed for the DPA method from Chapter 6.

This probabilistic approach was tested using the sinusoidal fringe pattern with three phase-shifts. It was found that the probabilistic approach was not very accurate when only using two phase-shifted intensities were used to estimate the one unknown saturated intensity. As a result, the estimated CDF did not resemble the ideal CDF, which was determined using Equation 6.3. While the probabolistic approach was not as successful as the deterministic approach, future work should still be conducted to see if the estimates can be corrected as in Section 6.1.2, to test different probabilistic approaches or to evaluate the limitations of the saturated intensity estimates when estimating the CDF.

7.2 Adaptive projection of phase shifted intensities

One of the advantages of using the method of adjusting the MIGL rather than the exposure time is that adjustment at the initial image acquisition stage can be performed on a pixel-by-pixel basis rather than across the entire image. Although the methods proposed in this thesis used MIGL adjustment and creation of a composite image, pixel-by-pixel, the projection of images was done only across the entire image, like the adjustment of exposure time by Zhang and Yau [79]. An improvement would be to project a composite image that would have pixels set to different MIGL which would correspond to areas of the captured image with high or low luminance. This would dramatically speed up the saturation avoidance method since it would allow for the capturing of only a single set of phase-shifted images when measuring an object with a large range of reflectivity, such as a checkerboard, once the projected composite image is known. This could facilitate an online saturation avoidance measurement system without sacrificing any loss in measurement accuracy since the projected intensities would still have a high SNR, while avoiding intensity saturation.

The problem with this method, and the reason that it is left for future work, is that it involves a complicated relationship between the projected pixels and the captured pixels. This would require stereo calibration between the camera and the projector. As well, the relationship between the camera and projector pixels would depend on the object height. It is therefore likely that an iterative method would be needed to determine the relationship between the projected intensity and object height. The camera and projector pixels would not have a one-to-one correspondence. An interpolation method would be needed for the captured pixel intensity to have the correct phase-shifted intensity. These are some of the foreseen problems that would need to be overcome to have a method that projects composite pixels of MIGL for saturation avoidance.

7.3 Synchronization of adjustment between MIGL and exposure time

One of the main limitations of adjusting the MIGL for saturation avoidance is that the camera aperture or exposure time must be manually set to be in a certain range for the camera to be able to capture the correct intensities as the projector lowers the luminance of the object by projecting at a lower MIGL. Ideally, the system would be able to automatically adjust the aperture or exposure time to select the best range for adjustment of MIGL. In this scenario, adjustment of the aperture or exposure time would serve as a rough adjustment, while the MIGL can be used for fine adjustment for saturation avoidance. To automate this, an adaptive method would have to be devised for the adjustment of the aperture or exposure time.

7.4 Improvements in DPA performance by using more advanced equipment

It is believed that better DPA performance could be achieved by using: a higher resolution and bit-level camera, and a projector with a higher contrast ratio. Having a higher bit-level camera has already been proven to give higher accuracy by Skydan et al. [80], who performed simulations at different bit-depths and found that using a 12-bit camera as opposed to an 8-bit camera can increase the measurement accuracy by a factor of four. Another reason for using a higher bit level camera would be to have a slightly higher SNR. Also, higher resolution of intensity quantization levels would permit a more accurate selection of when pixels become unsaturated. This

would also allow for the deterministic saturated intensity estimation method to have more accurate estimation of the unknown saturated intensities used to estimate the CDF. A higher bit-level camera may reduce the risk of overshoot of the MIGL with no saturation. Although there may be less risk of overshoot, the DPA method would still be useful since there is a larger range in gray level, where there may be no new unsaturated pixels if the constant step size for the LPA method is too small.

In addition to giving a higher accuracy by having a denser measurement spatially, a higher resolution camera would provide a wider variety of intensities that would be used to update the CDF for the DPA method. This may decrease the number of steps used by the DPA method when performing measurement with a large range of luminance, since more saturated intensities would be acquired at each step.

A projector with a higher contrast ratio would increase the range of projected intensities and would allow for measurement with a larger range of saturation. This would give more control of the luminance of the object when adjusting the MIGL, and in turn the projected intensity, for saturation avoidance.

Chapter 8

Conclusions

This thesis contributes three methods of saturation avoidance using the PSFPP method for full-field 3D surface measurement. The use of these saturation avoidance methods allows for measurement of objects with a change in ambient lighting or with a large range of luminance or reflectivity that causes camera sensor saturation and/or a low signal-to-noise ratio (SNR) resulting in significant measurement error.

All methods use a novel approach of captured image adjustment by lowering the maximum input gray level (MIGL) of the projected pattern. The first method, the non-adaptive uniform adjustment of MIGL method, showed that reducing the MIGL lowers the measurement error until a trade-off point, below which, the intensity modulation and SNR in the fringe patterns are too low and begin to diminish the advantage of further MIGL reduction. This point is referred to as the trade-off MIGL. The trade-off MIGL represents the point at which the highest accuracy can be achieved without having to capture phase-shifted images at different MIGL. In the case when performing measurement with a small range of luminance and saturation due to added ambient light, this non adaptive uniform adjustment of MIGL method was found to have the same accuracy as the LPA method, which requires multiple sets of phase-shifted images at different MIGL.

The LPA method had higher accuracy (lower error) than the non-adaptive uniform adjustment of MIGL method when performing measurement with a large range of luminance. This is because the LPA method maintains a high SNR when possible by creating a composite image for each phase-shift where the intensity at each pixel is captured at the highest MIGL with no saturation at any of the phase-shifted intensities. The DPA method improves upon the LPA method by dynamically selecting the step size in MIGL used to compute the composite images. This adds greater flexibility than the LPA method by being able to measure objects with either a low or high

range of luminance without having to make any manual adjustments to parameters in the method.

The DPA method avoids overshoot when decrementing the MIGL from the maximum MIGL with no saturation. Overshoot of the maximum MIGL with no saturation (lowering the MIGL more than necessary to avoid saturation) can result in significant measurement error since the input intensity modulation decreases as the MIGL is lowered.

These methods of saturation avoidance meet the main thesis goal of being able to measure surfaces with a large change or range of luminance. The measurement accuracy, when there is saturation, can often be improved to be comparable to the accuracy that would be expected if saturation had not occurred. In addition, these methods require no additional hardware, outside of what is needed for the PSFPP system. If there is no saturation, then the PSFPP measurement process continues as it normally would have without making any adjustments or having to switch to the conventional method. Last of all, no restrictions were placed on the PSFPP process except for the fact that the DPA method requires at least one more phase-shift than the minimum number of phase-shifts used for the PSFPP method. This is not a significant restriction, as it is very common to use the four-step (image) sinusoidal pattern as it yields higher accuracy than the three-step method [42].

Hopefully, this work inspires more research in the area of saturation avoidance using the adjustment of MIGL to improve the robustness of measurement. Further development in this area may allow for a wider range of measurement applications for measurement in uncontrolled environments and of specular surfaces with a large range of reflectivity or luminance.

References

[1] O. Skotheim and F. Couweleers. "Structured light projection for accurate 3D shape determination". In *Proc. 12th Int. Conf. Exp. Mech.* 2004.

[2] D. W. Capson and S. Eng. "A tiered-color illumination approach for machine inspection". *IEEE Transactions on Pattern Analysis and Machine Intelligence*, **10**(3), (1988) 387–393.

[3] J. Jeong, D. Hong, and H. Cho. "Measurement of partially specular objects by controlling imaging range". *Proceedings of SPIE*, **6718**, (2007) 671808–671808–10.

[4] F. Chen, G. M. Brown, and M. Song. "Overview of three-dimensional shape measurement using optical methods". *Optical Engineering*, **39**(1), (2000) 10.

[5] Z. Shuxian, Z. Wanhua, and L. Bingheng. "3D reconstruction of the structure of a residual limb for customising the design of a prosthetic socket". *Medical Engineering & Physics*, **27**(1), (2005) 67–74.

[6] M. Halioua and H.-C. Liu. "Optical three-dimensional sensing by phase measuring profilometry". *Optics and Lasers in Engineering*, **11**(3), (1989) 185–215.

[7] G. Sansoni and F. Docchio. "Three-dimensional optical measurements and reverse engineering for automotive applications". *Robotics and Computer Integrated Manufacturing*, **20**(5), (2004) 359–367.

[8] V. Carbone, M. Carocci, E. Savio, G. Sansoni, and L. De Chiffre. "Combination of a vision system and a coordinate measuring machine for the reverse engineering of freeform surfaces". *The International Journal of Advanced Manufacturing Technology*, **17**(4), (2001) 263–271.

[9] L. Meesters, W. IJsselsteijn, and P. Seuntiens. "A survey of perceptual evaluations and requirements of three-dimensional TV". *IEEE Transactions on Circuits and Systems for Video Technology*, **14**(3), (2004) 381–391.

[10] E. Stoykova, A. Alatan, P. Benzie, N. Grammalidis, S. Malassiotis, J. Ostermann, S. Piekh, V. Sainov, C. Theobalt, T. Thevar, and Others. "3DTV: 3D time-varying scene capture technologies: A survey". *IEEE Transactions on Circuits and Systems for Video Technology*, **17**(11), (2007) 1568–1586.

[11] A. S. Mian, M. Bennamoun, and R. Owens. "Three-dimensional model-based object recognition and segmentation in cluttered scenes." *IEEE Transactions on Pattern Analysis and Machine Intelligence*, **28**(10), (2006) 1584–1601.

[12] I. Gordon and D. Lowe. *What and where: 3D object recognition with accurate pose*, chapter 3, 67–82. 4170th edition. Springer, Berlin / Heidelberg, 2006.

[13] K. W. Bowyer, K. Chang, and P. Flynn. "A survey of approaches and challenges in 3D and multi-modal 3D+2D face recognition". *Computer Vision and Image Understanding*, **101**(1), (2006) 1–15.

[14] A. F. Abate, M. Nappi, D. Riccio, and G. Sabatino. "2D and 3D face recognition: A survey". *Pattern Recognition Letters*, **28**(14), (2007) 1885–1906.

[15] N. Glossop. "Laser projection augmented reality system for computer-assisted surgery". *International Congress Series*, **1256**, (2003) 65–71.

[16] C.-C. Wang, C. Thorpe, S. Thrun, M. Hebert, and H. Durrant-Whyte. "Simultaneous localization, mapping and moving object tracking". *The International Journal of Robotics Research*, **26**(9), (2007) 889–916.

[17] J. Alsinet, Y. Petillot, J. Salvi, and X. Lladó. "The SLAM problem: a survey". In *Artificial Intelligence Research and Development: Proceedings of the 11th International Conference of the Catalan Association for Artificial Intelligence*, 363. IOS Press, 2008.

[18] J. Salvi, E. M. Mouaddib, and J. Batlle. "An overview of the advantages and constraints of coded pattern projection techniques for autonomous navigation". In *Intelligent Robots and Systems*, 1264–1271. IEEE, Grenoble, France, 1997.

[19] B. Curless. "From range scans to 3D models". *ACM SIGGRAPH Computer Graphics*, **33**(4), (1999) 38–41.

[20] J. Kofman, J. T. Wu, and K. Borribanbunpotkat. "Multiple-line full-field laser-camera range sensor". *Proceedings of SPIE*, **6718**, (2007) 67180A–1–9.

[21] J. Batlle, E. M. Mouaddib, and J. Salvi. "Recent progress in coded structured light as a technique to solve the correspondence problem: a survey". *Pattern Recognition*, **31**(7), (1998) 963–982.

[22] U. R. Dhond and J. Aggarwal. "Structure from stereo: A review". *IEEE Transactions on Systems Man and Cybernetics*, **19**(6), (1989) 1489–1510.

[23] J. Y. Bouguet. "Camera calibration toolbox for Matlab", 2008.
URL `http://www.vision.caltech.edu/bouguetj/calib_doc/`

[24] A. S. Ogale and Y. Aloimonos. "Shape and the Stereo Correspondence Problem". *International Journal of Computer Vision*, **65**(3), (2005) 147–162.

[25] G. Bradski and A. Kaehler. *Learning OpenCV: Computer Vision with the OpenCV Library*. 1st edition. O'Reilly Media, 2008.

[26] D. Scharstein, R. Szeliski, and R. Zabih. "A taxonomy and evaluation of dense two-frame stereo correspondence algorithms". *Proceedings IEEE Workshop on Stereo and Multi-Baseline Vision (SMBV 2001)*, **47**(1), (2002) 131–140.

[27] G. Healey and T. O. Binford. "Local shape from specularity". *Computer Vision, Graphics and Image Processing*, **42**, (1988) 62–86.

[28] D. C. Knill, P. Mamassian, and D. Kersten. "Geometry of shadows". *Journal of Optical Society of America*, **14**(12), (1997) 3216–3232.

[29] B. K. Horn. "Shape from shading: A method for obtaining the shape of a smooth opaque object from one view", 1970.
URL `http://dspace.mit.edu/handle/1721.1/6885`

[30] R. Klette and R. Kozera. "Shape from shading and photometric stereo methods". *Communication and Information Technology Research Technical Report*, **20**, (1998) 57.

[31] R. Zhang, P.-S. Tsai, J. E. Cryer, and M. Shah. "Shape-from-shading: a survey". *IEEE Transactions on Pattern Analysis and Machine Intelligence*, **21**(8), (1999) 690–706.

[32] S. Shafer. *Shadows and Silhouettes in Computer Vision*. 3rd edition. Springer, 1985.

[33] J. Stauder. "Point light source estimation from two images and its limits". *International Journal of Computer Vision*, **36**(3), (2000) 195–220.

[34] W. Zhou and C. Kambhamettu. "A unified framework for scene illuminant estimation". *Image and Vision Computing*, **26**(3), (2008) 415–429.

[35] K. J. G. *Optical Metrology*. 3rd edition. J. Wiley & Sons, Chichester, 2002.

[36] R. C. Daley and L. G. Hassebrook. "Channel capacity model of binary encoded structured light-stripe illumination." *Applied Optics*, **37**(17), (1998) 3689–3696.

[37] J. Salvi, J. Pagès, and J. Batlle. "Pattern codification strategies in structured light systems". *Pattern Recognition*, **37**(4), (2004) 827–849.

[38] J. A. Quiroga, D. Crespo, J. Vargas, and J. A. Gomez-Pedrero. "Adaptive spatiotemporal structured light method for fast three-dimensional measurement". *Optical Engineering*, **45**(10), (2006) 1–8.

[39] P. S. Huang, S. Zhang, and F.-P. Chiang. "Trapezoidal phase-shifting method for three-dimensional shape measurement". *Optical Engineering*, **44**(12), (2005) 123601.

[40] P. S. Huang and S. Zhang. "Fast three-step phase-shifting algorithm". *Applied Optics*, **45**(21), (2006) 5086–5091.

[41] P. Jia, J. Kofman, and C. English. "Two-step triangular-pattern phase-shifting method for three-dimensional object-shape measurement". *Optical Engineering*, **46**(8), (2007) 083201.

[42] P. Jia, J. Kofman, and C. English. "Multiple-step triangular-pattern phase shifting and the influence of number of steps and pitch on measurement accuracy." *Applied optics*, **46**(16), (2007) 3253–62.

[43] J. Salvi, S. Fernandez, T. Pribanic, and X. Llado. "A state of the art in structured light patterns for surface profilometry". *Pattern Recognition*, **43**(8), (2010) 2666–2680.

[44] S. S. Gorthi and P. Rastogi. "Fringe projection techniques: Whither we are?" *Optics and Lasers in Engineering*, **48**, (2010) 133–140.

[45] S. Zhang. "Recent progresses on real-time 3D shape measurement using digital fringe projection techniques". *Optics and Lasers in Engineering*, **48**(2), (2010) 149–158.

[46] S. Xianyu and W. Chen. "Fourier transform profilometry: a review". *Optics and Lasers in Engineering*, **35**(5), (2001) 263–284.

[47] M. Takeda and K. Mutoh. "Fourier transform profilometry for the automatic measurement of 3-D object shapes". *Applied Optics*, **22**(24), (1983) 3977–3982.

[48] Q. Hu and K. G. Harding. "Conversion from phase map to coordinate: Comparison among spatial carrier, Fourier transform, and phase shifting methods". *Optics and Lasers in Engineering*, **45**(2), (2007) 342–348.

[49] X. Su and Q. Zhang. "Dynamic 3-D shape measurement method: A review". *Optics and Lasers in Engineering*, **48**(2), (2010) 191–204.

[50] P. Jia, J. Kofman, and C. English. "Real-time full-field 3-D surface-shape measurement using off-the-shelf components and a single processor". In *International Conference on 3-D Digital Imaging and Modeling*, 3DIM, 19–23. IEEE Computer Society, 2007.

[51] S. Zhang and P. S. Huang. "High-resolution, real-time three-dimensional shape measurement". *Optical Engineering*, **45**(12), (2006) 1–8.

[52] J. Li, L. G. Hassebrook, and C. Guan. "Optimized two-frequency phase-measuring-profilometry light-sensor temporal-noise sensitivity." *Journal of the Optical Society of America. A, Optics, image science, and vision*, **20**(1), (2003) 106–15.

[53] B. Kamgar-parsi and B. Kamgar-parsi. "Evaluation of quantization error in computer vision". *IEEE Transactions on Pattern Analysis and Machine Intelligence*, **11**(9), (1989) 929–940.

[54] C. Waddington and J. Kofman. "Analysis of measurement sensitivity to illuminance and fringe-pattern gray levels for fringe-pattern projection adaptive to ambient lighting". *Optics and Lasers in Engineering*, **48**(2), (2010) 251–256.

[55] D. Nobis and C. M. Vest. "Statistical analysis of errors in holographic interferometry". *Applied Optics*, **17**(14), (1978) 2198–2204.

[56] T. R. Judge and P. J. Bryanston-Cross. "A review of phase unwrapping techniques in fringe analysis". *Optics and Lasers in Engineering*, **21**(4), (1994) 199–239.

[57] E. Zappa and G. Busca. "Comparison of eight unwrapping algorithms applied to Fourier-transform profilometry". *Optics and Lasers in Engineering*, **46**(2), (2008) 106–116.

[58] P. Jia. *Real-time full-field range-sensing for 3-D surface-shape measurement*. Phd in mechanical engineering, University of Ottawa, 2006.

[59] P. Jia, J. Kofman, and C. English. "Comparison of linear and nonlinear calibration methods for phase-measuring profilometry". *Optical Engineering*, **46**(4), (2007) 1–10.

[60] S. Zhang and P. S. Huang. "Novel method for structured light system calibration". *Optical Engineering*, **45**(8), (2006) 1–8.

[61] H. Guo, Y. Yu, H. He, and M. Chen. "Least-squares calibration method for fringe projection profilometry". *Optical Engineering*, **44**(3), (2005) 1–9.

[62] H. Guo, H. He, and M. Chen. "Gamma correction for digital fringe projection profilometry". *Applied Optics*, **43**(14), (2004) 2906–2914.

[63] L. Chen and C. Liao. "Calibration of 3D surface profilometry using digital fringe projection". *Measurement Science & Technology*, **16**(8), (2005) 1554–1566.

[64] E. Zappa and G. Busca. "Fourier-transform profilometry calibration based on an exhaustive geometric model of the system". *Optics and Lasers in Engineering*, **47**(7-8), (2009) 754–767.

[65] G. Sansoni, M. Carocci, and R. Rodella. "Calibration and performance evaluation of a 3-D imaging sensor based on the projection of structured light". *IEEE Transactions on Instrumentation and Measurement*, **49**(3), (2000) 628–636.

[66] Z. Li, Y. Shi, C. Wang, and Y. Wang. "Accurate calibration method for a structured light system". *Optical Engineering*, **47**(5), (2008) 053604.

[67] J. Vargas, J. Antonio Quiroga, and M. Jose Terron-Lopez. "Flexible calibration procedure for fringe projection profilometry". *Optical Engineering*, **46**(2), (2007) 023601.

[68] Z. Wang, D. A. Nguyen, and J. C. Barnes. "Some practical considerations in fringe projection profilometry". *Optics and Lasers in Engineering*, **48**(2), (2010) 218–225.

[69] J. Tao, X. Juntong, and Y. Junqi. "An accurate three-dimensional scanning system with a new phase error compensation method". *The International Journal of Advanced Manufacturing Technology*, **29**(11-12), (2005) 1178–1185.

[70] X. Chen, J. Xi, and Y. Jin. "Phase error compensation method using smoothing spline approximation for a three-dimensional shape measurement system based on gray-code and phase-shift light projection". *Optical Engineering*, **47**(11), (2008) 113601.

[71] B. Pan, Q. Kemao, L. Huang, and A. Asundi. "Phase error analysis and compensation for nonsinusoidal waveforms in phase-shifting digital fringe projection profilometry". *Optics Letters*, **34**(4), (2009) 416.

[72] S. Zhang and S.-T. Yau. "Generic nonsinusoidal phase error correction for three-dimensional shape measurement using a digital video projector." *Applied Optics*, **46**(1), (2007) 36–43.

[73] P. Jia, J. Kofman, and C. English. "Intensity-ratio error compensation for triangular-pattern phase-shifting profilometry." *Journal of the Optical Society of America. A, Optics, image science, and vision*, **24**(10), (2007) 3150–8.

[74] R. Kowarschik, P. Kuhmstedt, J. Gerber, W. Schreiber, and G. Notni. "Adaptive optical three-dimensional measurement with structured light". *Optical Engineering*, **39**(1), (2000) 150.

[75] Q. Hu, K. G. Harding, X. Du, and D. Hamilton. "Shiny parts measurement using color separation". In K. G. Harding (editor), *Two- and Three-Dimensional Methods for Inspection and Metrology III*, volume 6000, 60000D–8. SPIE, Boston, MA, USA, November 2005.

[76] E. Hu, Y. He, and Y. Chen. "Study on a novel phase-recovering algorithm for partial intensity saturation in digital projection grating phase-shifting profilometry". *Optik - International Journal for Light and Electron Optics*, **121**(1), (2008) 23–28.

[77] Y. Chen, Y. He, and E. Hu. "Phase deviation analysis and phase retrieval for partial intensity saturation in phase-shifting projected fringe profilometry q". *Optics Communications*, **281**, (2008) 3087–3090.

[78] E. Hu, Y. He, and W. Wu. "Further study of the phase-recovering algorithm for saturated fringe patterns with a larger saturation coefficient in the projection grating phase-shifting profilometry". *Optik - International Journal for Light and Electron Optics*, **121**(14), (2010) 1290–1294.

[79] S. Zhang and S.-T. Yau. "High dynamic range scanning technique". *Optical Engineering*, **48**(3), (2009) 1–7.

[80] O. A. Skydan, F. Lilley, M. J. Lalor, and D. R. Burton. "Quantization error of CCD cameras and their influence on phase calculation in fringe pattern analysis". *Applied Optics*, **42**(26), (2003) 5302–5307.